In-situ Transmission Electron Microscopy Studies on Graphene

Proefschrift

ter verkrijging van de graad van doctor
aan de Technische Universiteit Delft,
op gezag van de Rector Magnificus prof.ir. K.C.A.M. Luyben;
voorzitter van het College voor Promoties,
in het openbaar te verdedigen op
vrijdag 17 Februari 2017 om 12:30 uur

door

Leonardo VICARELLI

Master of Science in Physics, Università di Pisa, Italië

Geboren te Siena, Italië

This dissertation has been approved by the promotor:

Prof.dr. H.W. Zandbergen

Composition of the doctoral committee:

Rector Magnificus	chairman
Prof.dr. H.W. Zandbergen	Technische Universiteit Delft, promotor

Independent members:

Prof.dr. R. E. Dunin-Borkowski	Forschungszentrum Jülich, Germany
Prof.dr. A. Tredicucci	Università di Pisa, Italy
Prof.dr. C. Dekker	Technische Universiteit Delft
Prof.dr.ir. L.M.K Vandersypen	Technische Universiteit Delft
Prof.dr. G.C.A.M. Janssen	Technische Universiteit Delft
Dr.ir. F.D. Tichelaar	Technische Universiteit Delft

This research was financially supported by ERC project 267922, "NemInTEM"

Keywords: In-situ, transmission electron microscopy, graphene, nanoribbons, direct sculpting, self-healing, MEMS heater, electron holography

Printed by: Gildeprint

Cover design: Projected phase shift of electrostatically charged graphene nanotips, measured with electron holography. By Leonardo Vicarelli & Linda Paoli

Author email: leonardo.vicarelli@gmail.com

ISBN: 978-90-8593-286-4
Casimir PhD series, Delft-Leiden 2017-1

An electronic version of this dissertation is available at:
`http://repository.tudelft.nl`

CONTENTS

CHAPTER 1

Introduction

Welcome reader! This introductory chapter will show you around the topic of this thesis. Why are we doing it? Why should we choose electron microscopy to study materials? These and many other questions will be raised, and hopefully answered.

We start with a brief history of in-situ electron microscopy, to see the evolution of this technique in the last 50 years. Then we explain what is graphene, with emphasis on nanoribbons, and why it is important to study it.

1.1 In-situ electron microscopy: a brief review

What is “in-situ” microscopy? To keep it short, it is the possibility to apply an external stimulus (electrical bias, gas flow, liquid flow, magnetic field, etc.) while observing the changes happening on the sample under investigation. Everything happens in real-time, live, simultaneously. These are some of the key words that distinguish in-situ microscopy from the traditional way of doing experiments, which we will call “ex-situ”.

The Transmission Electron Microscope (TEM) is a very powerful tool, which allows to image materials at a very small scale, from 100 µm (micrometer, 10^{-6} meters) down to 50 pm (picometer, 10^{-12} meters). Combining “in-situ” with “TEM”, we can monitor the changes of a material, in real-time, at atomic level.

The first examples of in-situ TEM date back to the early 1950’s and 60’s [1]–[3], in which they were using in-situ heating to study the nucleation, deposition and annealing of thin metal films. In the following years, the number of applications and in-situ techniques grew steadily[4]: cooling stages, working at temperatures below 10 K; strain stages to deform samples; environmental cells for gas and liquid experiments.

In-situ electrical measurements in TEM were also developed in the 1960’s. The work of Blech and Meieran [5], [6] used electrical contacts to apply a current across a thin aluminum film and visualize electromigration. Many other applications were developed in the following 50 years, including electrical characterization of nanowires and carbon nanotubes, holography on biased p-n junctions, lithiation of nanowires, electric field-emission from microtips and nanotubes [7]. More recently, the same in-situ electrical measurements have been applied to study graphene and other layered materials, of which we give a brief introduction in the next sections.

1.2 Graphene (and graphene nanoribbons)

Graphene is an allotrope of carbon, namely one of the possible crystalline shapes that carbon can have. It consists of a one atom thick carbon film, where the atoms are arranged in a honeycomb structure, shown in Figure 1.1(a). It was discovered in 2004 by Geim and Novoselov [8], who were playing with scotch tape and graphite. They found out that it is possible to peel off a single graphitic plane with the tape and place it on a silicon substrate, which was thought to be theoretically impossible because of the instability of a one-atom thick film. The discovery granted them the Nobel Prize in 2010, and opened the road for a new branch in material physics, which is the study of two-dimensional (2D) materials.

When arranged in such a honeycomb structure, carbon has sp_2 hybridization, which leaves a cloud of π orbital electrons available for electrical conduction. This feature gives graphene many of the properties of 2D electron gases (2DEG), already studied in MOSFET’s for over 30 years[11], such as the integer and fractional Quantum Hall effect, plasmons oscillation, and the Kosterlitz–Thouless phase transition (who were just awarded with the 2016 Nobel Prize in Physics for their discovery, together with Duncan Haldane). However, graphene possesses a very peculiar band structure, which the other 2DEG do not have.

With a simple tight-binding calculation [12], we see that there are two special points in the Brillouin Zone (BZ), called K and K', where the energy dispersion is linear with the momentum, with zero gap between the conduction and valence bands. This kind of linear energy dispersion is also shared by ultrarelavistic particles, such as neutrinos, which obey the massless Dirac equation. Therefore, we can make an analogy with graphene and say that the charge carriers are not just electrons or holes, but massless, fermionic quasiparticles, which travel at the Fermi velocity of $v_F = 10^6$ m/s (300 times slower than light). Interesting phenomena related to this Dirac-like nature are the chiral tunneling and Klein paradox and the anomalous integer quantum Hall effect [12].

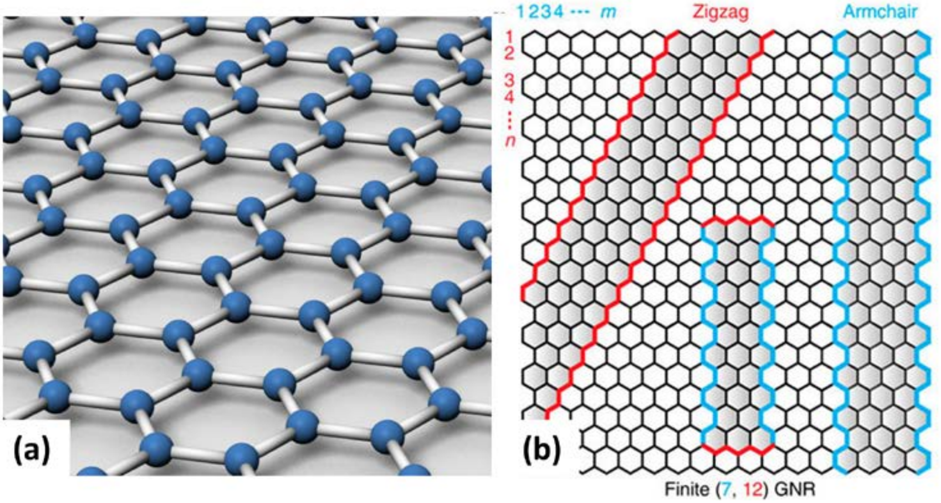

Figure 1.1 (a) bird-view of graphene lattice, with the hexagonal, honeycomb structure. From [9] under CC BY-NC-SA 3.0 license. (b) Illustration of the possible edge configuration of a graphene nanoribbon. Adapted from [10] under CC BY 4.0 license.

The fact that graphene has no bandgap poses somehow a problem for electronics applications. For example, if we want to fabricate a Field Effect Transistor (FET) with graphene, it is impossible to turn off the electronic current flowing in the channel, which is a fundamental requirement of a logic gate. Therefore, it would be nice to add a bandgap in graphene, while preserving all the other nice properties, such as electron mobility, thermal conductivity and mechanical strength. One possible solution is offered by graphene nanoribbons: if we cut graphene along one of the main crystallographic axis, we obtain stripes of graphene which have either armchair or zig-zag edges (see

Figure 1.1(b)). Ab-initio calculations have shown that both armchair and zigzag edges give a bandgap which scales as the inverse of the ribbon width [13], although they have different mechanisms at the base of this opening. However, the presence of defects on the edges can disrupt electronic transport, and, in the worst case, induce charge localization and insulating states.

Many experiments have tried to fabricate graphene nanoribbons, following various routes. These approaches can be mainly distinguished between bottom-up and top-down. In the first case, GNRs are chemically synthetized from basic organic molecules: this technique can produce atomically sharp edges and relatively long ribbons, but the main problem remains the interface with a metallic contact, which gives a big contact resistance. In the top-down approach, the nanoribbon is produced from a large graphene flake, removing the undesired parts. There are many possible ways to selectively remove graphene: oxygen and hydrogen plasma etching [14], [15], AFM direct lithography[16], STM lithography[17] and catalytic etching [18].

There is one additional top-down method for graphene patterning, which is direct sculpting via electron or ion beam. Since this topic is particularly relevant for us, we’re going to explain it in more depth in the following section.

1.3 Direct sculpting of graphene with electron and ion beams

The first experiment to sculpt, or ablate, graphene with electron beams was performed by Fischbein and Drndić in 2008 [19]. Graphene was suspended on a grid and the focused electron beam of a TEM was used to sputter carbon atoms away from the lattice. The basic requirement is just to use electrons whose energy is higher than the threshold for knock-off damage in carbon materials, namely 86 keV [20].

In the following years, the technique of electron beam sculpting has been adopted by various groups [21]–[23], also in combination with in-situ electrical measurements [24]–[28]. The advantages of e-beam sculpting over other lithographic methods are: the sample cleanliness, because graphene does not come in contact with any physical mask; atomic-resolution imaging and sub-nm sculpting precision; the possibility to run in-situ measurements during the device fabrication, to check the evolution of electrical properties. E-beam sculpting also has some disadvantages/challenges: the first is the fabrication of suspended devices, which are very fragile; this would make e-beam sculpting quite unpractical for mass-production of devices. The second challenge is the beam-induced carbon deposition[29], which causes carbon to be deposited, instead of being etched by the e-beam. Heating or cooling the sample can solve this problem, as it changes the diffusivity of carbon on graphene surface.

Another solution for graphene sculpting comes from ion beam milling. In this category we distinguish between Gallium [30], Helium [31]–[35] and more recently also Neon ions [36]. The advantages of these methods over e-beam are the possibility to pattern graphene on a substrate, and much faster etching rate. The adverse sides are the limited cutting precision, mostly because of backscattering from the substrate, and the amorphization of graphene edges near the sculpted area. A recent experiment [37] showed that the cutting precision can be improved in suspended graphene, but it remains ultimately limited by the spot size of the beam, which is around 2-3 nm for Gallium and Helium ion sources.

1.4 Scope of present research: in-situ electrical measurements and graphene sculpting in TEM.

From the previous sections, we have seen that in-situ microscopy is a powerful tool to investigate materials at the nanoscale. We also have discovered graphene nanoribbons, and found a way to fabricate them inside a TEM. Why not combining the two ideas? And this is what this thesis is mainly about.

First we perfected the graphene sculpting in Scanning TEM mode, introducing high-temperature annealing for edge recrystallization and lattice self-healing. Then we build integrated MEMS devices, with integrated heaters and electrical contacts, to perform in-situ electrical measurements. Finally we combined these two elements to measure, in-situ, e-beam sculpted graphene nanoribbons.

As we already mentioned, other works have walked on the same route [24]–[28], achieving remarkable results. Our work distinguishes itself for four key elements:

1. The graphene sculpting is performed with Scanning TEM mode, which gives unprecedented sub-nm precision during the cutting.
2. Graphene sculpting is performed at high temperature, using an independently controlled microheater. This feature also allows performing temperature dependent measurements.
3. Many graphene nanoribbons, with different number of layers, were investigated, giving a good statistics on their electrical properties.
4. In-situ electrical measurements were combined with holography to study charge distribution in graphene, done for the first time in this work.

1.5 Organization of the thesis

Chapter 1 contains a general introduction on graphene, graphene nanoribbons and in-situ microscopy, including the motivation for this work. Chapter 2 introduces the TEM, its physical structure and operational modes, and how it can be used to characterize 2D materials. Chapter 3 is a short review on four recent in-situ TEM studies on graphene, useful to get a panorama of the research status. Chapters 4 and 5 contain the main results of this thesis. In Chapter 4, we present the results of in-situ electrical measurements on graphene nanoribbons. Chapter 5 talks about the in-situ holography of charge accumulation in graphene nanotips. Finally Chapter 6 is a big appendix, which contains all the device fabrication details, and much, much more.

References

[1] T. A. McLauchlan, R. S. Sennett, and G. D. Scott, “Continuous observations with the electron microscope on the formation of evaporated films of silver, gold, and tin,” *Can. J. Res.*, vol. 28a, no. 5, pp. 530–534, Sep. 1950.

[2] H. Poppa, “Progress in the Continuous Observation of Thin-Film Nucleation and Growth Processes by Electron Microscopy,” *J. Vac. Sci. Technol.*, vol. 2, no. 1, p. 42, Jan. 1965.

[3] H. Poppa, “Heterogeneous Nucleation of Bi and Ag on Amorphous Substrates (In Situ Electron Microscopy Studies),” *J. Appl. Phys.*, vol. 38, no. 10, p. 3883, 1967.

[4] E. P. Butler, “In situ experiments in the transmission electron microscope,” *Reports Prog. Phys.*, vol. 42, no. 5, pp. 833–895, 1979.

[5] I. A. Blech and E. S. Meieran, “Electromigration in thin Al films,” *J. Appl. Phys.*, vol. 40, no. 2, pp. 485–491, 1969.

[6] I. A. Blech and E. S. Meieran, “Direct transmission electron microscope observation of electrotransport in aluminum thin films,” *Appl. Phys. Lett.*, vol. 11, no. 8, pp. 263–266, 1967.

[7] S. Canepa, S. B. Alam, D.-T. Ngo, F. M. Ross, and K. Mølhave, “In Situ TEM Electrical Measurements,” in *Controlled Atmosphere Transmission Electron Microscopy*, 2016, pp. 281–300.

[8] K. S. S. Novoselov, A. K. K. Geim, S. V. V Morozov, D. Jiang, Y. Zhang, S. V. V Dubonos, I. V. V Grigorieva, and A. A. Firsov, “Electric field effect in atomically thin carbon films.,” *Science (80-.).*, vol. 306, no. 5696, pp. 666–669, Oct. 2004.

[9] “graphene-atomic-structure-sheet.png (900×600).” [Online]. Available: http://www.jameshedberg.com/img/samples/graphene-atomic-structure-sheet.png.

[10] S. Wang, L. Talirz, C. A. Pignedoli, X. Feng, K. Müllen, R. Fasel, and P. Ruffieux, “Giant edge state splitting at atomically precise graphene zigzag

edges,” *Nat. Commun.*, vol. 7, p. 11507, May 2016.

[11] T. Ando, A. B. Fowler, and F. Stern, “Electronic properties of two-dimensional systems,” *Rev. Mod. Phys.*, vol. 54, no. 2, pp. 437–672, 1982.

[12] A. H. . Castro Neto, N. M. R. . Peres, K. S. . Novoselov, A. K. . Geim, and F. Guinea, “The electronic properties of graphene,” *Rev. Mod. Phys.*, vol. 81, no. 1, pp. 109–162, Jan. 2009.

[13] Y.-W. Son, M. L. Cohen, and S. G. Louie, “Energy Gaps in Graphene Nanoribbons,” *Phys. Rev. Lett.*, vol. 97, no. 21, p. 216803, Nov. 2006.

[14] M. Y. Han, B. Özyilmaz, Y. Zhang, and P. Kim, “Energy band-gap engineering of graphene nanoribbons,” *Phys. Rev. Lett.*, vol. 98, no. 20, pp. 1–4, 2007.

[15] L. Xie, L. Jiao, and H. Dai, “Selective Etching of Graphene Edges by Hydrogen Plasma,” *J. AM. CHEM. SOC*, vol. 132, pp. 14751–14753, 2010.

[16] S. Masubuchi, M. Ono, K. Yoshida, K. Hirakawa, and T. MacHida, “Fabrication of graphene nanoribbon by local anodic oxidation lithography using atomic force microscope,” *Appl. Phys. Lett.*, vol. 94, no. 8, 2009.

[17] L. Tapasztó, G. Dobrik, P. Lambin, and L. P. Biró, “Tailoring the atomic structure of graphene nanoribbons by scanning tunnelling microscope lithography,” *Nat. Nanotechnol.*, vol. 3, no. 7, pp. 397–401, Jul. 2008.

[18] L. C. Campos, V. R. Manfrinato, J. D. Sanchez-Yamagishi, J. Kong, and P. Jarillo-Herrero, “Anisotropic Etching and Nanoribbon Formation in Single-Layer Graphene,” *Nano Lett.*, vol. 9, no. 7, pp. 2600–2604, Jul. 2009.

[19] M. D. Fischbein and M. Drndić, “Electron beam nanosculpting of suspended graphene sheets,” *Appl. Phys. Lett.*, vol. 93, no. 11, p. 113107, 2008.

[20] B. W. Smith and D. E. Luzzi, “Electron irradiation effects in single wall carbon nanotubes,” *J. Appl. Phys.*, vol. 90, no. 7, p. 3509, 2001.

[21] B. Song, G. F. Schneider, Q. Xu, G. Pandraud, C. Dekker, and H. Zandbergen, “Atomic-scale electron-beam sculpting of near-defect-free graphene nanostructures,” *Nano Lett.*, vol. 11, no. 6, pp. 2247–2250, 2011.

[22] F. Börrnert, L. Fu, S. Gorantla, M. Knupfer, B. Büchner, and M. H. Rümmeli, “Programmable sub-nanometer sculpting of graphene with electron beams.,” *ACS Nano*, vol. 6, no. 11, pp. 10327–34, Nov. 2012.

[23] Q. Xu, M. Y. Wu, G. F. Schneider, L. Houben, S. K. Malladi, C. Dekker, E. Yucelen, R. E. Dunin-Borkowski, and H. W. Zandbergen, “Controllable atomic scale patterning of freestanding monolayer graphene at elevated temperature,” *ACS Nano*, vol. 7, no. 2, pp. 1566–1572, Feb. 2013.

[24] R. Botello-me, S. J. Hong, E. a. Stach, Y. W. Park, J. C. Charlier, M. Drndic, a. T. C. Johnson, Z. J. Qi, J. a. Rodríguez-Manzo, A. R. Botello-Méndez, S. J. Hong, E. a. Stach, Y. W. Park, J. C. Charlier, M. Drndić, and a. T. C. Johnson, “Correlating Atomic Structure and Transport in Suspended Graphene Nanoribbons,” *Nano Lett.*, vol. 14, no. 8, pp. 4238–4244, 2014.

[25] Z. J. Qi, C. Daniels, S. J. Hong, Y. W. Park, V. Meunier, M. Drndic, and A. T. C. Johnson, “Electronic transport of recrystallized freestanding graphene nanoribbons,” *ACS Nano*, vol. 9, no. 4, pp. 3510–3520, Apr. 2015.

[26] J. A. Rodríguez-Manzo, Z. J. Qi, A. Crook, J.-H. Ahn, A. T. C. Johnson, and M. Drndić, “In Situ Transmission Electron Microscopy Modulation of Transport in Graphene Nanoribbons,” *ACS Nano*, vol. 10, no. 4, pp. 4004–4010, Apr. 2016.

[27] Q. Wang, R. Kitaura, S. Suzuki, Y. Miyauchi, K. Matsuda, Y. Yamamoto, S. Arai, and H. Shinohara, “Fabrication and In Situ Transmission Electron Microscope Characterization of Free-Standing Graphene Nanoribbon Devices,” *ACS Nano*, vol. 10, no. 1, pp. 1475–1480, Jan. 2016.

[28] Y. Lu, C. A. Merchant, M. Drndić, and A. T. C. Johnson, “In situ electronic characterization of graphene nanoconstrictions fabricated in a transmission electron microscope,” *Nano Lett.*, vol. 11, no. 12, pp. 5184–5188, 2011.

[29] J. C. Meyer, C. O. Girit, M. F. Crommie, and A. Zettl, “Hydrocarbon lithography on graphene membranes,” *Appl. Phys. Lett.*, vol. 92, no. 12, p. 123110, 2008.

[30] Z. Liao, T. Zhang, M. Gall, A. Dianat, R. Rosenkranz, R. Jordan, G. Cuniberti, and E. Zschech, “Lateral damage in graphene carved by high energy focused gallium ion beams,” *Appl. Phys. Lett.*, vol. 107, no. 1, p. 13108, Jul. 2015.

[31] D. C. Bell, M. C. Lemme, L. a Stern, J. R. Williams, and C. M. Marcus, “Precision cutting and patterning of graphene with helium ions,” *Nanotechnology*, vol. 20, no. 45, p. 455301, Nov. 2009.

[32] M. C. Lemme, D. C. Bell, J. R. Williams, L. A. Stern, B. W. H. Baugher, P. Jarillo-Herrero, and C. M. Marcus, “Etching of Graphene Devices with a Helium Ion Beam,” *ACS Nano*, vol. 3, no. 9, pp. 2674–2676, Sep. 2009.

[33] D. Fox, Y. B. Zhou, A. O'Neill, S. Kumar, J. J. Wang, J. N. Coleman, G. S. Duesberg, J. F. Donegan, and H. Z. Zhang, "Helium ion microscopy of graphene: beam damage, image quality and edge contrast.," *Nanotechnology*, vol. 24, no. 33, p. 335702, 2013.

[34] A. N. Abbas, G. Liu, B. Liu, L. Zhang, H. Liu, D. Ohlberg, W. Wu, and C. Zhou, "Patterning, characterization, and chemical sensing applications of graphene nanoribbon arrays down to 5 nm using helium ion beam lithography," *ACS Nano*, vol. 8, no. 2, pp. 1538–1546, 2014.

[35] G. Nanda, S. Goswami, K. Watanabe, T. Taniguchi, and P. F. A. Alkemade, "Defect Control and n -Doping of Encapsulated Graphene by Helium-Ion-Beam Irradiation," *Nano Lett.*, vol. 15, no. 6, pp. 4006–4012, Jun. 2015.

[36] V. Iberi, A. V Ievlev, I. Vlassiouk, S. Jesse, S. V Kalinin, D. C. Joy, A. J. Rondinone, A. Belianinov, and O. S. Ovchinnikova, "Graphene engineering by neon ion beams," *Nanotechnology*, vol. 27, no. 12, p. 125302, 2016.

[37] J. Buchheim, R. M. Wyss, I. Shorubalko, and H. G. Park, "Understanding the interaction between energetic ions and freestanding graphene towards practical 2D perforation," *Nanoscale*, vol. 8, no. 15, pp. 8345–8354, 2016.

CHAPTER 2

TEM basics and characterization techniques of 2D materials

This chapter gives a basic overview over the Transmission Electron Microscope (TEM) design and operation. Special attention is dedicated to the Scanning TEM (STEM) operational mode, as it has been frequently adopted during this Phd project. We explain the working principles of the three main TEM characterization techniques that we used, i.e. Energy Dispersive X-ray analysis (EDX), Electron Energy Loss Spectroscopy (EELS) and Electron Diffraction (ED). Most of this information is gathered from the textbook Transmission Electron Microscopy, by David B. Williams and C. Barry Carter [1]. Every person who aspires to become a good TEM microscopist should start from this book. Springer now offers the possibility to download it in digital form, through the journal subscription. The interested reader can find it through the website link: http://www.springer.com/us/book/9780387765006

Additionally, we give examples of how TEM and the other analytical techniques can be useful for the characterization of two-dimensional materials, in particular graphene and black phosphorus. The part concerning black phosphorus is largely based on the publication [2].

2.1 Brief historical overview

After the wave-like nature of the electron was theorized by De Broglie in 1925 (and experimentally confirmed by Davisson & Germer and Thomson & Reid in 1927), it immediately appeared clear that a microscope based on an electron beam, instead of a visible-light beam, could, in principle, be realized. The advantage of using electrons instead of photons in microscopy is evident if we compare their wavelength. According to the Rayleigh criterion, the smallest distance, δ, that can be resolved depends on the radiation wavelength λ, following the equation:

$$\delta = \frac{0.61\lambda}{\mu \sin\beta} \tag{2.1}$$

where $\mu\sin\beta$ corresponds to the numerical aperture of the lens (typically close to 1). Visible light ranges from 390 to 700 nm, which means that the smallest resolvable distance is approximately 200 nm. Electrons, on the other hand, have a much smaller wavelength, related to their energy, *E*, by De Broglie's equation (non-relativistic):

$$\lambda = \frac{1.22}{E^{1/2}}. \tag{2.2}$$

For example, a 300 keV electron has λ=2.23 pm (which is actually λ=1.97 pm adding relativistic correction), which would theoretically deliver sub-atomic resolution. As we will see later, the resolution is practically limited by several other factors, including spherical and chromatic aberration of lenses, stability of the lenses over time, spatial and temporal coherence of the electrons, etc.

The first TEM was built in 1932 by E. Ruska and M. Knoll and it had a resolution of 200 nm, similar to an optical microscope. Apart from the improved resolution, the electron microscope differs from the optical one for two important facts. First of all, an electron microscope can only operate in high-vacuum condition, which is below a pressure of 10^{-6} mbar. This ensures that the mean free path of an electron, which is the average distance travelled before colliding with a gas molecule, is greater than 50 m, long enough to run from the electron gun to the image detector unscattered. The second issue to be addressed is how to make a lens for electrons: this can be done using a magnetic field, generated by an electromagnetic coil. The Lorentz force exerted by the field on the electron will bend its trajectory in a circular path, whose radius can be adjusted by tuning the intensity of the field itself.

Modern TEMs, equipped with spherical aberration correctors and cold field-emission electron sources, can reach 50 pm resolution [3], which is very close the quantum limit set by width of the electron wave function in the atoms. With atomic imaging being routinely performed in TEM, research is currently pushing the evolution of such a wonderful machine beyond other limits, rather than resolution. Improvement of electron detectors, chromatic aberration correctors, low-voltage microscopy, in-situ microscopy, cryo-microscopy, holo-microscopy, elemental analysis detectors, etc. will make the TEM a more versatile machine, being able to investigate radiation sensitive materials, automatically find chemical composition, combine imaging with external stimuli, map electric and magnetic fields. All with atomic scale resolution.

2.2 TEM basics: the journey of the electron through the microscope

This section is devoted to the TEM basics: how does it work, what are its components and a brief consideration about resolution limits. In order to explain it, we follow the path of electrons through the microscope, using the TEM cross-section in Figure 2.1 to help us visualizing the journey: starting from the electron gun, electrons are accelerated at high energies, they are focused on the sample by electromagnetic lenses, they interact with the specimen, they go through more lenses that magnify the image and, finally, they reach the image detector. Additional detectors can also be added along the way for elemental analysis (which will be discussed in Chapter 2.4).

The topic would be extremely vast, as the real design of a microscope is quite complex. Therefore we focus only on the main components, which we think are more essential to understand the results of this thesis. We proceed in order, starting from the electron source on top and finishing with the image detector at the bottom. A separate section is dedicated to STEM mode.

2.2.1 The electron source

The electron source is where the electrons are generated, or, to be more precise, extracted from a material. There are mainly two types of electron sources: thermionic and field-emission. The first type exploits the thermionic effect to extract electrons from a material with high melting point, such as a tungsten filament, or from a material with low work function, such as a LaB_6 crystal. The second type instead uses electron tunneling to extract electrons: a high voltage (a few kV) is used to extract electrons from a sharp tungsten tip (less than 100 nm tip radius). Field-emission sources have several advantages over thermionic sources: they have higher brightness, better temporal and spatial coherence and smaller probe size (useful for STEM imaging). Some techniques, such as electron holography (see Chapter 5) and high-resolution EELS, would actually be impossible to perform using a thermionic source. Therefore, a cold field-emission source is preferable in most cases, although it comes at a higher financial cost. After the electrons have been extracted, they are accelerated at the desired energy with a strong electric field. A wide range of energies is possible, depending on the purpose of the microscope [4]: low-voltage TEMs for biological samples operate in the 30-100 keV range to reduce beam damage; most TEMs for material analysis operate at higher energies, between 80 and 300 keV; some special (and very expensive) microscopes reach the 1-3 MeV scale.

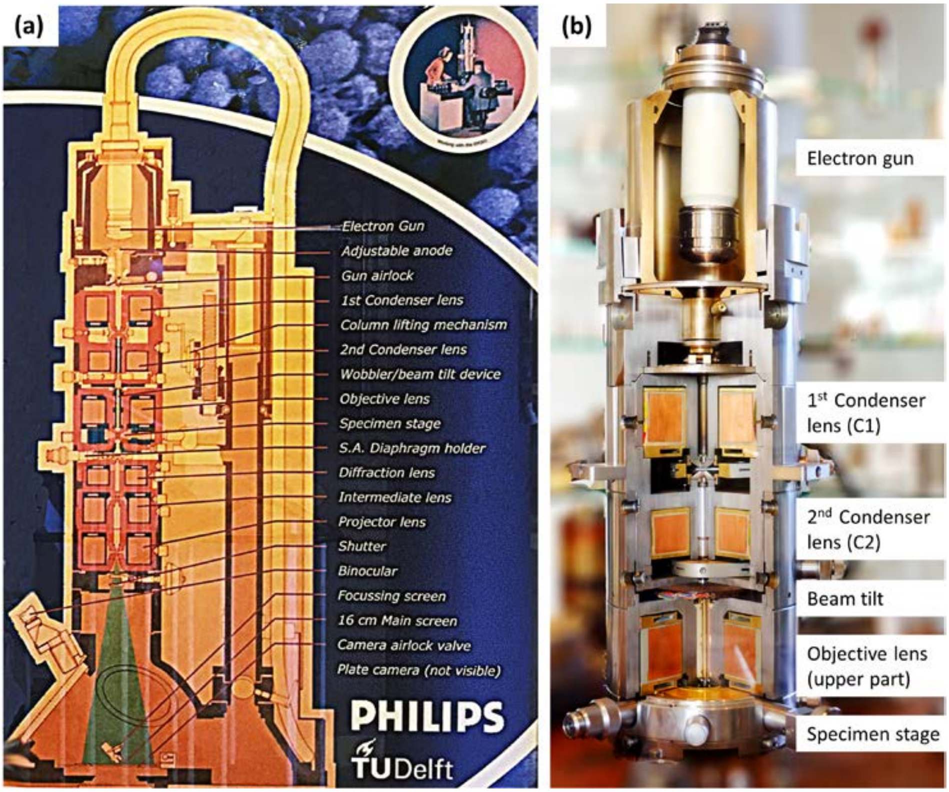

Figure 2.1 (a) Drawing of the cross section of the EM301 TEM, produced by Philips Electron Optics in 1972. It could achieve 3 Å resolution at 100 kV. (b) Cross section of the real TEM column, from the electron gun to the specimen stage. The electron gun is still thermionic, made of a tungsten filament. Courtesy of the Charged Particle Optics group, TU Delft.

2.2.2 Condenser lenses: shaping the electron beam before the specimen

Now that the electrons have reached the target energy, they enter into the second part of the TEM, which consists of the electromagnetic lenses used to shape the electron beam. The coils which are located above the specimen (which is on the electron source side) are called condenser lenses, and their scope is to define the beam characteristics before it hits the specimen. Modern TEM are usually equipped with either two or three condenser lenses, briefly called C1,C2 and C3[*] lens. We just consider the case with all three lenses because it resembles the configuration of the FEI Titan microscope. Beam apertures, which are just metallic plates with a small hole, are located in correspondence of the C1 and C2 lenses, with the hole centered on the beam axis. The combination of C1 lens and C2 aperture has the task to select the beam "spot size", which defines both

---

[*] The C3 lens is also called "upper objective lens", because it is located immediately above the specimen.

the minimum probe size (relevant for STEM imaging) and the beam current. Spot-sizes are conventionally defined with integer numbers, from 1 to 11, with the lowest number corresponding to the highest current and largest probe size. For example, in the specific TEM model used for this thesis (FEI Titan), spot size 1 corresponds roughly to 4.3 nA beam current, while spot size 6 has a modest 300 pA current. Going further in the electron path, the C2 and C3 lenses have different functions depending on the TEM mode of operation. In particular, we can choose between parallel beam illumination, used in bright-field TEM (BFTEM), or converged beam illumination, used in STEM mode. In the parallel beam configuration, both C2 and C3 lenses work together to make the beam parallel to the specimen. In the convergent beam configuration, the C2 lens is turned off and the C3 lens condenses the beam in a small spot on the sample (we will talk about the use of a small probe for STEM imaging in Chapter 2.2.6).

2.2.3 The electron interaction with the specimen

After the condenser lenses and apertures, the electron beam hits the specimen and it gets “scattered” by the atoms and electrons which compose it. If the sample is very thin (compared to the mean free path of the electron in the material), most of the electrons just go through the sample without any energy loss (elastic scattering). The remaining electrons lose part of their energy (inelastic scattering), which is transformed into other forms, such as visible light or X-rays, Auger electrons, electron-hole pairs, collective excitations (plasmons, phonons). Regarding the scattering angle, most electrons are scattered in the forward direction, within a small angle from the beam central axis (typically smaller than 5 mrad). For larger scattering angles, the Rutherford formula for differential cross-section tells us the angular distribution:

$$\sigma_R(\beta) \propto \frac{Z^2}{E_0^2}\frac{1}{\beta^4} \qquad \beta \ll 1 \tag{2.3}$$

where Z is the atomic number, E_0 is the electron beam energy and β is the scattering semi-angle. According to equation (2.3), the number of electrons scattered at high-angles rapidly decreases following a β^4 dependence. We will see in the later sections that, depending on the needs of the TEM operator, it is possible to detect either the electrons scattered with a small β (bright-field imaging), or those scattered at high β (dark-field imaging), and that it is possible to distinguish atoms based on their atomic number Z. All combinations are possible, and deliver complementary information about the specimen.

2.2.4 Objective, intermediate and projection lenses

Immediately below the specimen we find the objective lens[*], whose purpose is to collect the electrons which have been forward scattered, and form an initial image of the

---

[*] Also called “lower objective lens”

sample (the image is inverted after this lens). The lenses which follow the objective lens are called intermediate lenses and projection lens, and they can either by adjusted to visualize a magnified image (Image mode), or to visualize the diffraction pattern (DP) of the sample (Diffraction mode).

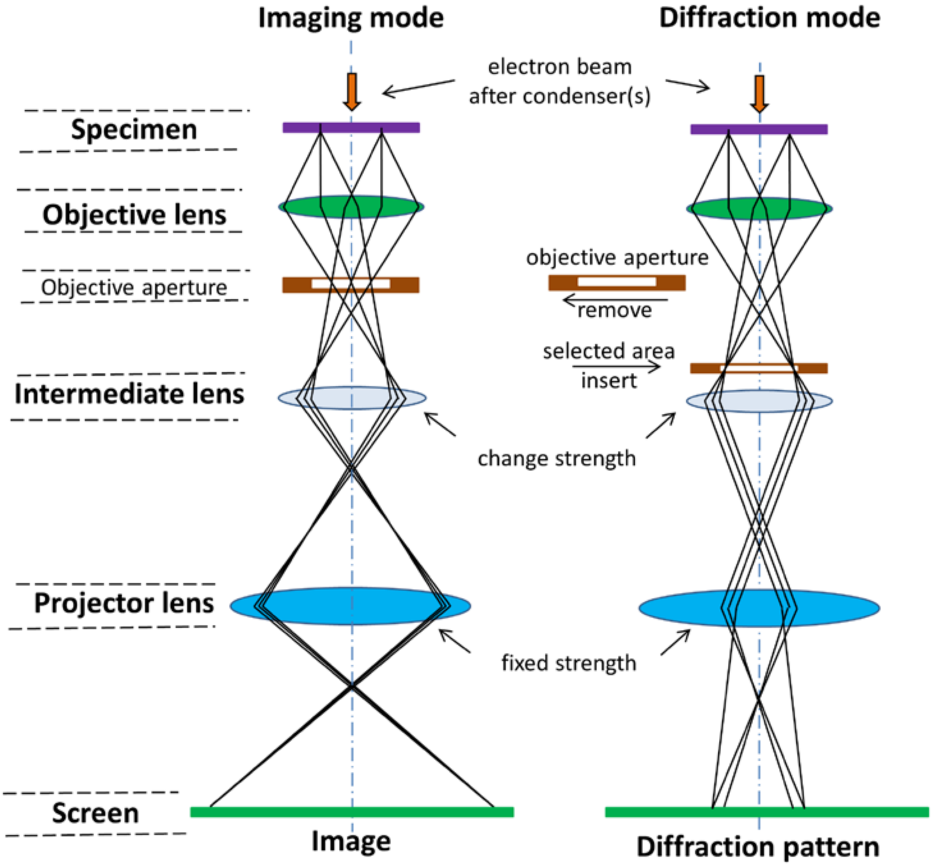

Figure 2.2 Configuration of the microscope in Imaging mode, on the left, and Diffraction mode, on the right.

Figure 2.2 helps us to visualize the two options. In the Image mode, an objective aperture is placed in the back-focal plane of the objective lens and it selects only the electrons which have been scattered within a selected angle range, in a specific direction. As we mentioned before, we speak about bright-field or dark-field imaging depending on the selected angle. In Diffraction mode, the objective aperture is retracted and the selective area aperture is inserted in the image plane after the objective lens. The aperture effectively limits the area of the sample which is used to form the DP. After these two apertures, the combination of intermediate and projection lenses is used to magnify the image. Tuning the strength of the intermediate lens we can either focus the image plane or the back-focal plane (which contains diffraction pattern) onto the final viewing screen, or detector camera.

2.2.5 The image recording system

If we consider the TEM operational mode (we will talk about STEM mode in a dedicated section), there are several ways to record the images. For fast visualization and beam adjustments, a viewing screen is generally used. It consists of a metal plate coated with a fluorescent material, such as ZnS, which absorbs electrons and emits greenish light that can be viewed by naked eye or by a normal TV camera. Despite having a fast response, it has a poor resolution and it is not intended to permanently record images. The viewing screen can be lifted just by pressing a button, which allows the electrons to travel to the next detector in line. In the early times of TEM, this was typically a film coated with photographic emulsion. Advances in silicon technology have made film obsolete, replacing it with digital acquisition sensors, such as Charge-Coupled Devices (CCD). Modern CCDs typically have 4096x4096 pixels, with a maximum acquisition rate of 30 frames per second (fps). The disadvantage of CCD sensors is that they cannot detect any electron with energy higher than 20 keV, which means that the electrons have to be converted into photons via the scintillator, losing efficiency. The most recent development in digital image recording is the CMOS, monolithic active pixel sensor, also known as Direct Electron camera [5]. The CMOS does not need any scintillator, as it can directly detect electrons up to 400 keV (or even more) with a quantum efficiency close to 80%. This means that the same image can be acquired with a much lower electron dose on the sample, or, conversely, that images can be acquired at much higher frame rate (up to 1600 fps) [6].

2.2.6 STEM imaging

Most TEM machines can also work in a different operational regime, called Scanning TEM (STEM)[*]. In STEM, a fine electron beam probe is scanned on the specimen in finite steps; an electron detector, located below the specimen, collects the scattered electrons and sends the signal to a computer, which correlates the beam position to the measured intensity, point by point, to recreate the image. STEM was extensively used in this thesis; therefore we give a more detailed description. Please refer to Figure 2.3 to understand the following part.

As we mentioned in Chapter 2.2.2, the condenser lenses can be used to focus the beam in a small probe, with convergent beam, on the specimen. The C1 lens is used to select the spot size, while the C2 lens is turned off. The C2 aperture, together with the C3 lens, selects the convergence angle α of the beam. Using additional beam deflection coils, located between the C2 and C3 condenser lenses, the probe is scanned on the specimen

---

[*] Actually, there are special microscopes dedicated exclusively to STEM operation

surface. Electrons are scattered through the specimen and reach the objective lens underneath (which has a fixed strength). Then they continue through the intermediate and projection lenses, which are set in the “Diffraction mode”. Contrary to TEM, magnification in STEM is not chosen with the intermediate and projection lenses, which remain fixed in Diffraction mode, but just by modifying the scanned sample area.

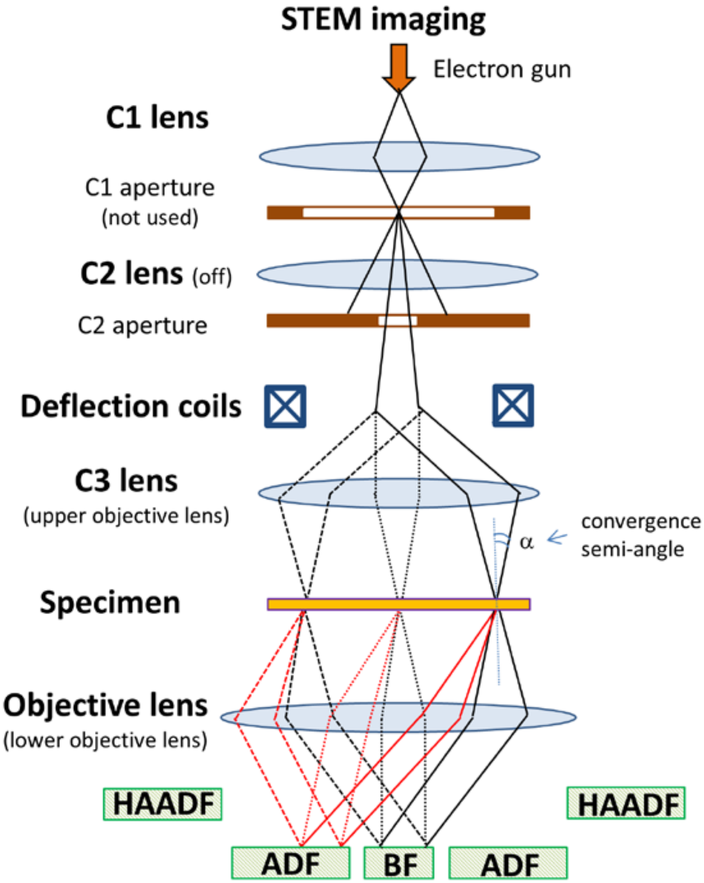

Figure 2.3 Schematic illustration of STEM imaging mode. C1 aperture is not used and C2 lens is turned off. The combination of C2 aperture and C3 lens determines the convergence semi-angle α, which determines the minimum achievable resolution. Below the (lower) objective lens there are the Bright Field (BF), Annular Dark Field (ADF) and High-angle Annular Dark Field (HAADF) detectors.

The STEM imaging detectors are located just above the viewing screen. Depending on their position, we distinguish three types of detectors: the bright-field (BF) is located on the beam central axis, and it collects the electrons scattered with a small semi-angle, also called the “collection semi-angle” ($\beta < 10$ mrad); the annular dark-field (ADF) is an annulus centered on the beam axis, and it collects electrons scattered with an intermediate angle ($10 < \beta < 50$ mrad); the high-angle annular dark-field (HAADF) is finally dedicated to electrons scattered at very high angles ($\beta > 50$ mrad). Keep in mind that 50 mrad=2.86°, so we are still considering very small angles! Moreover, the actual collection angle for each detector can be adjusted changing the so-called "camera length". The camera length is just the virtual distance between the objective lens and the detector, which can be tuned with the intermediate and projection lenses (lenses and detectors positions are fixed in the TEM, it is not a "real" physical movement). For example, on an HAADF detector, a small camera length (D=80 mm) will give a very large collection angle ($\beta > 80$ mrad), while a big camera length (D=560 mm) will give a collection angle comparable to an ADF detector ($11 < \beta < 57$ mrad) [7]. This means that an HAADF detector can be used for dark-field imaging almost at any collection angle (but still not for bright-field).

2.3 Image contrast in (S)TEM

Contrast is, by definition, "the difference in intensity between two adjacent areas", divided by the background intensity[1]. In TEM we distinguish between amplitude and phase contrast. Unless we are dealing with a completely amorphous sample, both types of contrast can contribute to the image formation, revealing complementary information.

Phase contrast refers to any situation where two or more beams contribute simultaneously to the formation of the image, creating periodic variation in intensity, called fringes. For example, if a large objective aperture is used on a crystalline material, several diffraction spots interfere together to form lattice fringes, which represent the periodicity of the crystal structure (this kind of imaging is called high-resolution TEM, HRTEM). Another example of phase contrast are Moiré fringes, which are observed whenever two superposed crystalline structures have a small lattice mismatch, or are slightly rotated respect to each other.

Amplitude contrast refers to all mechanisms that change the image intensity without involving interference. Within this category we distinguish between mass-thickness contrast and diffraction contrast. The first type originates from the elastic scattering (incoherent) in the specimen. If we recall the Rutherford formula from equation (2.3), we see that heavier atoms (higher Z) have a larger cross-section, which means they scatter electrons with higher probability (mass contrast). Since we are considering incoherent scattering, each additional atom that the electron encounters along its path contributes independently to the scattering intensity. Rephrasing the last sentence, more atoms equals more scattering (thickness contrast). But what does more or less scattering actually mean in terms of image contrast? It all depends on which electrons we choose to collect on the detector: if we choose the electrons scattered with small semi-angle ($\beta <$ 5-10 mrad), higher scattering means reduced intensity, thus a darker image (BF imaging); and the opposite is true when collecting electrons with high scattering angle (DF imaging). This concept is valid both in TEM and STEM modes. Finally, diffraction contrast is a special type of DF imaging, which works only on crystalline materials: a specific Bragg-scatterd beam is selected with the objective aperture. The resulting image will appear bright only in the sample areas which share the same crystallographic orientation of the selected diffracted beam.

2.4 Elemental analysis in TEM

In addition to all the imaging techniques that we listed so far, (S)TEM can also provide elemental analysis of the specimen. This is possible thanks to additional detectors, located in different positions of the TEM, which collect information coming from inelastically scattered electrons, either directly (EELS), or indirectly (EDX). We give a brief explanation of both techniques.

2.4.1 Energy Dispersive X-ray (EDX)

One of the possible byproducts of inelastically scattered electrons is the emission of X-rays. Energy levels in atoms are quantized, meaning that electrons can occupy only specific orbits, which are grouped into "shells". These shells are traditionally labelled with letters, K, L, M, N… with K being the innermost shell. When a high-energy electron hits the atom, it may transfer its energy to an electron in the inner shell, expelling it. The vacant position is refilled by one of the electrons sitting in the outer shells, releasing one X-ray photon. The energy of the photon is also quantized, as it depends on the energy difference between the two atomic levels involved in the transition. Since each atomic element in the periodic table has a different shell configuration, the energies of the emitted x-rays (also called "energy spectrum") are a unique fingerprint of the element itself.

X-rays can be detected in TEM using various types of sensors, the most common being Silicon detector, or, more recently silicon-drift detector (SDD). In the latter type, the typical energy range is between 0.1 keV and 30 keV, with a resolution of ~125 eV. The sensitivity of the detector is strongly reduced at low energies, which means that the lightest elements, Berillium and Boron, are harder to detect (Lithium detection is still in study for next generation detectors). If properly calibrated, X-ray detectors can also deliver quantitative information, about the relative abundance of an atomic species in a compound. The X-rays are emitted uniformly from the sample (4π solid angle), which is why, to collect the most signal, the X-ray detector has to be located as close as possible to the specimen. This is usually achieved inserting the detector from one of the side openings on the specimen plane.

X-ray spectra can be acquired both in TEM or in STEM mode, but the largest potential of this technique is achieved with the latter mode. Through the aid of computer software, it is possible to correlate the electron beam position (STEM mode), with the correspondent X-ray spectra. In this manner, an elemental, chemical map of the specimen is created.

2.4.2 Electron Energy Loss Spectroscopy (EELS)

Inelastically scattered electrons are generated by the interaction of the electron beam with the specimen. The analysis of the energy spectrum corresponding to the energy lost in this interaction is called EELS.

The EELS spectrometer is usually located at the bottom of the microscope, together with the image recording cameras. It collects the electrons which are scattered in a small angle (~5 mrad) and it reconstructs their energy spectrum with a magnetic-prism spectrometer. The resolution of the EELS spectra can be tuned selecting the dispersion angle of the prism, but the ultimate, fundamental resolution is given by the energy-spread of the electron gun of the TEM. For a FEG, the best resolution is around 0.3 eV. This can be further reduced to 0.1 eV in high-resolution EELS, which is obtained adding a monochromator after the electron gun, to reduce its energy spread. Notice that this is much higher resolution than EDX spectroscopy, which is limited to ~100 eV.

In practice, what kind of information can we get from the EELS spectra? The first and most basic information is the elemental analysis, following the same physical process described in the EDX section. The energy which is lost by one high-energy electron upon ejecting an inner shell electron is quantized, and typical of each atomic species. This defines the so-called “core-loss” energy range, starting from 50 eV and going up to 2-3 keV. The part of the spectrum below 50 eV is called low-loss region, and it reveals information about the electrons sitting in the outer shells of the atom. This comprises plasmonic excitations, phonon modes, local electron density in semiconductors and metals, band-gap size in semiconductors, etc.

2.5 Application of (S)TEM characterization techniques on 2D materials

We show in this section some examples of how (S)TEM can be used to characterize 2D materials, in particular graphene and black phosphorus. Throughout this thesis we never used “classic” characterization methods, such as Raman spectroscopy or AFM microscopy, to measure the thickness and the amount of defects in our samples. This is because TEM can provide the same information, and even crystallographic orientation, with equal accuracy.

2.5.1 Quantitative mass-thickness contrast in Graphene with STEM

Since graphene has a layered structure, thickness variation always occur in quantized steps, which corresponds to multiples of the one-atom-thick, single layer graphene. Recent publications [8], [9], have shown that it is actually possible to count the number of layers in graphene flake looking at the mass-thickness contrast, using STEM mode with an HAADF detector. To be more precise, the intensity observed on the HAADF detector grows sub-linearly with the thickness, according to the formula[1], [8]:

$$I = A(1 - e^{-\xi d}) \tag{2.4}$$

where ξ and A are fitting parameters, and d is the total thickness. If the graphene flake is thin compared to the inelastic mean free path of the electron (120 nm at 200 keV in diamond), then equation (2.4) can be approximated with a simple linear growth. This approximation has been proven to be acceptable up to a maximum of 30 graphene layers (10 nm thickness in total) [8].

Now we give a practical, step-by-step guide, to calibrate the HAADF intensity respect to the number of layers. We also indicate the settings that we used in our FEI Titan microscope.

1) Choose beam spot-size, C2 aperture and convergence angle according to your preferences. Memorize these settings. If any of them is changed, a new calibration is needed. We use typically spot-size 6, with 300 pA current, 50 μm C2 aperture, 10 mrad convergence angle.
2) Find a suitable sample area: the ideal case is a zone where there is empty space, single layer and multi-layer graphene. Verify the presence of single-layer with Electron Diffraction. Set the sample at the eucentric height (very important!!!).
3) Maximize the signal-to-noise ratio. Since graphene is very thin, the number of scattered electrons is also very small. The best signal is obtained from the bragg-scattered electrons, which are comprised in a small scattering angle around the central, undiffracted beam. If we want to collect those electrons with an HAADF detector, the camera length has to be increased. We use 460 mm camera length, which is the maximum possible value. Further increase of the camera length magnifies the undiffracted beam too much, which then hits the inner radius of the HAADF detector, saturating the signal.
4) With the beam blanked, find the brightness settings of STEM where the average intensity of the image is just below the minimum detectable value of the HAADF detector. This value is 41.25% in our case. Don’t ever change it.
5) Unblank the beam and play with the contrast setting. The optimal value depends on the thickness of the sample. We use 66% contrast for thickness from 1 to 5 layers, 60% from 1 to 15 layers, 55% from 1 to 30 layers. Using a lower contrast increases the detectable range. However, it becomes very difficult to distinguish the layers by naked eye on the screen.
6) For each contrast setting, record the average intensity of the image on the empty-region area, on the single-layer graphene and on any other thicker zone. Plot the number of layers vs intensity and apply a linear fit to extract offset and slope.

Table 2.1 shows the intensity values (on a 8 bit gray scale, from 0 to 255) for different layer numbers and contrasts.

Table 2.1 Image average intensity for various contrast settings, as a function of the number of graphene layers. Values for spot-size 6 (300 pA current), 460 mm camera length. The images are in grayscale, 8bit, thus intensity varies from 0 to 255.

# layers Contrast	0 (vacuum)	1	2	3	4	5	6
66.40%	54.5	87	126	150	181	212	243
60.30%	21	35-37	47-55	67	81	96	111
55.30%	6	13	22	29	36	43	50

2.5.2 Electron Diffraction in Graphene: counting layers

The atomic structure of graphene is usually regarded as “boring” from the crystallographic point of view. The real-space honeycomb lattice gives a simple hexagonal diffraction pattern (DP), when viewed in reciprocal space. Nevertheless, much information can be obtained from the DP. From the position of the diffraction spots we can extract the lattice constant a=2.46 Å. If there are multiple graphene layers stacked with a misorientation, multiple sets of diffraction spots appear, and the rotation angle can be easily measured.

What is most interesting for us is the possibility to distinguish monolayer from multilayer graphene based on the intensity of the diffraction spots. Electron Diffraction pattern of monolayer and multilayer graphene are shown in Figure 2.4 (a)-(b). The dashed rectangles indicate the area where the intensity of the diffraction spots is integrated, which is shown in Figure 2.4 (c)-(d). It can be clearly observed that in monolayer graphene the intensity ratio $I_{\{1100\}}/I_{\{2110\}}$ is >1, while in multi-layer graphene the ratio is < 1 [10], [11]. The distinction is even clearer if the sample is tilted: in monolayer graphene the ratio $I_{\{1100\}}/I_{\{2110\}}$ remains almost unchanged for all tilt angles, while in multi-layer it greatly varies, with some spots disappearing for specific tilt angles [12].

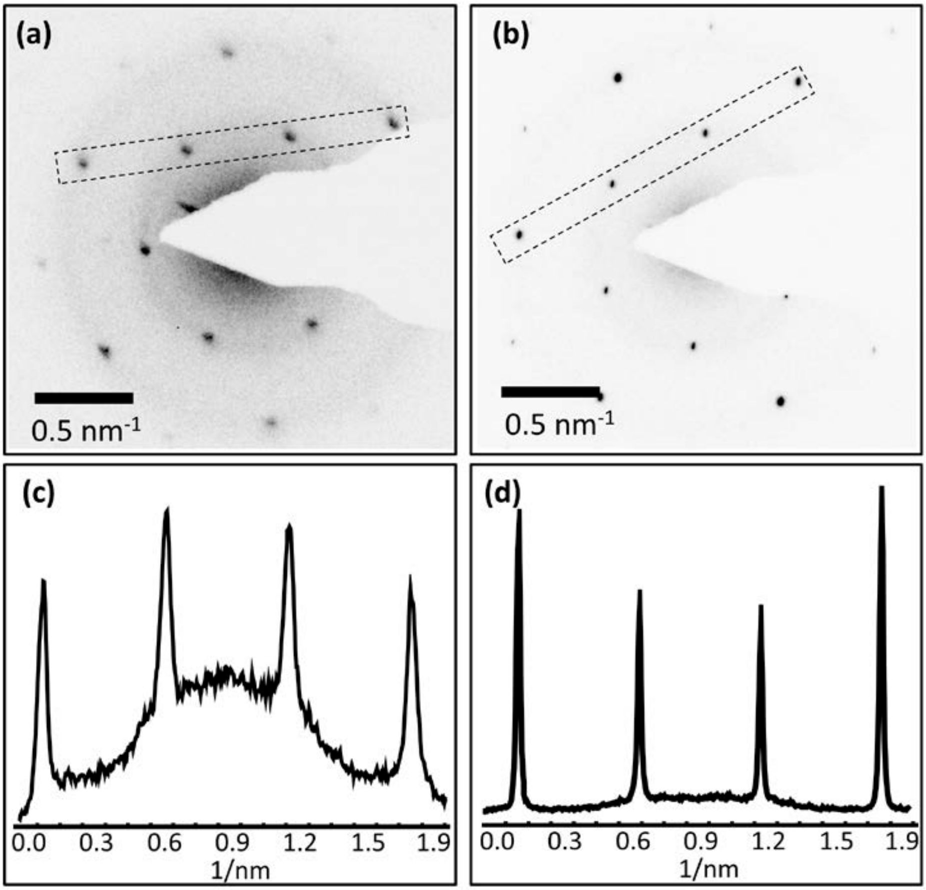

Figure 2.4 (a)-(b) Electron Diffraction pattern of mono and bilayer graphene, respectively. (c)-(d) Intensity profile integrated along the dashed rectangles shown in (a) and (b). In monolayer graphene the {1100} reflections (inner spots) are stronger than the {2110} ones (outer spots). Vice versa in multilayer graphene.

2.5.3 Electron Diffraction in Black Phosphorus: counting layers

Disclaimer: this section has been extracted from the publication [2], removing the parts which are not relevant for this thesis.

… Recent works have demonstrated that black phosphorus, a layered allotrope of the element phosphorus, can be exfoliated similarly to graphite to fabricate few-layer thick sheets [13]–[17] triggering the interest in this new elemental 2D material [18]–[22]. Unlike graphene, few-layer black phosphorus has an intrinsic bandgap, so that field-effect transistors with large current on–off ratios and high mobilities (100–3000 cm^2 Vs^{-1}) can be fabricated [13]–[17]. … In its bulk form, black phosphorus is a direct-gap semiconductor with a 0.33 eV bandgap and mobilities of up to 20000 cm^2 Vs^{-1} at room temperature [23]–[25]. Unlike other allotropes, black phosphorus is characterized by a layered structure: the in-plane bonds are strong and the van der Waals interlayer interaction is weak [26]. The crystal structure of bulk black phosphorus is orthorhombic, with space group Cmca. Note that films with a discrete number of layers there is no translational symmetry along the z axis (out of plane) and thus this configuration cannot be described with space group Cmca. Figure 2.5 shows a representation of the black phosphorus crystalline structure formed by a puckered honeycomb lattice.

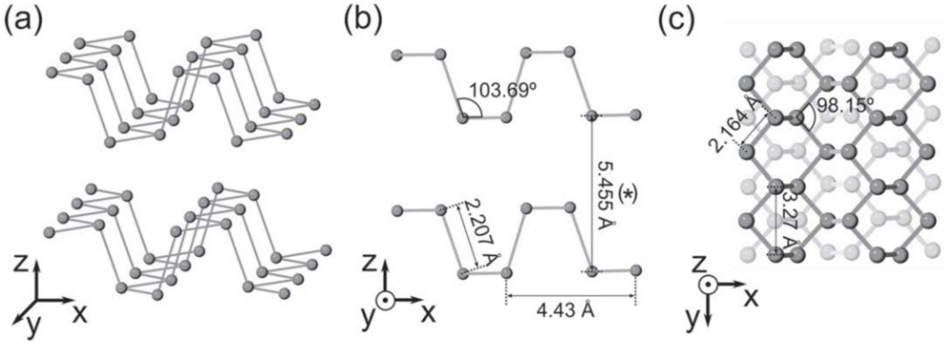

Figure 2.5 Black phosphorus structure. Schematic diagram of the crystalline structure of black phosphorus obtained from the relaxation of the structure using density functional theory calculations (see [2]). The layered structure is composed of sheets with the phosphorus atoms arranged in a puckered honeycomb lattice. Adjacent layers interact by weak van der Waals forces and are stacked following an ABA stacking order. (a) 3D representation. (b) Lateral view. (c) Top view.

… We employed TEM to further characterize the crystallinity of the exfoliated black phosphorus flakes. In order to make possible to use HRTEM, to allow for direct imaging of the atomic structure of the sample, the studied flakes must be freely-suspended. Here we exploit the fact that our fabrication method allows one to transfer the atomically thin black phosphorus flakes onto different substrates, making possible to deposit thin black phosphorus flakes onto silicon nitride membranes with holes [27].

Figure 2.6(a) shows an optical microscopy image of the deposited flake, the thinner part has an optical absorbance of 5.8 ± 0.4% with respect to the Si_3N_4 membrane which corresponds to a bilayer. The sample has been loaded in a transmission electron microscope FEI Titan right after the transfer to avoid sample contamination. The TEM imaging has been carried out at an acceleration voltage of 300 kV. An HRTEM image from a multilayer area of the sample is shown in Figure 2.6(b).

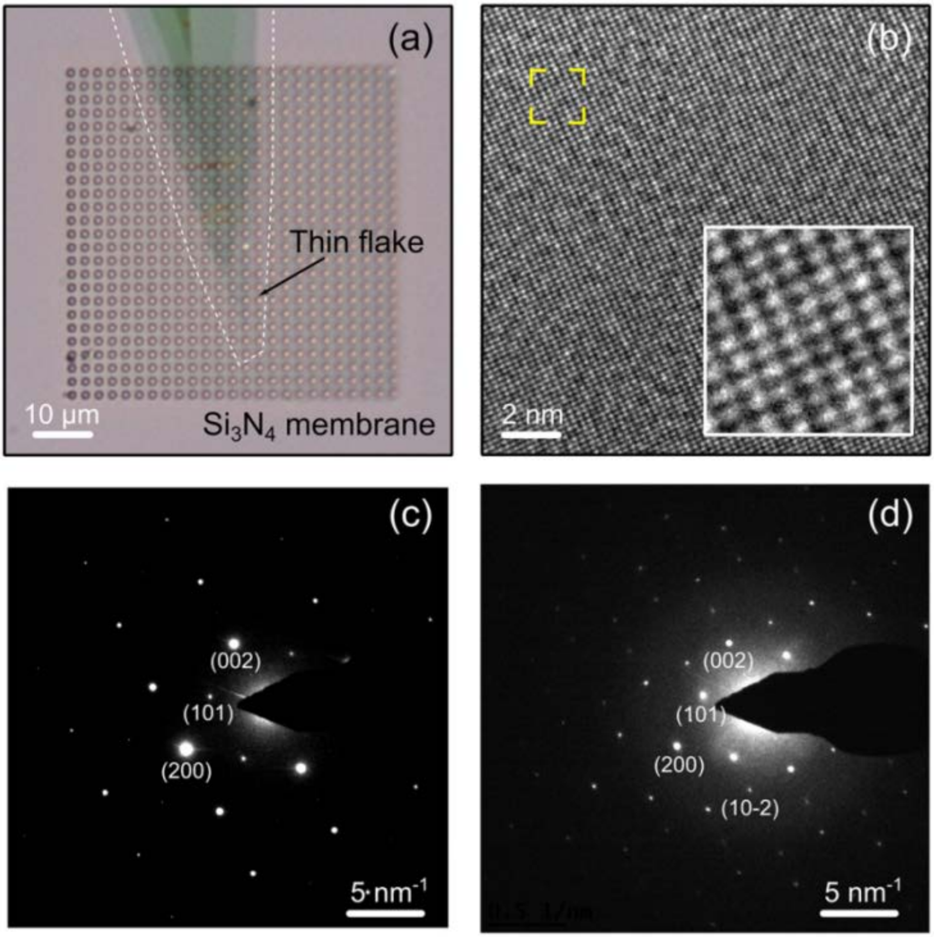

Figure 2.6 Transmission electron microscopy study of few-layer black phosphorus flakes. (a) Optical image of a black phosphorus flake transferred onto a holey silicon nitride membrane. (b) High resolution transmission electron microscopy image of the multilayered region of the flake (~13–21 layers). (c) and (d) are electron diffraction patterns acquired with a 400 nm spot on the thick (~13–21 layers) and the thin (~2 layers) region of the flake.

The uniformity in this image indicates that the lattice contains no extended defects (single vacancies cannot be detected). Therefore, few-layer black phosphorus flakes are stable and crystalline even in free-standing form. Since very thin areas were observed to be very beam sensitive, we chose a very low beam intensity and electron diffraction (ED) with a large illumination area of 400 nm in diameter to study their crystal structure. No serious amorphization of the thin sample was observed. ED patterns were recorded with 0° tilt angle at various locations of the flake. Interestingly, we found that ED patterns depend on the number of layers and thus ED can be employed to determine the thickness of the black phosphorus flakes. We simulated ED patterns finding that the ratio between the 101 and 200 reflections depends on the number of black phosphorus layers as indicated in Table 2.2. Note that the use of the I(101)/I(200) ratio to determine the layer number is only valid if the diffraction pattern is taken from an area with uniform thickness. Figure 2.6(c) and (d) show the diffraction pattern corresponding to a thick region and a thin region of the flake, respectively. In the ED pattern of the thick region we notice strong $h, l = 2n$ reflections and weak $h, l = 2n+1$ reflections. This is consistent with our calculations, as the I(101)/I(200) ratio should be very small for thick black phosphorus flakes if the number is uneven and zero if the number is even. Based on this ratio, we estimated that the thick sample corresponds roughly to 21 layers.

A refinement using MSLS software [28] of this diffraction pattern, using only the reflections with $h, l = 2n$, indicates the thickness to be 7 nm (13 layers circa) with an R-value of 0.001%. In the ED pattern of the thin region we notice that the sum of the intensities of the $h, l = 2n$ reflections is almost equal to that of the $h, l = 2n+1$ reflections. In particular, we measured I(101)/I(200) ratios of 0.29 and 0.42 in two separate positions of the thin region.

Table 2.2 Thickness dependence of the electron diffraction patterns. We display the thickness dependence of the intensity ratio between the 101 and 200 reflections. The experimental data acquired on two spots of the thin flake and one spot of the thicker area has been included for comparison.

Number of layers	I(101)/I(200)
1	2.557
2	0.001
3	0.286
4	0.001
5	0.104
6	0.001
21	0.009
Exp. data thin flake 1	0.31
Exp. data thin flake 2	0.42
Exp. data thick flake	0.01

According to our calculations (see Table 2.2), these values fall in the range corresponding to a thickness of one to three layers. This ratio does not match with a specific value of a single type of layer, and therefore we expect that the thickness of the sample is non-uniform in the illuminated area (circle with 400 nm diameter). For example, an area with 25% of monolayer and 75% of double layer has an the I(101)/I(200) ratio of 0.36. Note that this thickness estimation agrees fairly well with the one obtained from the optical absorbance analysis. Another interesting feature is the presence of ‘forbidden’ reflections $h + l = 2n + 1$ in the thin sample. We measured that these reflections account for 5% of the total intensity of the diffracted beams, almost ten times more than the value expected from the calculations for a monolayer. The presence of these strong forbidden reflections might be explained by the presence of adatoms on the surface of the black phosphorus layer or a slight distortion of the lattice.

References

[1] D. B. Williams and C. B. Carter, *Transmission Electron Microscopy*. Boston, MA: Springer US, 2009.

[2] A. Castellanos-Gomez, L. Vicarelli, E. Prada, J. O. J. O. Island, K. L. L. Narasimha-Acharya, S. I. S. I. Blanter, D. J. D. J. Groenendijk, M. Buscema, G. A. G. A. Steele, J. V. V. Alvarez, H. W. H. W. Zandbergen, J. J. J. Palacios, and H. S. J. H. S. J. Van Der Zant, "Isolation and characterization of few-layer black phosphorus," *2D Mater.*, vol. 1, no. 2, p. 25001, 2014.

[3] K. W. Urban, "Studying Atomic Structures by Aberration-Corrected Transmission Electron Microscopy," *Science (80-.).*, vol. 321, no. 5888, 2008.

[4] R. F. Egerton, "Choice of operating voltage for a transmission electron microscope," *Ultramicroscopy*, vol. 145, pp. 85–93, 2014.

[5] D. Contarato, P. Denes, D. Doering, J. Joseph, and B. Krieger, "High Speed, Radiation Hard CMOS Pixel Sensors for Transmission Electron Microscopy," *Phys. Procedia*, vol. 37, pp. 1504–1510, 2012.

[6] G. McMullan, A. R. Faruqi, D. Clare, and R. Henderson, "Comparison of optimal performance at 300keV of three direct electron detectors for use in low dose electron microscopy," *Ultramicroscopy*, vol. 147, pp. 156–163, 2014.

[7] S. Sadayama, H. Sekiguchi, A. Bright, N. Suzuki, K. Yamada, and K. Kaneko, "High-resolution three-dimensional scanning transmission electron microscopy characterization of oxide-nitride-oxide layer interfaces in Si-based semiconductors using computed tomography," *J. Electron Microsc. (Tokyo).*, vol. 60, no. 3, pp. 243–251, 2011.

[8] F. Q. Song, Z. Y. Li, Z. W. Wang, L. He, M. Han, and G. H. Wang, "Free-standing graphene by scanning transmission electron microscopy," *Ultramicroscopy*, vol. 110, no. 12, pp. 1460–1464, 2010.

[9] M. H. Gass, U. Bangert, A. L. Bleloch, P. Wang, R. R. Nair, and A. K. A. K. Geim, "Free-standing graphene at atomic resolution," *Nat. Nanotechnol.*, vol. 3, no. 11, pp. 676–681, Nov. 2008.

[10] S. Horiuchi, T. Gotou, M. Fujiwara, R. Sotoaka, M. Hirata, K. Kimoto, T. Asaka, T. Yokosawa, Y. Matsui, K. Watanabe, and M. Sekita, “Carbon nanofilm with a new structure and property,” *Japanese J. Appl. Physics, Part 2 Lett.*, vol. 42, no. 9 AB, 2003.

[11] Y. Hernandez, V. Nicolosi, M. Lotya, F. Blighe, Z. Sun, S. De, I. T. McGovern, B. Holland, M. Byrne, Y. Gunko, J. Boland, P. Niraj, G. Duesberg, S. Krishnamurti, R. Goodhue, J. Hutchison, V. Scardaci, a. C. Ferrari, and J. N. Coleman, “High yield production of graphene by liquid phase exfoliation of graphite,” *Nat. Nanotechnol.*, vol. 3, no. 9, pp. 563–8, 2008.

[12] J. C. Meyer, A. K. Geim, M. I. Katsnelson, K. S. Novoselov, D. Obergfell, S. Roth, C. Girit, and A. Zettl, “On the roughness of single- and bi-layer graphene membranes,” *Solid State Commun.*, vol. 143, no. 1–2, pp. 101–109, 2007.

[13] M. Buscema, D. J. Groenendijk, S. I. Blanter, G. A. Steele, H. S. J. Van Der Zant, and A. Castellanos-Gomez, “Fast and broadband photoresponse of few-layer black phosphorus field-effect transistors,” *Nano Lett.*, vol. 14, no. 6, pp. 3347–3352, 2014.

[14] L. Li, Y. Yu, G. J. Ye, Q. Ge, X. Ou, H. Wu, D. Feng, X. H. Chen, and Y. Zhang, “Black phosphorus field-effect transistors.,” *Nat. Nanotechnol.*, vol. 9, no. 5, pp. 372–7, 2014.

[15] H. Liu, A. T. Neal, Z. Zhu, Z. Luo, X. Xu, D. Tománek, and P. D. Ye, “Phosphorene: An Unexplored 2D Semiconductor with a High Hole Mobility,” *ACS Nano*, vol. 8, no. 4, pp. 4033–4041, Apr. 2014.

[16] F. Xia, H. Wang, and Y. Jia, “Rediscovering black phosphorus as an anisotropic layered material for optoelectronics and electronics,” *Nat. Commun.*, vol. 5, Jul. 2014.

[17] S. P. Koenig, R. A. Doganov, H. Schmidt, A. H. Castro Neto, and B. Özyilmaz, “Electric field effect in ultrathin black phosphorus,” *Appl. Phys. Lett.*, vol. 104, no. 10, 2014.

[18] J. Qiao, X. Kong, Z.-X. Hu, F. Yang, and W. Ji, “High-mobility transport anisotropy and linear dichroism in few-layer black phosphorus,” *Nat. Commun.*, vol. 5, Jul. 2014.

[19] A. S. Rodin, A. Carvalho, and A. H. Castro Neto, “Strain-Induced Gap Modification in Black Phosphorus,” *Phys. Rev. Lett.*, vol. 112, no. 17, p. 176801, May 2014.

[20] R. Fei and L. Yang, "Strain-Engineering the Anisotropic Electrical Conductance of Few-Layer Black Phosphorus," *Nano Lett.*, vol. 14, no. 5, pp. 2884–2889, May 2014.

[21] V. Tran, R. Soklaski, Y. Liang, and L. Yang, "Layer-controlled band gap and anisotropic excitons in few-layer black phosphorus," *Phys. Rev. B*, vol. 89, no. 23, p. 235319, Jun. 2014.

[22] J.-W. Jiang and H. S. Park, "Negative poisson's ratio in single-layer black phosphorus," *Nat. Commun.*, vol. 5, Aug. 2014.

[23] D. Warschauer, "Electrical and Optical Properties of Crystalline Black Phosphorus," *J. Appl. Phys.*, vol. 34, no. 7, p. 1853, 1963.

[24] Y. Akahama, S. Endo, and S. Narita, "Electrical Properties of Black Phosphorus Single Crystals," *J. Phys. Soc. Japan*, vol. 52, no. 6, pp. 2148–2155, Jun. 1983.

[25] A. Morita, "Semiconducting black phosphorus," *Appl. Phys. A Solids Surfaces*, vol. 39, no. 4, pp. 227–242, Apr. 1986.

[26] A. Brown and S. Rundqvist, "Refinement of the crystal structure of black phosphorus," *Acta Crystallogr.*, vol. 19, no. 4, pp. 684–685, 1965.

[27] A. Castellanos-Gomez, M. Buscema, R. Molenaar, V. Singh, L. Janssen, H. S. J. van der Zant, and G. A. Steele, "Deterministic transfer of two-dimensional materials by all-dry viscoelastic stamping," *2D Mater.*, vol. 1, no. 1, p. 11002, Apr. 2014.

[28] "The ELSTRU software package with the MSLS refinement program is available at http://nchrem.tnw.tudelft.nl/elstru/." .

CHAPTER 3

Controlling defects in graphene for optimizing the electrical properties of graphene nanodevices

This chapter is extracted from the publication in [1]. It is a perspective focused on defects in graphene and related in-situ TEM experiments.

Structural defects strongly impact the electrical transport properties of graphene nanostructures. Here, we give a brief overview of different types of defects in graphene and their effect on transport properties. We discuss recent experimental progress on graphene self-repair of defects, with a focus on in-situ transmission electron microscopy studies. Finally, a future outlook for graphene self-repair and in-situ experiments is presented.

3.1 Defects and electrical transport in graphene

Ideal graphene is a one-atom-thick layer of carbon atoms that are perfectly arranged in a two-dimensional honeycomb lattice. Each carbon atom is coordinated with other three carbon atoms, with identical 120° in-plane bonding angles. The presence of structural defects breaks this perfect symmetry, and opens a whole research area for studying their effect on mechanical, electrical, chemical and optical properties of graphene. Sometimes their effect is beneficial. For example, defects are essential in chemical and electro-chemical studies, where they create preferential bonding sites for adsorption of atoms and molecules, which can be used for gas and liquid sensing. On the other hand, defects pose a problem for electronics applications such as Field-Effect Transistors and electrical interconnects, because they can significantly lower the charge carrier mobility and thus increase the resistivity of graphene [2]–[5]. While this is the general rule, there are also some exceptions where defects can be engineered in regular arrays to yield metallic or insulating states [6], [7].

Given their crucial impact on graphene properties, it is important to control defect formation and, if possible, find ways to repair existing defects. Important progress in this direction has recently been reported, where several in-situ Transmission Electron Microscopy (TEM) experiments have observed self-repair of graphene heated at high temperatures (>500°C)[8]–[10]. TEM is, in fact, the perfect tool for this kind of studies, as it combines atomic resolution with capabilities such as in-situ heating and in-situ electrical measurements. With this approach, correlating defects and electronic transport becomes a manageable task, as the experimenter can determine defects with atomic resolution and simultaneously measure the conductivity.

First, we provide an overview of the types of defects that are present in graphene, and we briefly discuss their effect on the electron transport properties with an emphasis on graphene nanoribbons.

3.1.1 Defects in graphene

In graphene, we can distinguish vacancy, impurity and topological defects. In a vacancy defect, one or more atoms are removed from the lattice. In an impurity defect, one carbon atom is replaced by another atom of a different element. In a topological defect, no atom is removed from the lattice, but the bonding angles between the carbon atoms are rotated.

Vacancy defects in graphene are not easily formed. The energy required to sputter (or “knock-on”) a single atom out of the lattice is 18-20 eV [11]. Such energy can be provided by bombarding ions in a plasma, or by electrons with an energy >86 keV, which is typically achievable in a TEM (high energy electrons are needed because of the large mass difference between the electron and the carbon atom, which sets the maximum transferable energy [12]). This kind of vacancy defects act as strong scattering centers for the charge carriers in graphene, decreasing the localization length and disrupting the ballistic nature of electronic transport in graphene. For a low and medium vacancy defect density (10^{10}-10^{12} cm^{-2}, or 0.01-0.1% of the total area), mobility reduction is generally observed [13].

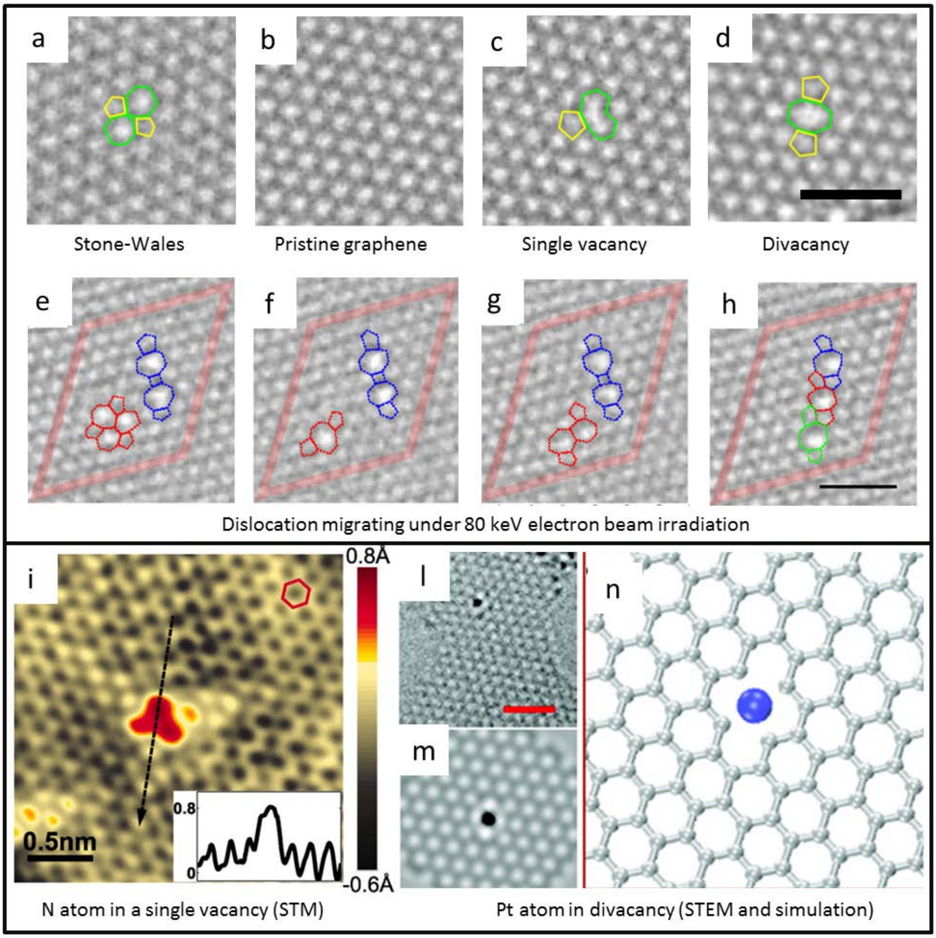

Figure 3.1 Structural defects in graphene. (a-d) HRTEM images of (a) Stone-Wales defect, (b) defect-free graphene, (c) single vacancy with 5-9 rings, (d) divacancy with 5-8-5 rings. Scale bar is 1 nm. (e-h) HRTEM image sequence of divacancy migration observed at 80 keV. Scale bar is 1 nm. Reprinted with permission from ref [15]. Copyright 2011 American Physical Society. (i) STM image of a single N atom dopant in graphene on a copper foil substrate. (Inset) Line profile across the dopant shows atomic corrugation and apparent height of the dopant. Reprinted with permission from ref[17]. Copyright 2011 American Association for the Advancement of Science. (l,m) HRTEM images of a Pt atom trapped in divacancy and (n) simulated HRTEM image for the Pt-vacancy complex. Scale bar is 1 nm. Reprinted from ref[16].

For a high defect density ($>10^{13}$ cm^{-2}, 1% of the area) , Anderson insulating behavior is predicted to develop [5]. An example of a single-atom vacancy is shown in Figure 3.1(c). The missing atom causes the lattice to rearrange in a 5 carbon atom ring (5-ring) plus a 9-ring. The sp-2 hybridization is broken, leaving one dangling bond unsaturated. Single vacancies can migrate and merge in divacancies. Such migration has a low activation energy (1.3 eV) and should already be observed at 200°C [14] (to our knowledge, single vacancy migration has not been recorded in any experiment yet). Instead, divacancies (shown in Figure 3.1(d)) need to overcome a larger energy barrier to migrate (5-6 eV), which makes them much more stable than single vacancies[14], [15]. Divacancy migration was observed by Kotakoski et al.[15], under the influence of an 80 keV electron beam in a TEM (see Figure 3.1(e-h)). The migration involved only carbon bond rotation, no additional vacancies were created.

Whenever a vacancy is formed in graphene, an external element can replace the missing atom and fill the void in the lattice, forming an impurity defect. Single vacancies are ideal trapping sites for the small atoms, such as B and N, while noble and transition metals, with larger atomic radii, prefer to rest on multi-vacancies[16]. Zhao et al.[17] obtained chemical-vapor deposition (CVD) graphene with N impurities by adding ammonia (NH_3) as a precursor during the growth process. A high density of N atoms was obtained (0.34% of C atoms), which resulted in a considerable n-type doping of graphene. As it can be seen from the STM images shown in Figure 3.1(i), each N atom replaced a single C atom in the lattice, creating a perturbation in the local density of states which rapidly decayed in space (~7 Å radius around the N atom). Conversely, Wang et al.[16] created vacancies in graphene with pulsed laser deposition and implanted different elements (Pt, Co, and In) afterwards. In this case, the doping has been theoretically predicted to depend on the work function of the guest element (p-type if higher than the graphene work-function, n-type otherwise). Figure 3.1(l-n) show an example of a Pt atom trapped in a di-vacancy. The binding energy of the platinum atom in this configuration is 6 eV, which also makes it stable for prolonged TEM observation at low voltage (60 keV).

Finally, we consider topological defects in graphene. The simplest one is a single disclination, i.e., the presence of a 5-, or 7-ring that alters the regular 6-ring structure (see Figure 3.2(a),(b)). Isolated disclinations are highly unlikely to develop in single layer graphene, because they require an out-of-plane bulging of the graphene sheet, and therefore have a high formation energy[18]. Dislocations are a combination of two or more complementary disclinations. The most basic dislocation is composed by a 5-7 ring pair, as shown in Figure 3.2 (c). Another interesting and frequently occurring dislocation is the Stone-Wales defect, which is composed of two 5-7 ring pairs (shown in Figure 3.1(a)).

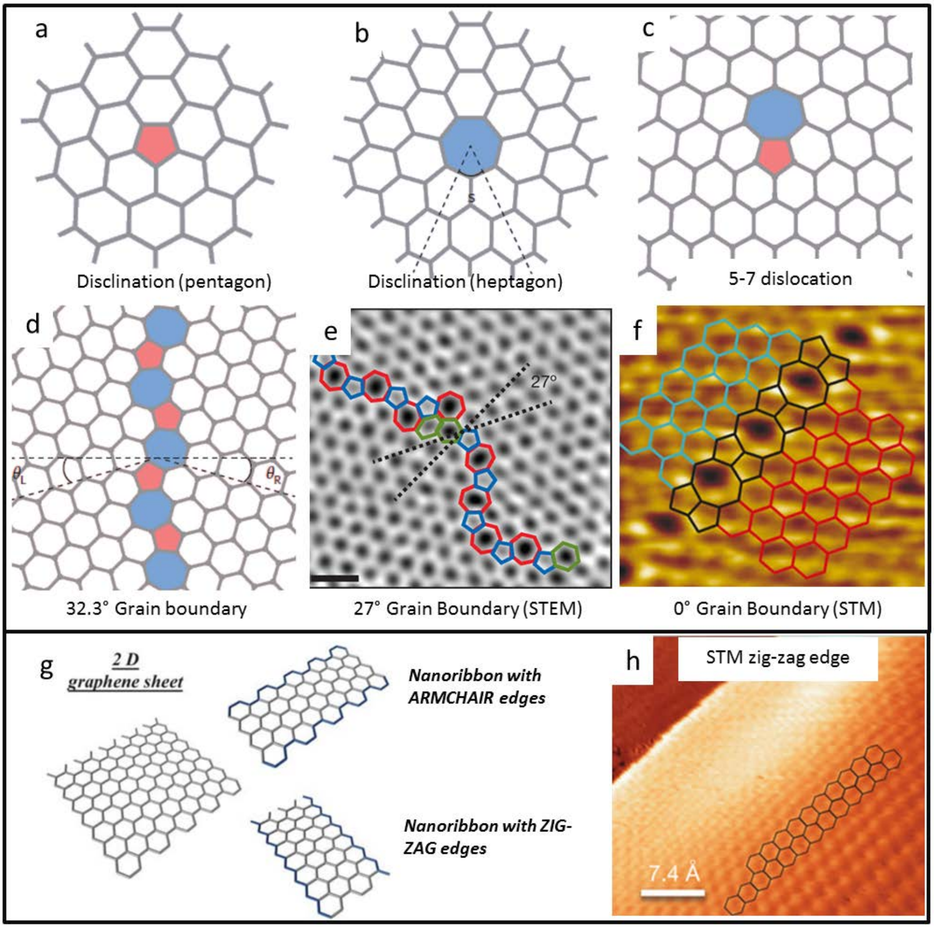

Figure 3.2 (a-f) Topological defects in graphene. (a,b) 5 ring and 7 ring disclinations, (c) 5-7 dislocation, (d) grain boundary with θ =32.3° misorientation angle. Reprinted with permission from ref [18]. Copyright 2014 Nature Publishing Group. (e) Aberration-corrected annular dark-field scanning TEM of a grain boundary with θ =27° misorientation angle. Scale bar is 0.5 nm. Reprinted with permission from ref [20]. Copyright 2011 Nature Publishing Group. (f) STM image of a 0° grain boundary, formed by 5 and 8 carbon atom rings. Reprinted with permission from ref[6]. Copyright 2010 Nature Publishing Group. (g) Zig-zag and armchair edges in monolayer graphene nanoribbons. Reprinted with permission from ref [21]. Copyright 2010 Royal Society of Chemistry. (h) Atomic resolution STM image of graphene edge structure on the sloped sidewall of SiC. Reprinted with permission from ref [22]. Copyright 2014 Nature Publishing Group.

The most prominent example of extended dislocations are grain boundaries (GB). GBs are formed in graphene whenever two separate domains (grains), with a different crystallographic orientation, are linked together. Figure 3.2(d,e) show examples of a GB that connects two grains which are rotated by 32.3° and 27°, respectively. Experiments conducted on CVD grown graphene have shown that GBs degrade the electronic transport in graphene. Tsen et al. [3] have measured that a single GB has a resistivity of 0.5 to 4 kΩ-µm, depending on the position of the Fermi level in the graphene grains. GBs are usually intrinsically n-type doped, while the surrounding graphene can be either n- or p- type. In the latter case, a sharp p-n junction is formed, which leads to a yet larger resistance. A special case of GB with zero rotation angle (see Figure 3.2(f)) was experimentally investigated by Lahiri et al.[6]. In this case the GB resembles a linear, periodic chain of 5-8 rings and it has a metallic nature (i.e. non-zero density of states at the Fermi level).

The interested reader can find more information on structural defects in graphene in three recent reviews on the topic [14], [18], [19].

3.1.2 Edge defects in graphene nanoribbons

A graphene nanoribbon (GNR) is a narrow strip of graphene (width ranging from 1 to 100 nm) with a large length to width ratio. When the width of the nanoribbon is reduced below 20 nm, a sizeable band gap can be opened in the band structure. The size of this band gap has been theoretically predicted to be in the 0.2-1.5 eV range[23], depending both on the GNR width and on its edge orientation (zig-zag or armchair, see Figure 3.2 (g)). The presence of a band gap makes GNRs good candidates for replacing traditional semiconductors in electronic devices such as Field Effect Transistors, tunnel barriers, and quantum dots.

Depending on the method adopted for GNRs fabrication, the experimental band gap and mobility differ quite radically from the predicted values. The explanation for this behavior is mainly given by the presence of defects on the GNR edges, which alter the normal zig-zag or armchair edge profiles and create localized states along the length of the GNR. This happened for example in fabrication using electron-beam lithography, followed by oxygen plasma etching, which yields GNRs with rough edges. Stampfer et al.[4] have shown that a GNR fabricated following such method behaves as a series of quantum dots, which gives an “effective energy band gap” of 110-340 meV, roughly ten times higher than the predicted value (8 meV) in a 45 nm wide GNR. On the other hand, a recent experiment by Baringhaus et al.[22] showed ballistic transport in GNR grown on the sidewalls of etched steps in SiC. As revealed by STM images (see Figure 3.2 (h)), these GNRs have a well-defined edge orientation and are mostly defect-less, which means that the charge carriers can travel a long distance (mean free path ~16 µm) before undergoing inelastic scattering.

These, and many other experiments, highlight the importance of controlling the quality, and the orientation, of GNR edges. For more details on GNRs, their edges and fabrication methods, we point the reader to specific reviews[21], [24].

3.2 Graphene self-healing and recrystallization

Graphitization of thin carbon films (i.e., the process of graphite formation from amorphous carbon) was extensively studied in the 1980s [25]. These experiments were carried out ex-situ, where each sample was individually heated at a fixed temperature and imaged afterwards in a TEM. It was found that graphitization takes place progressively in a temperature range of 2000°C- 3000°C. Almost 30 years later, prompted by the renewed interest in graphene, the topic of lattice recrystallization (or “healing”) was addressed with more modern, practical, in-situ approaches. Here we present four recent in-situ (S)TEM experiments that use different approaches to achieve graphene lattice recrystallization. These include ultra-high vacuum (UHV) healing [26], silicon-assisted growth [8], high-temperature healing [27] and recrystallization by Joule heating [10]. We emphasize that, to achieve atomic resolution imaging, graphene is always freestanding in these experiments.

3.2.1 Graphene ultra-high vacuum healing and metal catalyzed etching at room-temperature

In the research conducted by Zan and collaborators [26], Ni and Pd metal particles were evaporated on top of CVD graphene and imaged with a STEM microscope in UHV ($6x10^{-9}$ mbar). Under the effect of 60 keV electron beam scanning, these metal particles acted as catalysts for etching holes in the graphene surface (see Figure 3.3(a,b)). In fact, the low energy of the electron beam itself would not be sufficient to create new vacancies in the bulk lattice (as the threshold for knock-on damage of single carbon atoms in graphene is 86keV[11]), but it could be enough to displace atoms at graphene edges. The threshold for removing atoms at the edges has been calculated to be 62 keV (zig-zag profile) [28], which could be further lowered by the presence of the metal catalysts.

Without the metal particles, the authors observed re-filling and repairing of the holes, under the same electron beam irradiation. As the whole experiment was conducted at room temperature, any heat-related repair process can be discarded. The authors concluded that the scanning electron beam could dislodge carbon adatoms from the graphene surface, and drag them to the edge of the holes. There, they could rearrange in a random combination of 5,6,7 or 8 carbon atom rings and refill the hole (see Figure 3.3(c)).

3.2.2 Silicon-assisted growth of graphene at high temperature

In another experiment, Liu et al. [8] observed silicon-catalyzed graphene growth. A STEM microscope (operated at 60 keV) in high vacuum ($1x10^{-7}$ mbar) was used to image CVD bilayer graphene, and simultaneously heated to 500°C with an in-situ TEM heating holder. The carbon needed for the growth originated from the hydrocarbons in the vacuum chamber of the microscope, after being decomposed on graphene by the electron beam (no growth was observed in areas not exposed by the electron beam).

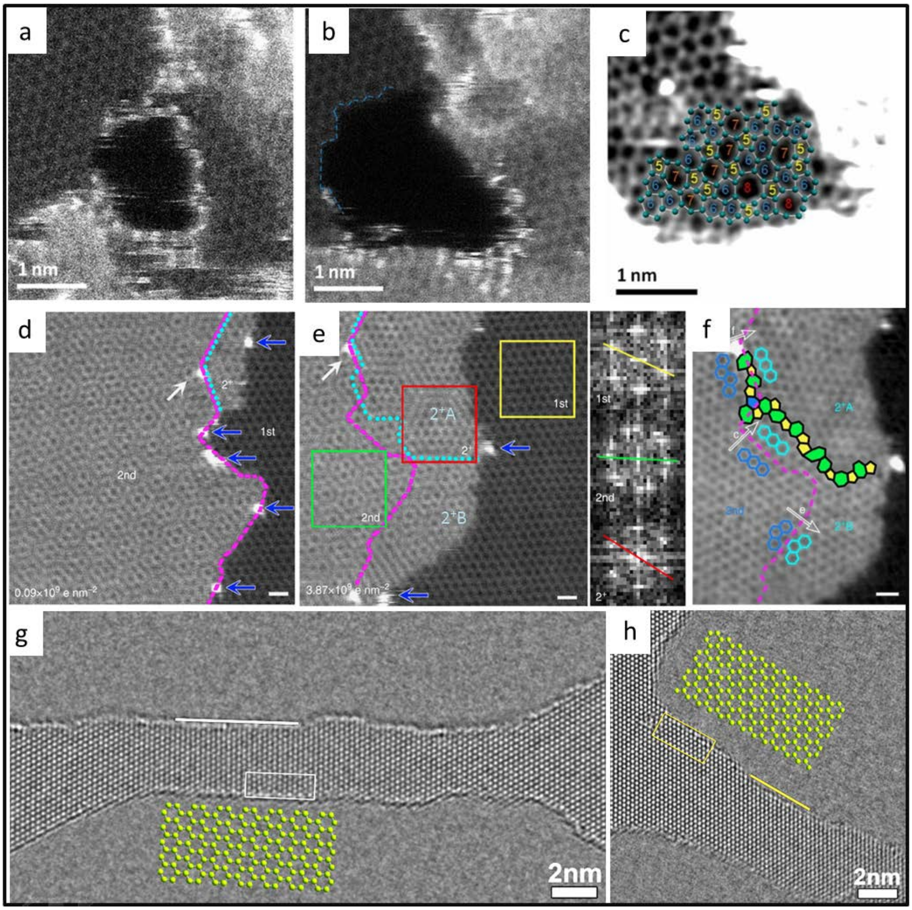

Figure 3.3 Graphene self-repair experiments. (a-c) Aberration-corrected high-angle annular dark-field scanning TEM (@60 keV) images showing (a) an hole etched in graphene that is decorated with Pd atoms, (b) the stabilization of the hole in the absence of Pd atoms at the edge, and (c) the hole refilling with 5,6,7 and 8 carbon atom rings. The sample is at room temperature, in ultra-high vacuum. Reprinted with permission from ref [26]. (d-f) Aberration-corrected annular dark-field scanning TEM (@60 keV) images showing (d) a graphene area which is single layer on the right side and bilayer on the left, (e) the same area after a cumulative electron dose of 3.87×10^{9} e nm^{-2}. The inset shows the Fourier transform images corresponding to the 1st (yellow box), 2nd (green box) and 2^{+} (red box) layer of graphene. (f) A detail of the previous picture, showing the grain boundary formed between the newly grown graphene (2^{+}A and 2^{+}B) and the original 2nd layer. The sample is heated to 500°C. Scale bar is 0.5 nm. Reprinted with permission from ref [8]. Copyright 2014 Nature Publishing Group. (g-h) HRTEM images of nanoribbons in monolayer graphene sculpted at 300 keV at 600°C and imaged at 80 keV at 600°C. The ribbons in (g) and (h) are oriented respectively along the $\langle 1\bar{1}00\rangle$ and $\langle 1\bar{2}10\rangle$ direction. White and yellow lines indicate armchair and zig-zag edges, respectively. Atom structure models for armchair and zig-zag edges, outlined with open frames in the corresponding images, are enlarged and overlaid. Reprinted with permission from ref [27].

In contrast to the previously discussed experiment [26], room temperature imaging did not result in hole re-filling, but simply in amorphous carbon deposition. This can be explained by the different vacuum conditions of the two microscopes: in worse vacuum conditions there are more hydrocarbons available, resulting in a higher beam-induced carbon deposition rate. If this rate is too high, carbon atoms cannot form covalent bonds and keep accumulating in amorphous layers. Water molecules on graphene surface (not completely removed in high-vacuum) may also play a role in this process, catalyzing the deposition of amorphous carbon.

An example of the observed graphene growth is shown in Figure 3.3(d-f) . Looking at Figure 3.3(d), the 1st layer area on the right is gradually covered by a 2nd layer of graphene, extending from the left side. Silicon atoms (blue arrows) catalyze the growth and are pushed to the outermost edges of the newly formed graphene. As the authors explain, the graphene can either grow in the same crystal orientation as the seeding layer (layer 2^+B in Figure 3.3(e,f)), or it can be rotated by 30° (layer 2^+A). In the latter case, a grain boundary is formed. The rotation is caused by the presence of 5-7 edge defects in the original seeding layer, before the growth had started. This proves that in few-layer graphene heated at 500°C, the growing orientation mainly follows the edge structure, rather than the energetically favorable AB stacking.

3.2.3 Graphene STEM sculpting at high temperature

In the third experiment that we present, Xu *et al.*[27][*] used the STEM electron beam to sculpt graphene nanoribbons with 2 nm width and crystalline edges with defined orientation. In this case, the microscope was operated at 300 keV in order to physically knock the carbon atoms away from the lattice. Graphene was simultaneously heated to 600° C using a dedicated in-situ TEM holder. During the imaging process, the electron beam scanned the graphene surface with a short dwell time (10 µs). This only rarely created vacancies in the lattice, which were instantly repaired by refilling with carbon adatoms (highly mobile at 600°C) present on the surface of graphene. When the dwell time was increased (10 ms), the beam-induced damage extended beyond repair, and a hole was formed in the graphene. Using a computer script to slowly move the beam along a pre-defined path, the authors could pattern graphene nanoribbons and nanopores with sub-nm accuracy. The edges of the patterned nanostructures maintained their crystalline structure because of the 600°C temperature. Figure 3.3(g,h) show an example of two graphene nanoribbons, sculpted following either zig-zag or armchair direction, exhibiting atomically sharp edges. This paper, rather than presenting a new graphene repair mechanism, exploits the high-temperature healing effects to achieve maskless, resist-free and defect-free graphene patterning. With a few modifications, the method could also be extended to industrial e-beam lithography machines.

---

[*] This work was published before the beginning of this Phd project. It developed the graphene sculpting technique which is at the base of our project.

3.2.4 Graphene nanoribbon edge recrystallization induced by Joule heating

In a recently published paper [10], Qi and his co-workers correlate, in real-time, the conductivity of a graphene nanoribbon with its crystallinity, which is monitored at the atomic scale with High Resolution TEM imaging. Starting from a 8 nm wide multilayer graphene nanoribbon with rough edges (see Figure 3a in ref.[10]), an increasing voltage (2-3 V) is applied across it, resulting in Joule heating and local temperatures that exceed 2000 K. This heating induces recrystallization of the nanoribbon edges, which rearrange along either zig-zag or armchair profile (see Figure 3b-d in ref.[10]). As the voltage is increased and the temperature rises, the edges become smoother, the ribbon width shrinks, and the number of layers decreases (see Figure 3e-g in ref.[10]). This recrystallization resulted in an overall increase in conductivity, despite the reduced width of the ribbon (see Figure 5a,b in ref.[10]). This is an important, direct experimental confirmation of the influence of edge roughness and lattice crystallinity on graphene electronic transport.

To further explain the mechanism of edge smoothing induced by Joule heating, Monte-Carlo simulations were implemented. It was found that junctions between edges with different orientation (zig-zag or armchair) develop a larger electrical resistance, which results in a higher local heat dissipation and thus, temperature. Consequently, any edge protrusion was subject to a fast recrystallization, and promptly flattened into a smooth edge.

One consequence of recrystallization induced by heating (either external or Joule), is the systematic formation of bonded edges. Any open edge in a bilayer, or multilayer, graphene sheet will “fuse” with the closest free edge available, as shown in Figure 2a-f from ref.[10]. For electro-chemical studies, this could represent a disadvantage because there are no dangling bonds available for chemical functionalization. On the other hand, bilayer graphene nanoribbons with closed edges could, in theory, have a finite band gap (up to 0.25 eV), depending on the twist angle between the two layers.

As a final remark, we note that a similar experiment was performed a few years ago by Jia et al[29]. However, in that experiment there was no correlation between width and conductivity of the sample, nor any consideration on the number of graphene layers or the presence of bonded edges.

3.3 Outlook and future challenges

Different repair mechanisms of defects in graphene have been observed. Most of them are based on high temperature annealing (>500°C) and they require a carbon source to be initiated. The carbon is usually available as free adatoms on graphene surface, but it can also be provided by the hydrocarbons present in the vacuum chamber of the TEM. Controlled Joule heating can be used to recrystallize the rough edges of plasma etched graphene nanoribbons, where the current flowing through the nanoribbons is regulated in order to induce self-repair, without causing physical breakdown.

The results obtained by Qi *et al.* [10], highlight that in-situ TEM is the optimal instrument to study the effects of lattice repair on graphene conductivity. With small modifications, the experiment could be repeated on single layer graphene and other two-dimensional materials, such as layered transition metal dichalcogenides (MoS_2, WSe_2, $MoSe_2$, WS_2, etc.), phosphorene, silicene, and many others.

While the current focus of the field is on controlling the annealing processes in such a way that one can make defect-free graphene nanostructures, a next stage will likely be to deliberately create single defects within perfect graphene (e.g., a small pore, a single step in a zigzag edge, or replacing a single C atom by a Pt atom) with the same level of perfection. This opens up many applications from electronic devices to catalysis. For example, with STEM one could create a vacancy inside a graphene nanoribbon at a pre-chosen site, refill it by a Si or Pt adatom, and subsequently explore the interaction of a single Pt atom with H_2 or other gases in an environmental TEM.

To fabricate graphene nanostructures, the fine probe of STEM can be optimally used for sculpting on an atomic level and in any shape, with higher precision than conventional TEM. To verify what has been made, one can use the same STEM, but with a voltage below the knock-on energy. Thus, for optimal operation one needs a STEM that can rapidly switch from 100 keV (sculpting) to 60 keV (imaging). An interesting geometry to sculpt in graphene would be a nanoribbon with a nanopore in its center. In fact, it has been hypothesized that this configuration could be used for sequencing DNA with single-base resolution [30].

These and other future experiments will pave the way for the fabrication of reliable, defect-controlled graphene devices. In-situ TEM plays a crucial role in this expedition, as it provides a wonderful workbench for real-time graphene engineering.

References

[1] L. Vicarelli, S. J. Heerema, C. Dekker, and H. W. Zandbergen, “Controlling Defects in Graphene for Optimizing the Electrical Properties of Graphene Nanodevices,” *ACS Nano*, vol. 9, no. 4, pp. 3428–3435, Apr. 2015.

[2] J. Haskins, A. Kınacı, C. Sevik, H. Sevinçli, G. Cuniberti, and T. Çağın, “Control of Thermal and Electronic Transport in Defect-Engineered Graphene Nanoribbons,” *ACS Nano*, vol. 5, no. 5, pp. 3779–3787, May 2011.

[3] A. W. Tsen, L. Brown, M. P. Levendorf, F. Ghahari, P. Y. Huang, R. W. Havener, C. S. Ruiz-Vargas, D. A. Muller, P. Kim, and J. Park, “Tailoring Electrical Transport Across Grain Boundaries in Polycrystalline Graphene,” *Science (80-.).*, vol. 336, no. 6085, pp. 1143–1146, Jun. 2012.

[4] C. Stampfer, J. Güttinger, S. Hellmüller, F. Molitor, K. Ensslin, and T. Ihn, "Energy Gaps in Etched Graphene Nanoribbons," *Phys. Rev. Lett.*, vol. 102, no. 5, p. 56403, Feb. 2009.

[5] A. Lherbier, S. M.-M. Dubois, X. Declerck, Y.-M. Niquet, S. Roche, and J.-C. Charlier, "Transport properties of graphene containing structural defects," *Phys. Rev. B*, vol. 86, no. 7, p. 75402, Aug. 2012.

[6] J. Lahiri, Y. Lin, P. Bozkurt, I. I. Oleynik, and M. Batzill, "An extended defect in graphene as a metallic wire," *Nat. Nanotechnol.*, vol. 5, no. 5, pp. 326–329, May 2010.

[7] O. V. Yazyev and S. G. Louie, "Electronic transport in polycrystalline graphene," *Nat. Mater.*, vol. 9, no. 10, pp. 806–809, Oct. 2010.

[8] Z. Liu, Y.-C. Lin, C.-C. Lu, C.-H. Yeh, P.-W. Chiu, S. Iijima, and K. Suenaga, "In situ observation of step-edge in-plane growth of graphene in a STEM," *Nat. Commun.*, vol. 5, Jun. 2014.

[9] B. Song, G. F. Schneider, Q. Xu, G. Pandraud, C. Dekker, and H. Zandbergen, "Atomic-scale electron-beam sculpting of near-defect-free graphene nanostructures," *Nano Lett.*, vol. 11, no. 6, pp. 2247–2250, 2011.

[10] Z. J. Qi, C. Daniels, S. J. Hong, Y. W. Park, V. Meunier, M. Drndic, and A. T. C. Johnson, "Electronic transport of recrystallized freestanding graphene nanoribbons," *ACS Nano*, vol. 9, no. 4, pp. 3510–3520, Apr. 2015.

[11] B. W. Smith and D. E. Luzzi, "Electron irradiation effects in single wall carbon nanotubes," *J. Appl. Phys.*, vol. 90, no. 7, p. 3509, 2001.

[12] A. Zobelli, A. Gloter, C. P. Ewels, G. Seifert, and C. Colliex, "Electron knock-on cross section of carbon and boron nitride nanotubes," *Phys. Rev. B - Condens. Matter Mater. Phys.*, vol. 75, no. 24, pp. 1–9, 2007.

[13] J.-H. Chen, W. G. Cullen, C. Jang, M. S. Fuhrer, and E. D. Williams, "Defect Scattering in Graphene," *Phys. Rev. Lett.*, vol. 102, no. 23, p. 236805, Jun. 2009.

[14] F. Banhart, J. Kotakoski, and A. V. Krasheninnikov, "Structural Defects in Graphene," *ACS Nano*, vol. 5, no. 1, pp. 26–41, Jan. 2011.

[15] J. Kotakoski, A. V. Krasheninnikov, U. Kaiser, and J. C. Meyer, "From Point Defects in Graphene to Two-Dimensional Amorphous Carbon," *Phys. Rev. Lett.*, vol. 106, no. 10, p. 105505, Mar. 2011.

[16] H. Wang, Q. Wang, Y. Cheng, K. Li, Y. Yao, Q. Zhang, C. Dong, P. Wang, U. Schwingenschlögl, W. Yang, and X. X. Zhang, "Doping Monolayer Graphene with Single Atom Substitutions," *Nano Lett.*, vol. 12, no. 1, pp. 141–144, Jan. 2012.

[17] L. Zhao, R. He, K. T. Rim, T. Schiros, K. S. Kim, H. Zhou, C. Gutiérrez, S. P. Chockalingam, C. J. Arguello, L. Pálová, D. Nordlund, M. S. Hybertsen, D. R. Reichman, T. F. Heinz, P. Kim, A. Pinczuk, G. W. Flynn, and A. N. Pasupathy, "Visualizing Individual Nitrogen Dopants in Monolayer Graphene," *Science (80-.).*, vol. 333, no. 6045, pp. 999–1003, Aug. 2011.

[18] O. V. Yazyev and Y. P. Chen, "Polycrystalline graphene and other two-dimensional materials," *Nat. Nanotechnol.*, vol. 9, no. 10, pp. 755–767, Oct. 2014.

[19] A. W. Cummings, D. L. Duong, V. L. Nguyen, D. Van Tuan, J. Kotakoski, J. E. Barrios Vargas, Y. H. Lee, and S. Roche, "Charge transport in polycrystalline graphene: Challenges and opportunities," *Adv. Mater.*, vol. 26, no. 30, pp. 5079–5094, Aug. 2014.

[20] P. Y. Huang, C. S. Ruiz-Vargas, A. M. van der Zande, W. S. Whitney, M. P. Levendorf, J. W. Kevek, S. Garg, J. S. Alden, C. J. Hustedt, Y. Zhu, J. Park, P. L. McEuen, and D. A. Muller, "Grains and grain boundaries in single-layer graphene atomic patchwork quilts," *Nature*, vol. 469, no. 7330, pp. 389–392, Jan. 2011.

[21] X. Jia, J. Campos-Delgado, M. Terrones, V. Meunier, and M. S. Dresselhaus, "Graphene edges: a review of their fabrication and characterization," *Nanoscale*, vol. 3, no. 1, pp. 86–95, Jan. 2011.

[22] J. Baringhaus, M. Ruan, F. Edler, A. Tejeda, M. Sicot, A. Taleb-Ibrahimi, A.-P. Li, Z. Jiang, E. H. Conrad, C. Berger, C. Tegenkamp, and W. A. de Heer, "Exceptional ballistic transport in epitaxial graphene nanoribbons," *Nature*, vol. 506, no. 7488, pp. 349–354, Feb. 2014.

[23] Y.-W. Son, M. L. Cohen, and S. G. Louie, "Energy Gaps in Graphene Nanoribbons," *Phys. Rev. Lett.*, vol. 97, no. 21, p. 216803, Nov. 2006.

[24] L. Ma, J. Wang, and F. Ding, "Recent Progress and Challenges in Graphene Nanoribbon Synthesis," *ChemPhysChem*, vol. 14, no. 1, pp. 47–54, Jan. 2013.

[25] J. Goma and M. Oberlin, "Graphitization of thin carbon films," *Thin Solid Films*, vol. 65, no. 2, pp. 221–232, Jan. 1980.

[26] R. Zan, Q. M. Ramasse, U. Bangert, and K. S. Novoselov, "Graphene Reknits Its Holes," *Nano Lett.*, vol. 12, no. 8, pp. 3936–3940, Aug. 2012.

[27] Q. Xu, M. Y. Wu, G. F. Schneider, L. Houben, S. K. Malladi, C. Dekker, E. Yucelen, R. E. Dunin-Borkowski, and H. W. Zandbergen, "Controllable atomic scale patterning of freestanding monolayer graphene at elevated temperature," *ACS Nano*, vol. 7, no. 2, pp. 1566–1572, Feb. 2013.

[28] J. Kotakoski, D. Santos-Cottin, and A. V. Krasheninnikov, "Stability of Graphene Edges under Electron Beam: Equilibrium Energetics versus Dynamic

Effects," *ACS Nano*, vol. 6, no. 1, pp. 671–676, Jan. 2012.

[29] X. Jia, M. Hofmann, V. Meunier, B. G. Sumpter, J. Campos-Delgado, J. M. Romo-Herrera, H. Son, Y.-P. Hsieh, A. Reina, J. Kong, M. Terrones, and M. S. Dresselhaus, "Controlled Formation of Sharp Zigzag and Armchair Edges in Graphitic Nanoribbons," *Science (80-.).*, vol. 323, no. 5922, pp. 1701–1705, Mar. 2009.

[30] K. K. Saha, M. Drndić, and B. K. Nikolić, "DNA Base-Specific Modulation of Microampere Transverse Edge Currents through a Metallic Graphene Nanoribbon with a Nanopore," *Nano Lett.*, vol. 12, no. 1, pp. 50–55, Jan. 2012.

CHAPTER 4

In-situ electrical measurement on graphene nanoribbons, sculpted with STEM

This chapter contains the main topic of this thesis, which is the sculpting of graphene nanoribbons using the electron beam of a STEM microscope, combined with in-situ heating and electrical biasing. If the reader is not familiar with graphene nanoribbons, it is recommended to read Chapter 1 for a basic overview.

In Chapter 4.1 we explain the procedure for graphene sculpting at high-temperatures, with STEM electron beam. In Chapter 4.2 we describe the experimental setup (the sample fabrication details are in Chapter 6). Finally, in Chapter 4.3 we provide the main results of this research.

4.1 Graphene sculpting at high-temperature using STEM electron probe

The basic mechanism of STEM imaging/sculpting graphene at high temperature the we employ in this work was already demonstrated in [1]. We further optimized this technique for both rough and fine sculpting of graphene.

The first step is to heat up the graphene at ~900-1000 K, using a combination of indirect heating through the MEMS[*] chip (see Chapter 4.2) and direct joule-heating of graphene (as explained later in Chapter 4.3). This high temperature is the key concept of our technique, as it prevents beam induced carbon deposition and it enables self-repair of the graphene lattice. At this point we can image graphene in STEM mode with a 300 keV electron beam and a short dwell time (0.5 μs). The electron energy is above the threshold for knock-off damage of carbon atoms from graphene (86 keV) [2], thus the graphene lattice is damaged during the imaging and promptly self-repaired because of the high temperature. We scan the graphene surface looking for a suitable area to sculpt the nanoribbon. In particular, we search for an area that is free of polymer residues and possibly not containing any grain-boundaries, as they can easily rupture during the sculpting.

During this search, we also characterize the number of layers using two different methods. The first method is the analysis of graphene contrast in the STEM images (see Chapter 2.5.1). The second method is the analysis of the peak intensity of the diffraction spots in Electron Diffraction (ED) patterns (see Chapter 2.5.2). ED is also used to roughly check the crystallographic orientation of the graphene flake.

Once an area has been chosen and the layers counted, we proceed to roughly cut the unwanted parts of graphene, until the width is reduced to 200-300 nm. For the rough cut we use a high current STEM probe with a 4 nm spot size (4.3 nA current, spot size 1). Similarly to conventional electron beam lithography, we define a beam step-size (2 nm) and we adjust the dwell time based on the number of layers to cut (10-500 ms). In case of single layer graphene we can cut as fast as 300 nm/minute. After the initial rough shaping, we change the beam spot size to obtain a finer probe (300 pA current, spot-size 6) and continue to sculpt the graphene in smaller steps. From this point onwards, we carefully sculpt the graphene along one of the main crystallographic axis (zig-zag or armchair). The sculpting angle can be first deduced from the ED pattern, which, however, does not provide the required accuracy. To solve the problem, we acquire an HRTEM image of the local area to sculpt, and deduce the crystal orientation from the 2D FFT of that image. Then we sculpt the graphene and acquire a new HRTEM image as a feedback to adjust the cutting angle. Figure 4.1 gives an example of the STEM sculpting technique. The sculpting process is controlled by a custom-made script for TIA software (compatible with FEI microscopes). The user initially acquires an image

---

[*] Micro Electro-Mechanical Systems

of the sample, then draws a line with the TIA tools, in the position where the cutting should be. Starting the script, the user is asked to input step size, dwell time and number of loops (how many time the beam has to repeat the same path). The script moves the beam along the desired path and stops at the end. Another image can be acquired to check the result.

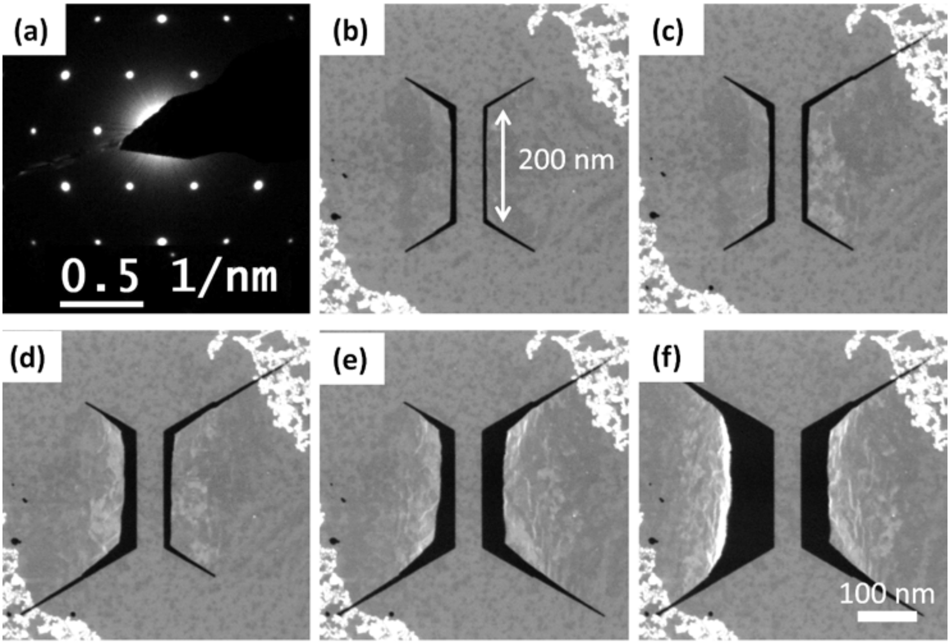

Figure 4.1 (a) Diffraction patter of bilayer graphene, to check the crystallographic orientation. (b)-(f) STEM HAADF images of the sculpting of a 200 nm long, 50 nm wide graphene ribbon. In dark-field images, black areas represent empty space.

4.2 Experimental setup and sample preparation

In order to perform the high-temperature STEM sculpting, in combination with electrical measurements, we have built a custom designed setup, which is illustrated in Figure 4.2, Figure 4.3 and Figure 4.4.

4.2.1 Electrical setup

Starting from Figure 4.2(a), we see the TEM microscope (an FEI Titan 80-300) with the TEM holder inserted from the side entry. A copper-shielded cable links the TEM holder with the Matrix box, visible in Figure 4.2(b). From the Matrix box we route the various electrical signals to the proper destination, such as the current amplifier, the voltage meter, the voltage source, oscilloscope, etc. An Analog Digital Converter (ADC) and a Digital Analog Converter (DAC) provide the connection to the PC, used both to generate and read-out the signals. A more detailed description of the electrical setup, including electrical noise analysis, is reported in Chapter 6.13.

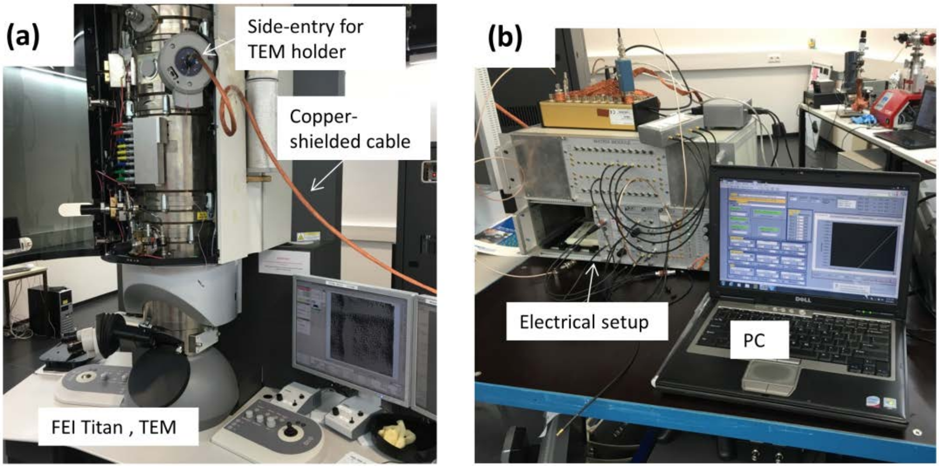

Figure 4.2 Experimental setup: (a) FEI Titan TEM, with the copper-shielded cable connected to the TEM holder (b) Electrical setup, including the Matrix box, the ADC and DAC converters, the heating control box, the PC with software.

4.2.2 In-situ TEM holder and general design of MEMS chips

Moving now to Figure 4.3(a), we see the custom-designed TEM holder, equipped with six electrical connections. Inside the holder there are six wires which connect the tip, where the specimen is located, to the opposite end, which remains accessible to the experimenter when the holder is inserted in the TEM. A standard Fischer ® connector is used to ensure a quick plugging to the electrical setup, via the copper-shielded cable.

An enlargement of the TEM holder tip is shown in Figure 4.3(b): there are six spring-loaded needles, which provide the electrical connection to the contact pads on the MEMS chip, visible in Figure 4.3(d). The MEMS chip is a rectangular Si chip, 0.5 mm thick and 3.4x10 mm in size, which contains six Pt tracks used to carry electrical currents. All these lines converge to the center of the chip, where we find a 0.6 mm wide, 400 nm thick SiN window, shown in Figure 4.3(c). Four of the Pt tracks (200 nm thick) supply current to the Pt heating coil, which is sandwiched between two SiN layers, each 200 nm thick (together they form the 400 nm thick membrane). The coil has a square shape, and it can heat the whole membrane from room temperature up to 900 K through simple Joule heating. The low thermal conductivity of SiN (4-5 W/m/K in thin films) guarantees small power dissipation to the Silicon frame (typically 15-18 mW at 900 K). The remaining two Pt tracks (70 nm thick) are deposited on top of the whole structure, and function as electrodes to measure the electrical properties of graphene. Pointing the attention to Figure 4.3(c), we notice that the Pt electrodes cross the path of the Pt heating coil: we underline that these metal layers are separated by 200 nm thick insulating SiN, and there is no leaking current between them, up to 30 Volt potential difference (see Chapter 6.3.3 for considerations on SiN electrical conductivity and dielectric strength).

Concerning the practical realization of these MEMS devices, their design and manufacturing is entirely done in-house, using the facilities provided by the Kavli Nanolab and TU Delft. A detailed description of their fabrication is given in Chapter 6.1. The MEMS chips are also temperature-calibrated, following the procedure described in Chapter 6.2. Temperature distribution, stress and bulging of the SiN membrane have been optimized using Finite Element Method (FEM) simulation software, Comsol Multiphysics ®, as illustrated in Chapter 6.4. A similar configuration is also available with a ten-pin TEM holder, whose design is visible in Chapter 6.12. The ten-pin holder has six contacts for graphene measurements and four contacts for the heating coil. The greater amount of connections allows also performing 4-probe electrical measurements on graphene. Both the six-pin and the ten-pin holder have been used in our experiments. For each sample we will mention which holder has been used.

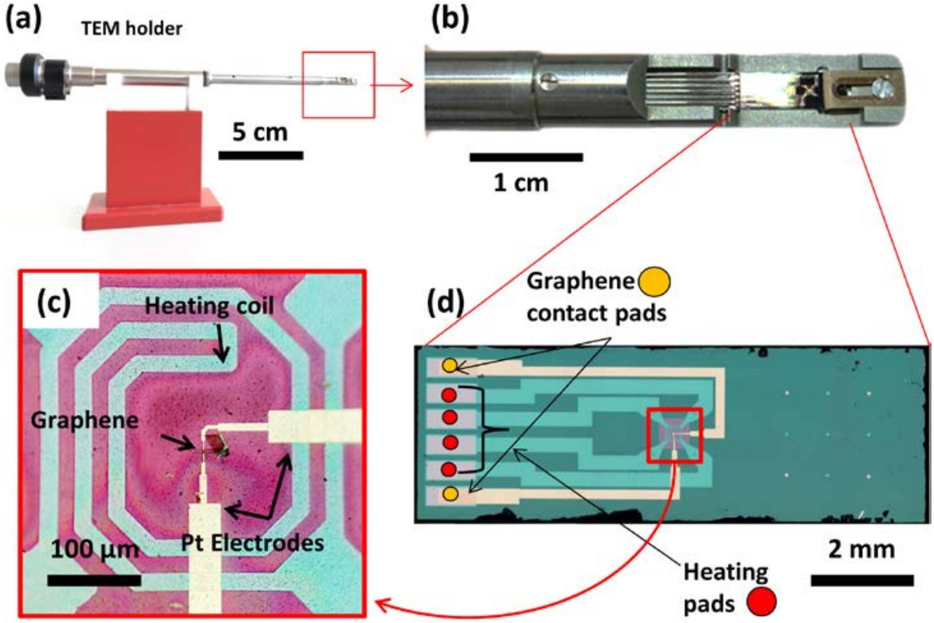

Figure 4.3 (a) In-situ TEM holder for electrical measurements. (b) Zoom of the TEM holder tip, with six electrical contacts. (c) Optical image of the Silicon Nitride window, with the heating coil and the electrical contacts for graphene. The heating coil and the electrodes cross each other paths, but they are separated by a 200 nm thick insulating SiN layer. (d) Optical microscopy image of the MEMS silicon device, to insert in the TEM holder.

4.2.3 Electrodes fabrication and design

In the previous section we explained the general design of the MEMS chip. Here we describe in more detail the fabrication and the configuration of the platinum electrodes used to measure graphene electrical properties.

Starting from a MEMS heating chip with the Pt heating coil, we deposit Ti/Pt electrodes, 5/70 nm thick, using standard electron-beam patterning and lift-off technique. Then we open a through hole in the SiN membrane, between the platinum electrodes, in the position where graphene will be placed. This is essential for TEM observation, as graphene can be imaged and sculpted only if it is completely free-standing (sometimes we also say “suspended” graphene).

Regarding the design for the electrodes and SiN holes, several solutions were tested in order to reach the final configuration that we report here. It is therefore useful to discuss this particular electrode configuration, looking at the motivations that lead to it.

Figure 4.4 (a) and (b) show low- and high-magnification optical images of the Pt electrodes (yellow), the SiN membrane (pink), and the holes in SiN (black). The two electrodes are 180° apart, and terminate with a semi-circular part. Between the electrodes there is a circular hole in the SiN, 2 µm in diameter, which is also visible in the STEM images in Figure 4.4 (c) and (d). The graphene nanoribbon is going to be sculpted on the graphene which is on top of this circle. Because of the SiN thermal expansion during heating and cooling of the membrane, the hole cannot be bigger than 2 µm, otherwise graphene would suffer from excessive strain, and eventually break. The hole also needs to be circular, to distribute the strain as uniformly as possible. Details on SiN thermal expansion and the related strain on graphene are described in Chapters 6.3.2, 6.4.3 and 6.5.

Going back to Figure 4.4 (b) and (c), we see several other rectangular openings (0.5x2 µm in size) in the SiN membrane, parallel and orthogonal to the Pt electrodes. These openings have two different functions: the first one is to provide an area for (S)TEM beam optimization, such as adjusting the *Cs* image corrector or the condenser stigmation, without exposing the central part; the second function is to minimize the current leakage between the two Pt electrodes. In fact, there are three parallel paths for an electronic current between the electrodes: there is graphene, then there is supporting SiN membrane, and finally graphitized carbon. We are actually interested only in the graphene resistance, while the other two components are the “parasitic” parts.

The SiN electrical conductivity is both temperature and electric field dependent: it can be safely neglected at room temperature up to ~2 MV/cm (20 Volts across a 1 µm gap), which lowers to 1 MV/cm when heated at 900 K. A more detailed analysis on SiN electrical conductivity is given in Chapter 6.3.3.

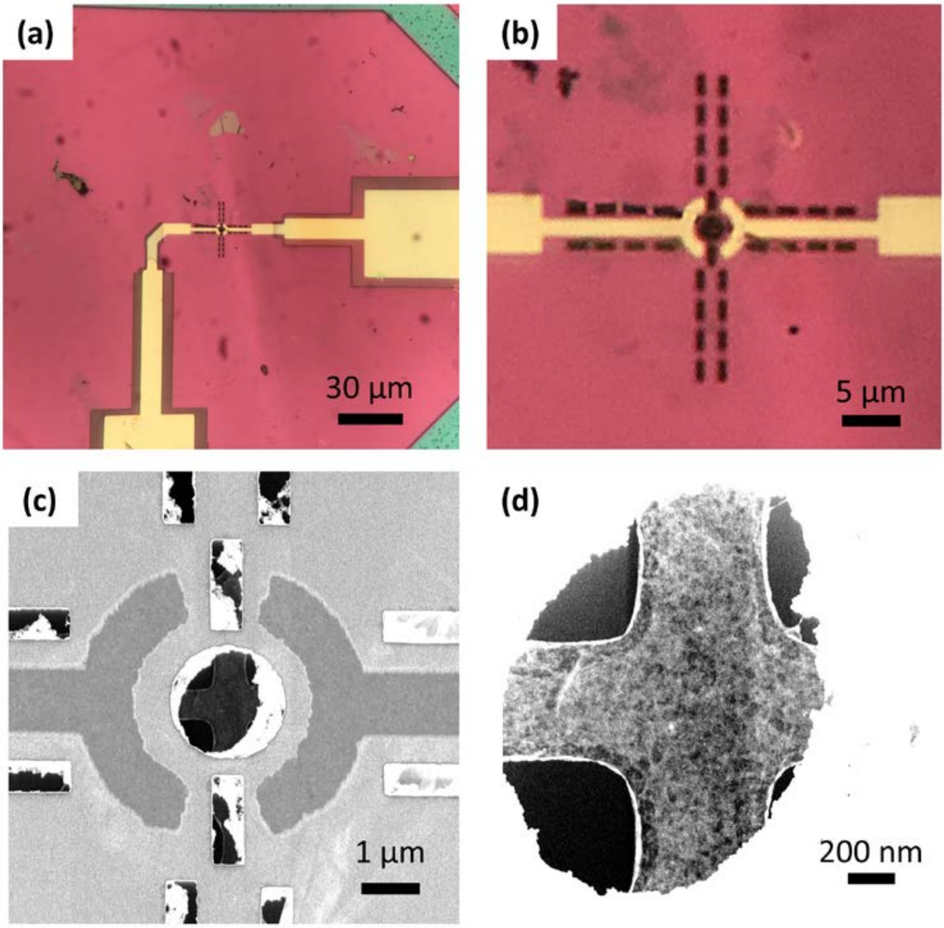

Figure 4.4 Details of Pt electrodes, SiN holes and graphene EBPG pre-patterning. (a),(b) Optical images of the Pt electrodes at different magnification. (c),(d) STEM images of the central SiN hole, with the etched graphene cross, at different magnification. Some residues from PMMA processing are visible on the surface.

Graphitized carbon originates from the organic residues of sample processing (PMMA, solvents), dispersed on the SiN surface, which undergo a graphitization process when heated above ~700-900 K. Contrary to amorphous carbon, graphitized carbon is a good electrical conductor, and it may considerably influence the electrical measurements on the graphene nanoribbons. For this reason, we should not heat the SiN membrane above 600 K during our experiments*. The remaining heat to achieve 900 K, necessary for

---

* Some of the samples that are presented in this Chapter were actually heated at over 900 K with the Pt heating coil, because we were not aware of the carbon graphitization issue yet.

defect-free sculpting, is provided by additional direct Joule heating of the graphene itself. Further details on carbon graphitization and its temperature dependence are given in Chapter 6.6.

Ideally, a single, long cut in SiN between the two electrodes would eliminate all the parasitic contribution of SiN and graphitized carbon, but it would result in an extremely high strain applied on graphene during heating and cooling of the SiN membrane. In practice, the design of the electrodes and the various SiN openings is a compromise between these two adverse effects.

4.2.4 Graphene transfer and pre-patterning

After electrode and SiN holes fabrication, we can proceed with graphene transfer and pre-patterning.

We exfoliate graphene from HOPG graphite with standard scotch tape method, and we transfer it on top of the electrodes, in correspondence of the SiN hole, with wedging transfer technique (see Chapter 6.7). The mechanical and electrical contact between graphene and Pt electrodes is improved with vacuum annealing at temperatures above 420-470 K, achieved with the integrated heating coil of the MEMS chip. The decrease of graphene contact resistance (originating from the graphene-metal interface) during the annealing can be monitored in real-time with in-situ electrical measurements, and it is described in detail in Chapter 6.8. The resistance measured between the two electrodes after the annealing step is typically 1-3 kΩ; from 4-probe measurements performed on the 10-pin holder we observed that only 10% of this value is due to graphene flake resistance, the remaining 90% is the graphene-metal contact resistance. The detailed results of 4-probe measurements of graphene-metal contact resistance are given in Chapter 6.9.

After the graphene-metal adhesion has improved, we need to pre-pattern graphene. Exfoliated graphene flakes are, in fact, tens of µm wide, covering an area which is much larger than the 2 µm circular hole between the electrodes. Since we can use the STEM sculpting only on suspended graphene, we need to remove all the un-suspended parts by other means. We pattern graphene into a 0.5-1 µm wide cross, exactly centered on the 2 µm circular hole between the electrodes, using an EBPG[*] patterned PMMA mask and oxygen plasma. The result of this etching process is visible in Figure 4.4(d).

Now we are finally ready to start the STEM sculpting and perform the in-situ electrical measurements.

---

[*] Electron Beam Pattern Generator

4.3 In-situ electrical measurements on graphene nanoribbons (in TEM)

This section contains the main results of this thesis. We present the results from three devices with graphene nanoribbons, as example of in-situ electrical measurements.

The first device is a monolayer graphene ribbon, while the second and third devices are multilayer. We evaluate their electrical conductivity as a function of ribbon width, temperature and number of layers. In the third device, we show local thinning (from three to two layers) of a graphene nanoribbon due to thermomigration of carbon atoms. On the same device, we also observe the formation of a large charge transport gap (700 meV) due to localized states at the edges of a 1.5 nm wide nanoribbon. We conclude with a general survey on all the fabricated samples (13 in total).

4.3.1 Device 1: monolayer graphene, 50 nm wide ribbon

The first device we show is useful to illustrate the methodology of the in-situ measurements. In this case we use the 10-pin TEM holder, so that 4-probe measurements are also available. This sample was fabricated when we were not aware of the carbon graphitization yet, therefore it was heated at 873 K with the MEMS heater only. The parasitic resistance due to graphitized carbon on SiN surface, in parallel with the graphene resistance, has been measured after all graphene was cut-off. It is comprised between 278 kΩ at 873 K and 3.6 MΩ at 300 K, and it has been subtracted from the total resistance to obtain the “clean” graphene resistance. We also claim that this is a monolayer graphene sample from the diffraction pattern, shown in the inset of Figure 4.5 (ribbon #4); at the time when this sample was fabricated, we had not calibrated the STEM thickness-contrast relationship yet.

The top four images in Figure 4.5 illustrate the progressive sculpting of the graphene flake. Notice that there are some very bright spots in the center of the frame: these are polymeric residues from the graphene transfer and pre-patterning; some metallic nanoparticles are also mixed with the polymer (see Chapter 6.11 for an EDX elemental analysis of those impurities).

The red dots and black squares in the bottom graph of Figure 4.5 are the resistance values corresponding to images #1 to #4, measured *in-situ* at T=300 K and at T=873 K, respectively, plotted as a function of the ribbon width. The resistance is extracted from the slope of the I-V curves, which are perfectly linear at small bias (10-20 mV). The Resistance vs Width data points in Figure 4.5 have been fitted with the equation:

$$R = R_c + \rho \frac{L}{W} \tag{4.1}$$

where R_c is the contact resistance, ρ is the resistivity, L is the length (fixed) and W the width of the nanoribbon.

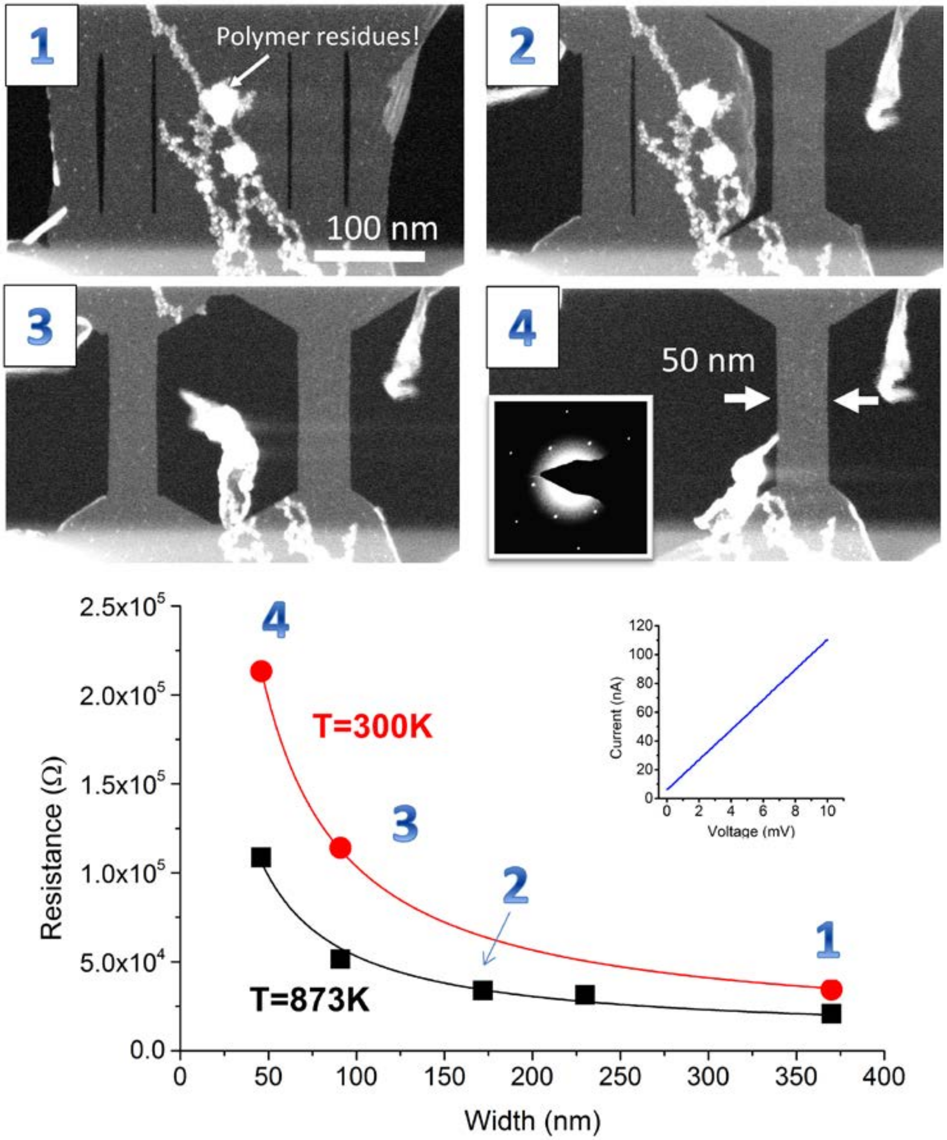

Figure 4.5 In-situ electrical measurements for Device 1, measured at T=873 K and T=300 K. On top, HAADF-STEM images of the progressive sculpting steps, ordered by increasing numbers. The ribbons have been sculpted with a 7 degree misorientation respect to the zigzag direction. On bottom, the corresponding device resistance, measured in real time during the sculpting. The red and black curves are 1/Width fits of the data points. The inset on the right shows the linearity of the I-V curves for this sample, valid in this range of width (50-350 nm) and temperature (300-873 K).

For this particular sample we fix L=250 nm and we extract from the fit at T=873 K, the values R_c =8±3 kΩ and ρ =18±2 kΩ. The same fit on the data points acquired at T=300 K give R_c =9±3 kΩ and ρ=37±4 kΩ. Translating the resistivity values in quantum conductance units, we find that for T=873K and T=300 K, the conductance is G_{873K}=1.4±0.1 e^2/h and G_{300K}=0.69±0.08 e^2/h, respectively. First we will make the analysis of the contact resistance R_c, then the resistivity ρ.

The contact resistance includes two components: one part originates from the graphene-metal interface (due to the different work functions), while the other part comes from the wider part of graphene, which connects the ribbon to the metal electrodes. The graphene-metal interface resistance has been measured with 4-probe sensing: for this sample it is 2.9±0.1 kΩ, with small variation over the whole temperature range (see Chapter 6.8 and 6.9 for a more detailed analysis). This value is compatible with those reported in literature for graphene-Pt interface. The remaining part of the contact resistance, approximately 5 - 6 kΩ, comes from the wide part of suspended graphene before and after the ribbon itself. Its value drops with temperature, similarly to the ribbon resistivity.

Concerning the resistivity of the ribbon, we should know the Fermi level of suspended graphene to be able to interpret the data. This issue is not trivial in our devices, because we do not have an electrostatic gate to shift the Fermi level at all. We assume that the Fermi level is close to the charge neutrality point for the following reasons: first, graphene is suspended, thus there are no induced charges from the substrate; second, graphene has been annealed at 873 K in vacuum, thus removing all water moisture, gas molecules, and other doping contaminants; third, all measurements are performed in high-vacuum, hence no doping from gas adsorbates; fourth and most relevant, we performed ex-situ liquid gating on one test device, and we observed that the minimum conductance is exactly equal to the conductance measured inside TEM, after annealing. This implies that the conductance values obtained with in-situ electrical measurements always correspond to the minimum conductance value. The details of the liquid-gating experiment are in Chapter 6.10.

The value of minimum conductivity in graphene has been subject to intense debate in the scientific community. The theoretical minimum conductivity in a ballistic graphene channel at T=0 K, calculated with the Landauer formula, is $4e^2/\pi h$ L/W ($1.27\ e^2/\pi$ L/W) for monolayer graphene [3] and $2\ e^2/h$ L/W for bilayer graphene [4]. Therefore, the minimum conductivity should scale with the graphene flake aspect ratio Length/Width, increasing for narrower samples, completely opposite to what we observe in our experiment.

However, our experimental conditions are far away from the ideal ballistic case, as we typically measure above room temperature, plus there is the scattering from the edges of the ribbon, which is mostly inelastic due their roughness. Moreover, even in case of perfect edges, an intrinsic band-gap in the order of the thermal energy k_BT=26 meV should appear for widths of ~30-40 nm [5], [6].

The effect of temperature is twofold: on one hand, it increase the conductance because of thermal generated carriers; on the other hand, it decreases the conductance because of increasing electron-phonon scattering. In our case the thermal generation of carrier dominates over the electron-phonon scattering because our devices are close to the charge neutrality point. The effect is clearly visible in Figure 4.6, as we notice a linear increase of the conductance as a function of temperature (a more detailed explanation is given in the next section 4.3.2).

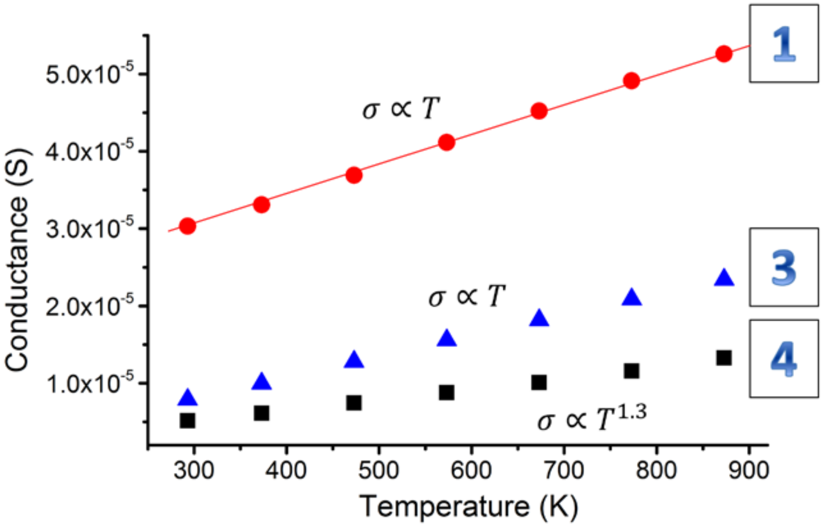

Figure 4.6 Temperature dependence of the conductance for the ribbon shown in Figure 4.5 (Device 1). The numbers on the right correspond to the sculpting steps. Conductance increases linearly with temperature.

The effect of inelastic scattering on the edges will reduce the conductance, regardless of the temperature at which we measure. In particular, it has been shown that the minimum conductivity of graphene ribbons with short length (L<500 nm) and small aspect ratio (W/L< 0.5) is strongly affected by edge roughness, and it can well decrease below the $4e^2/\pi h$ quantum limit [7], [8].

In literature we find recent in-situ TEM studies performed on suspended graphene ribbons [9], [10], to which we can compare our results. Qi et al. [9] reports resistivities of 36 kΩ·nm and 207 kΩ·nm, for a multilayer (2-4 layers) and monolayer, 5 nm long ribbon, respectively. This corresponds to a conductivity of 3.6 e^2/h and 0.62 e^2/h for the multilayer and monolayer sample, similarly to what we found. Instead, Wang *et al.* [10]

reports a resistivity of 3.77×10^3 kΩ·nm for a monolayer, 20 nm long ribbon, which corresponds to a conductivity of 0.14 e^2/h, quite smaller than what we found. Perhaps the discrepancy can be attributed to the irregular shape of their ribbon, which does not maintain a constant length during the process.

4.3.2 Device 2: bilayer graphene, 50 nm wide

Our integrated heater allows us to measure the conductivity of the graphene ribbons in a wide temperature range, from room temperature up to T=900 K. However, many features associated with mesoscopic (electronic) transport appear only at low temperatures. Therefore, we took one of our nanoribbon devices and we performed ex-situ measurements, in a liquid helium refrigerator. The combination of the refrigerator with the integrated Pt heating coil broadens the temperature range enormously, from T=4.2 K to T=900 K.

The data we are reporting here corresponds to a bilayer graphene ribbon (of which we do not show the images). We claim that this is a bilayer device from the diffraction pattern and the optical image of the flake, recorded on SiO_2 substrate before the wedging transfer. Also in this case the STEM thickness-contrast relationship was not fully established yet. The parasitic resistance due to graphitized carbon is not available for this sample, thus it cannot be subtracted.

We measured the resistivity with the same method used in Chapter 4.3.1. We find that at T=300 K, R_c =13±1 kΩ and ρ = 18±2 kΩ, while at T= 873 K the resistance drops to R_c =12±1 kΩ and ρ =8.6±0.5 kΩ. Translated into quantum conductance values we have G_{300K}=1.5±0.2 e^2/h and G_{873K}=3.0±0.2 e^2/h. We can see that the conductivity is approximately twice as large as the sample shown in Chapter 4.3.1, compatible with the fact that here we have two graphene layers instead of one.

The sample was inserted in the liquid helium refrigerator after the last sculpting step, which is a ribbon with L=200 nm and W=50 nm. The refrigerator has a temperature sensor, so that we could record the temperature during the cooling to T=4.2 K, but there is no thermostat to set the temperature at our will. The heating above T=300 K was achieved inside the refrigerator itself, using the in-situ heating coil of our device. We limited the maximum temperature to T=700 K instead of T=900 K, as it was enough to show the temperature dependence.

Looking at the inset of Figure 4.7 we see that at T=4.2 K, the I-V curve is non-linear, from which we deduce that there is a small transport gap E_{gap}~10 meV. It is also useful to display the same data in the Arrhenius plot, shown in Figure 4.8. For T < 100 K, the transport is ruled by variable range hopping (VRH) conduction, but limited amount of data is not enough to distinguish between a $T^{-1/2}$ or $T^{-1/3}$ dependence, or to extract a meaningful hopping distance.

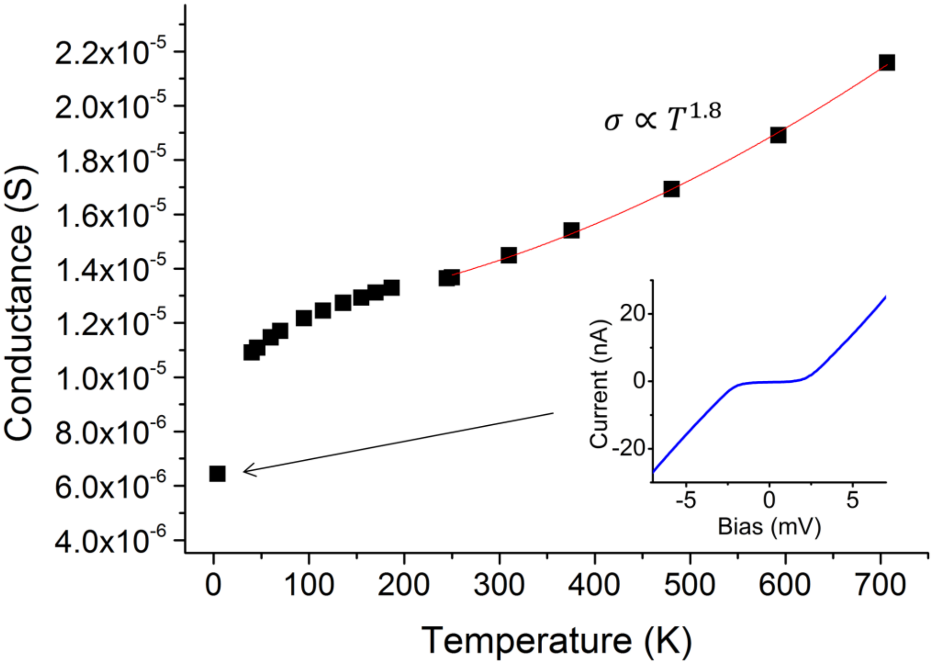

Figure 4.7 Conductance vs Temperature plot for Device 2, L=200 nm, W=50 nm. Above T=250 K the conductance increases almost quadratically with temperature. The inset shows the I-V curve at T=4.2 K, from which a small transport gap E_{gap}=10 meV can be extracted.

Thermal activated behavior is present for 100 K < T < 250 K, with activation energy E_a=22 meV. Above room temperature, we observe an almost quadratic increase of the conductance, $\sigma \sim T^{1.8}$. In this range, thermal activated transport cannot explain by itself the observed data. We need to add a new component, namely thermal generated carriers. As we already mentioned in Chapter 4.3.1, our graphene devices are very close to the charge neutrality point. At low temperatures, the carrier density is mainly governed by charged impurities, which set the minimum density at $n_{imp}=10^8 \div 10^9$ cm^{-2} [11][*]. When the temperature is increased, thermal generated carriers, electron-like plus hole-like quasiparticles, give their contribution according to the equation [12][†]:

$$n_{th}(bilayer) = 2\frac{t\ln 2}{\pi(\hbar v_F)^2}k_B T \qquad (4.2)$$

---

[*] These values are valid for clean suspended graphene. For graphene on SiO_2 substrate, it is at least two orders of magnitude higher, because of the charged impurities on its surface.

[†] The equation is valid for bilayer graphene.

where v_F ~10^8 cm/s is the Fermi velocity in graphene and t~0.4 eV is the nearest neighbor interlayer hopping energy in bilayer graphene. At T=300 K, we have $n_{th}=1\times10^{12}$ cm^{-2}, which is at least three orders of magnitude higher than n_{imp}. At T=700 K we have $n_{th}=2.4\times10^{12}$ cm^{-2}, and an even higher number of thermal generated carriers contribute to the conduction. In bulk bilayer graphene, the conductance is proportional to the carrier density according to the equation [13]:

$$\sigma(n) \propto n^{\alpha} \quad \text{with} \quad 1 \leq \alpha \leq 2 \tag{4.3}$$

where the coefficient α depends on the dominant scattering mechanism (Coulomb, short-range, phonon). From the fitting of our data for T>300 K, we obtain a $T^{1.8\pm0.2}$ dependence of the conductance, which confirms the proposed model with coefficient α=1.8.

This is actually the only sample where we found a strong superlinear dependence of the conductance at high temperature. All the other samples (either monolayer, bilayer or multilayer) always display a linear or sublinear dependence (coefficient $\alpha \leq 1$) . The only plausible explanation that we have at the moment is related to the fact that this particular measurement was performed inside the liquid helium refrigerator, which might have changed the actual temperature on graphene during the in-situ heating.

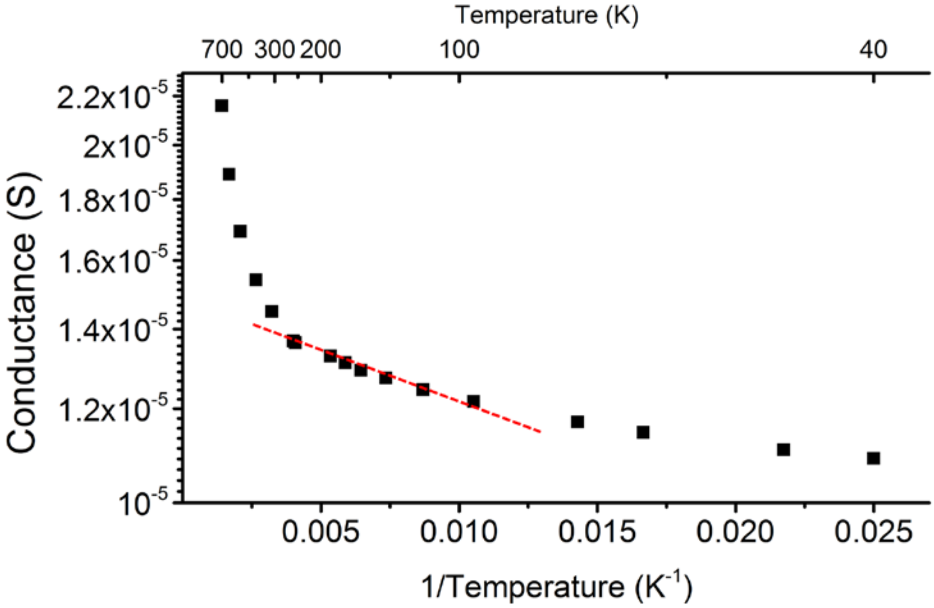

Figure 4.8 Arrhenius plot, using the same data of Figure 4.7 (Device 2). In the range 100 K<T<250 K we observe thermal activated transport (red dashed line). For T<100 K, variable range hopping is the most likely candidate.

4.3.3 Device 3: two-three layer graphene, 100 to 8 nm wide

The third device we present was measured on the 6-pin holder, therefore only two-probe measurements are available. The initial ribbon is three layers thick, as calculated from the STEM contrast analysis (see Chapter 2.5.1). In order to prevent the parasitic conductive carbon issue which was present in Device 1 and 2, this sample was heated at a maximum temperature of T=573 K with the embedded Pt heating coil. The heat required to increase the temperature from T=573 K to T=900 K, necessary for graphene sculpting, was provided by direct Joule heating of graphene. The parasitic resistance due to graphitized carbon, measured after the graphene nanoribbon breakdown, is ~1 GΩ at T=573 K and higher than 10 GΩ at T=300 K (beyond the limit of our electrical setup).

Figure 4.9 (a) shows the initial status of the device, immediately after Oxygen plasma etching and PMMA mask removal. The ribbon is approximately 270 nm wide and 1850 nm long. The presence of PMMA residues is clearly visible, in the form of round particles, 20-30 nm in diameter, dispersed on the surface. EDX analysis of the particles (not shown here), confirms the presence of Carbon and Oxygen (Hydrogen cannot be detected). Heating at 573 K does not help removing of modifying them.

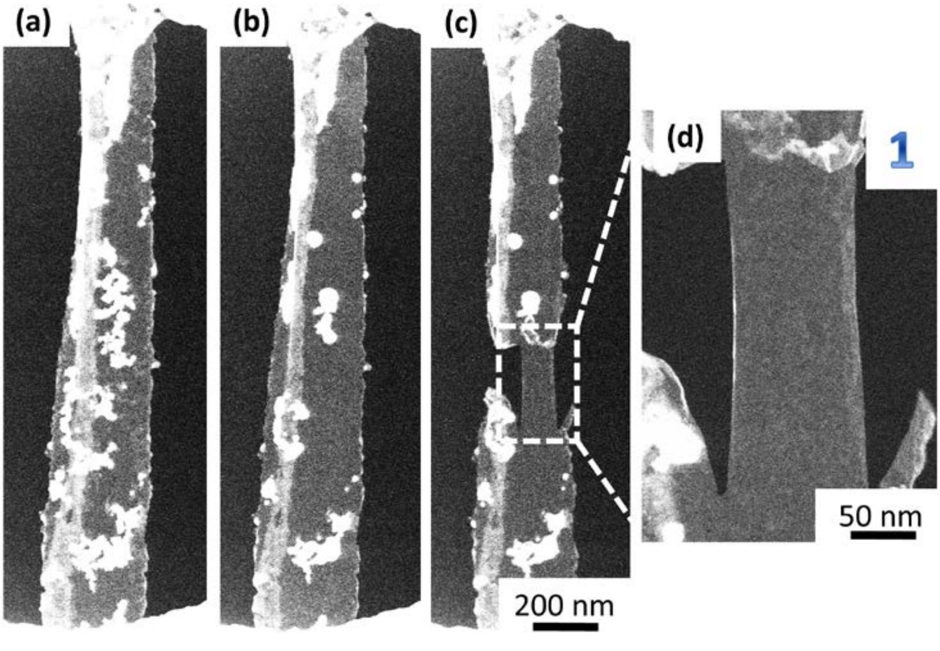

Figure 4.9 STEM images of graphene ribbon Device 3. (a) Ribbon immediately after oxygen plasma etching and PMMA removal in acetone. PMMA residues are visible as bright spots on graphene surface. Edges are very rough. The ribbon is 1850 nm long and 270 nm wide. (b) Annealing at T=1000 K, obtained as combination of direct Joule heating of graphene plus the MEMS platinum heating coil, set at T_0=573 K. PMMA is not removed, but it melts in bigger clusters. (c)-(d) First step of graphene sculpting, to define a 100 nm wide, 250 nm long ribbon.

Applying a 1.4 V direct bias on the ribbon, we achieve a current density of 3.8×10^{7} A/cm^{2}, calculated considering three layer graphene (0.335 nm single layer thickness [14]). The temperature distribution along the ribbon can be calculated using the one-dimensional heat conduction equation [15]:

$$T(x) = T_0 + \frac{IV}{2Wh\lambda}x - \frac{IV}{2LWh\lambda}x^2 \tag{4.4}$$

where T_0 is the temperature at the extremes of the ribbon, h is the height, λ is the thermal conductivity, I and V are the current and voltage, respectively. If we consider a thermal conductivity of 150 W/m/K [16], [17], we can find the maximum temperature reached in the middle of the ribbon is ~1000 K (with T_0=573 K). These considerations are valid if we assume a strong electron-phonon coupling, so that the heat generated by the hot electrons is locally dissipated on the ribbon, rather than on the contacts. This is a valid hypothesis if we consider scattering from optical and flexural phonons [18], [19]. Flexural phonons arise because samples are freestanding, while in-plane optical phonons contribute only above ~0.2 V voltage bias. The result of the Joule heating at T~1000 K is visible in Figure 4.9(b): most of the polymeric residues have agglomerated in bigger clusters, leaving a cleaner zone for sculpting graphene. The first sculpting step is shown in Figure 4.9 (c) and (d), where we have created a 100 nm wide, 250 nm long constriction.

From this point onwards we proceed with gradual sculpting of the ribbon, reducing its width while keeping the length constant. Figure 4.10 shows the subsequent sculpting steps, going from W=45 nm on the leftmost image, to W=8 nm in the rightmost. As we did in Chapter 4.3.1 and 4.3.2, we can use equation 4.1 to extract the resistivity and the contact resistance: at T=300 K, R_c=11±6 kΩ and ρ = 12±2 kΩ, while at T= 573 K the resistance drops to R_c=11±4 kΩ and ρ=9±1 kΩ. Translated into quantum conductance values we have G_{300K}=2.2±0.4 e^2/h and G_{573K}= 3±0.4 e^2/h. These conductivity values are slightly higher than the bilayer ribbon, compatible with the fact that this ribbon is mostly three layers thick (with some bilayer segments, visible in Figure 4.10).

Similarly to what we did in Chapter 4.3.2, we analyze the temperature dependence of the conductance for each sculpting step, in the range between 300 K and 573 K. Figure 4.11 shows that the conductance increases sublinearly with temperature, with an exponent which varies between 0.31 for the largest ribbon (step#1, 100 nm wide), to 0.72 in the narrowest ribbon (step#5, 8 nm wide). The exponent tends to increase as the ribbon is narrowed, a trend which has been consistently observed in all bilayer and multilayer samples we measured (excluding the monolayer sample, which was always linear regardless of the ribbon width).

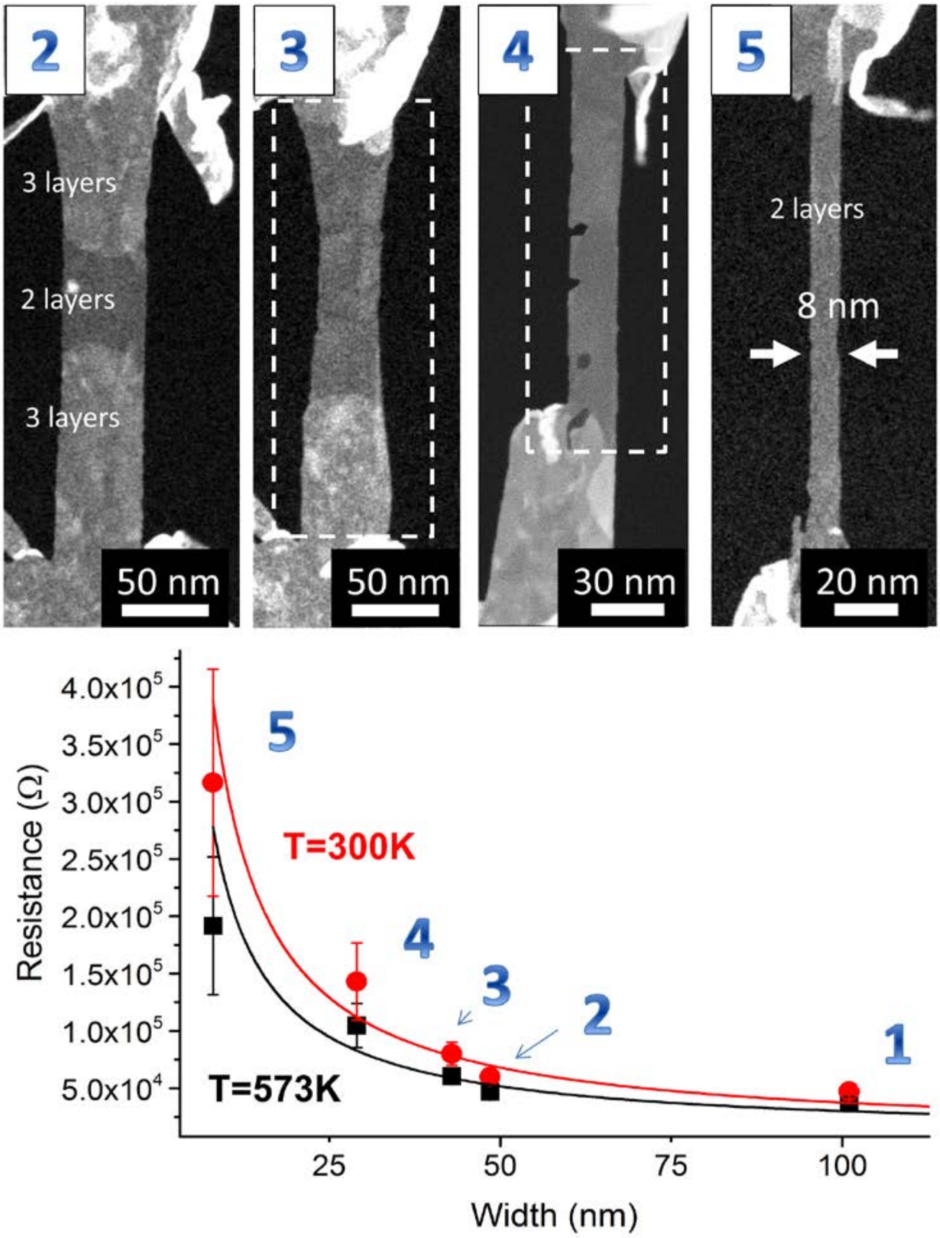

Figure 4.10 Top: STEM images of progressive sculpting steps of the graphene ribbon in Device 3. Bottom: Resistance vs Width graph for the same device, measured at T=300 K and T=573 K. Step number 1 is shown in Figure 4.9 (c) and (d). The error bars on the Resistance axis have been derived from the uncertainty on the width of the ribbon.

The actual interpretation of this trend is not trivial: as we already mentioned in Chapter 4.3.2, multiple scattering mechanisms contribute to the ribbon conductance, and it is not possible to isolate their individual contribution without full control on Fermi level and low-temperature measurements. In a recent publication, *Sarma and Hwang* [20] show that the interplay of Coulomb, short and phonon scattering can indeed produce such sublinear dependency. The fact that the trend becomes more linear in narrow ribbons remains currently unexplained.

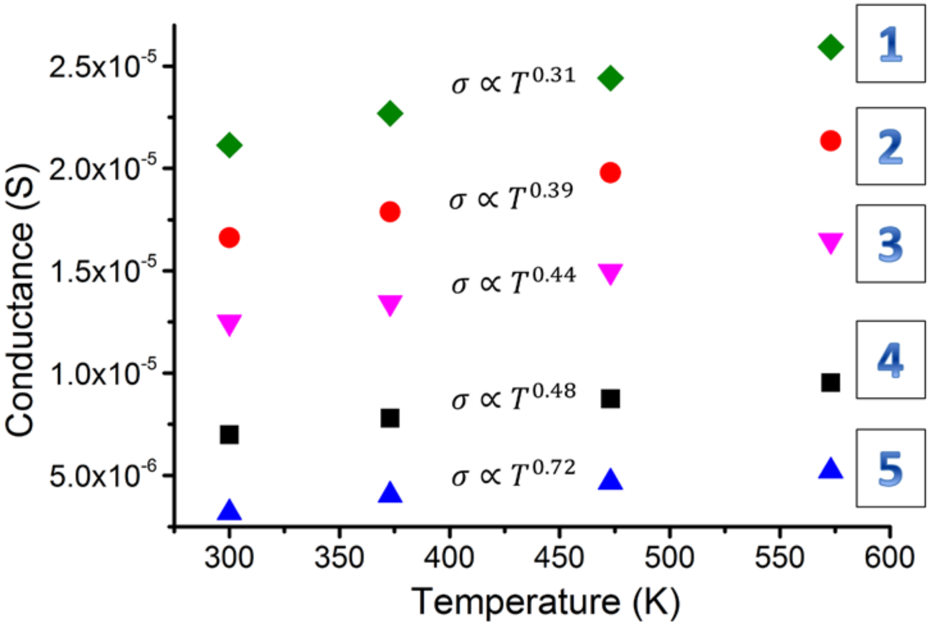

Figure 4.11 Conductance as a function of Temperature for the cutting steps from 1 to 5, as shown in Figure 4.10 (Device 3). The Conductance increases sublinearly as function of Temperature for all widths, but with different exponents.

4.3.4 Device 3: thermomigration at high bias

As we already mentioned in the previous section, Joule heating the ribbon can produce temperatures exceeding 1000 K. If we look at the STEM images in Figure 4.10, we notice that the middle part of the ribbon #2 and #3 is only two layers thick, while the most outer parts are three layers thick. This local thinning is the result of a thermomigration process of carbon atoms, induced by the high temperature gradient created across the length of the nanoribbon during high-bias Joule heating (approx. 2.9 Volts and 3.5×10^{8} A/cm^{2} current density).

We claim that this is a thermomigration process rather than electromigration, because the thinning always starts from the middle of the ribbon, regardless of the electric current direction*.

The Current-Voltage (I/V) and Conductance-Voltage (S/V) plots of the annealing between step #2 and #3 are shown in Figure 4.12. The I/V plot is superlinear up to 2.3 Volts, and it does not show any saturation behavior. The superlinear trend arises from the Joule heating of the nanoribbon, which increases the number of thermal generated carriers, thus the conductance of the ribbon itself [21]. In fact, we see from the S/V plot that the conductance of the ribbon steadily increases up to 2.3 Volts. However, we also notice that the conductance saturates beyond 2.3 Volts, reaching a plateau at 2.9 Volts. This saturation effect is related to the physical modification of the ribbon, due to the thermomigration effect.

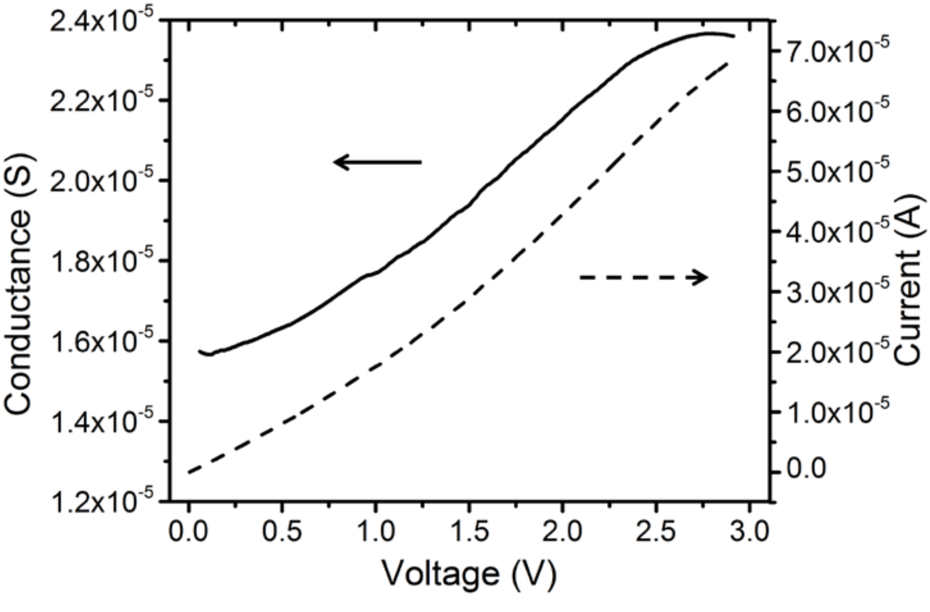

Figure 4.12 Conductance and Current as a function of the Voltage applied across the graphene ribbon before sculpting step #3, as shown in Figure 4.10.

We have used Equation 4.4, in combination with the temperature-conductance data shown in Figure 4.11, to run a Finite Element Method simulation of the temperature distribution along the length of the ribbon #3 of Figure 4.10. The result is shown in Figure 4.13: using an upper and lower limit of 150 and 80 W/m/K for the thermal conductivity [16], [17], and a 2.3 Volt bias, we see that the temperature reaches

---

* The thinning due to electromigration in metallic Pd-Pt nanobridges always starts from the cathode side [29]

T=1900-2300 K in the middle of the ribbon. The temperature gradient in the steepest point is between 3 and 7 K/nm. Other TEM studies have observed graphene melting/sublimating in the 2000-2500 K temperature range [22]–[25], but they do not consider the effect of temperature gradient, which is particularly evident in our case.

Increasing the voltage beyond 2.3 Volts initiates the thermomigration process, which causes the ribbon to become thinner and thus the electrical conductance to saturate (or even drop, at 2.9 Volts). The annealing step has been repeated also between steps #3 and #4, with similar results. However, we notice that in step #4 from Figure 4.10, the left edge has two dents, corresponding to a reconfiguration of the edge shape. We think that this happened because it is energetically more favorable to adjust the edges of the ribbon rather than breaking the bonded bilayer edge to form a single layer graphene edge [26], [24]. This means that the thermomigration thinning process stops when the graphene is bilayer, and it cannot be used to create single layer graphene ribbons.

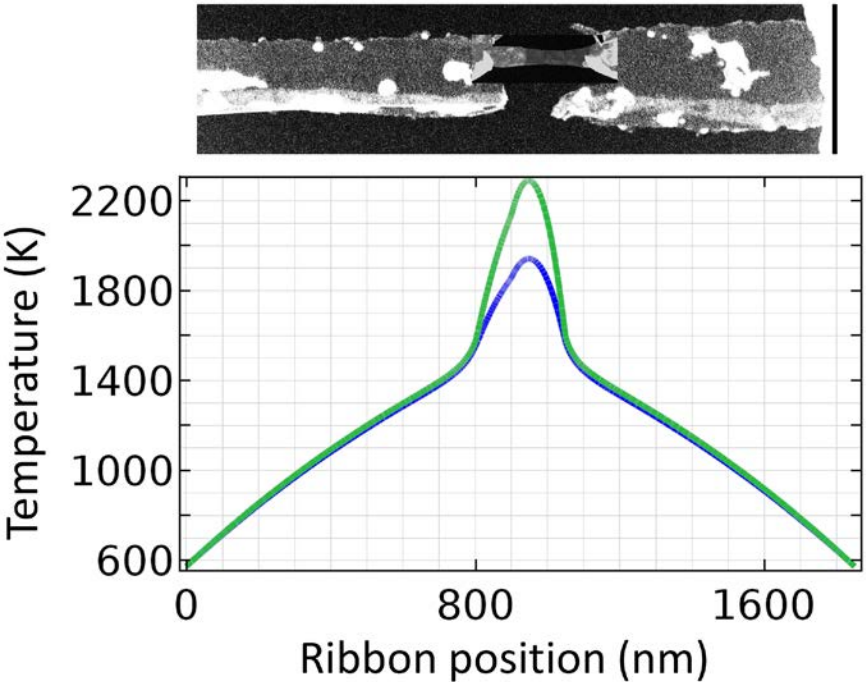

Figure 4.13 Temperature distribution along the ribbon length, calculated with Finite Element Method simulation, for sculpting step #3 in Figure 4.10. The green curve and blue curve correspond to a thermal conductivity of 80 and 150 W/m/K, respectively. The applied bias is 2.3 Volts, and the Pt heating coil is set at T_0=573 K.

4.3.5 Device 3: semiconducting nanoribbon, 1.5 nm wide

Using the same device of the previous two sections (4.3.3 and 4.3.4), we continue the sculpting and Joule heating process. Starting from step #5 in Figure 4.10, we narrow the ribbon from 8 nm down to 2.5 nm, trying to sculpt along the armchair direction.

Figure 4.14 (a), (b) show the low magnification of the ribbon, both in STEM and TEM mode. Despite our effort to follow the armchair direction during sculpting, it remains very difficult to achieve a smooth, single type of edge along the whole 120 nm length of the ribbon. The difficulties arise from sample drift, which should be smaller than 0.5 nm/min: such condition that can be achieved only after several hours of stabilization. As it can be seen from Figures 4.14 (c), (d), some segments rearrange into zigzag configuration, with the help of Joule heating, in order to smooth the rough junctions in the ribbon. This phenomenon is consistent with what has been observed in a recent publication from Qi *et al.*[26].

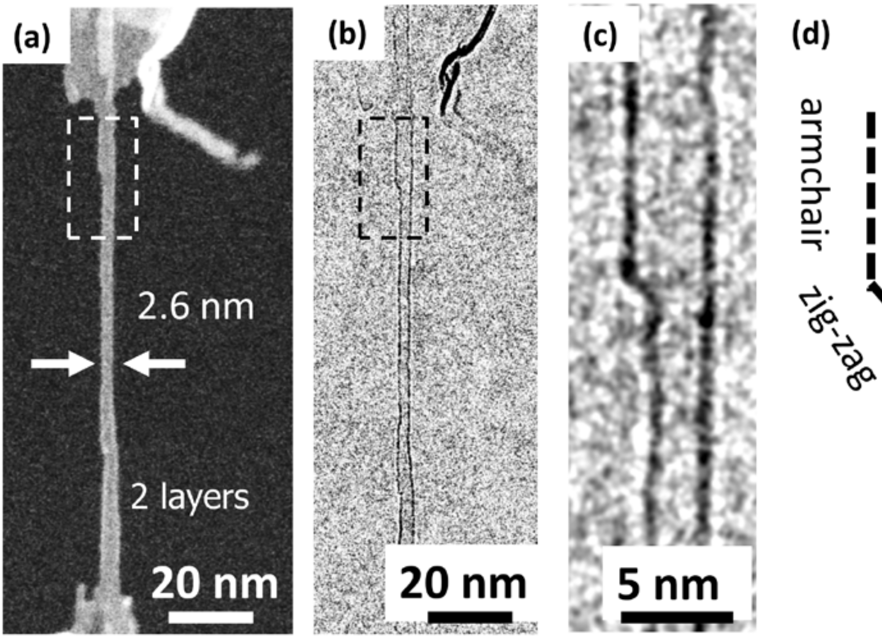

Figure 4.14 (a) STEM image of bilayer graphene nanoribbon, 2.6 nm wide and 120 nm long. (b)-(c) Bright-field TEM images of the same ribbon. (c) is a detail showing different edge orientation along the ribbon, schematically illustrated in (d).

Considering the aforementioned difficulties, we think it is unpractical to continue sculpting the nanoribbon with the electron beam below 2.5 nm. Therefore we continue with Joule annealing only, applying high bias voltages across the ribbon. After a short annealing at 2.9 Volts (less than 5 seconds), the resulting ribbon has shrunk to 1.5 nm width, as shown in Figure 4.15 (a). The corresponding I-V plot, shown in Figure 4.15 (b), is strongly non-linear, and it displays an insulating state approx. in the ±700 mV range.

The most likely interpretation for this insulating state is the formation of a transport gap due to localized states at the edges of the ribbon [10], [27]. The size of the gap, derived directly from the I-V curve, is 700 meV: this large gap also explains the stability of the insulating state up to T= 620 K (thermal energy k_BT = 53 meV).

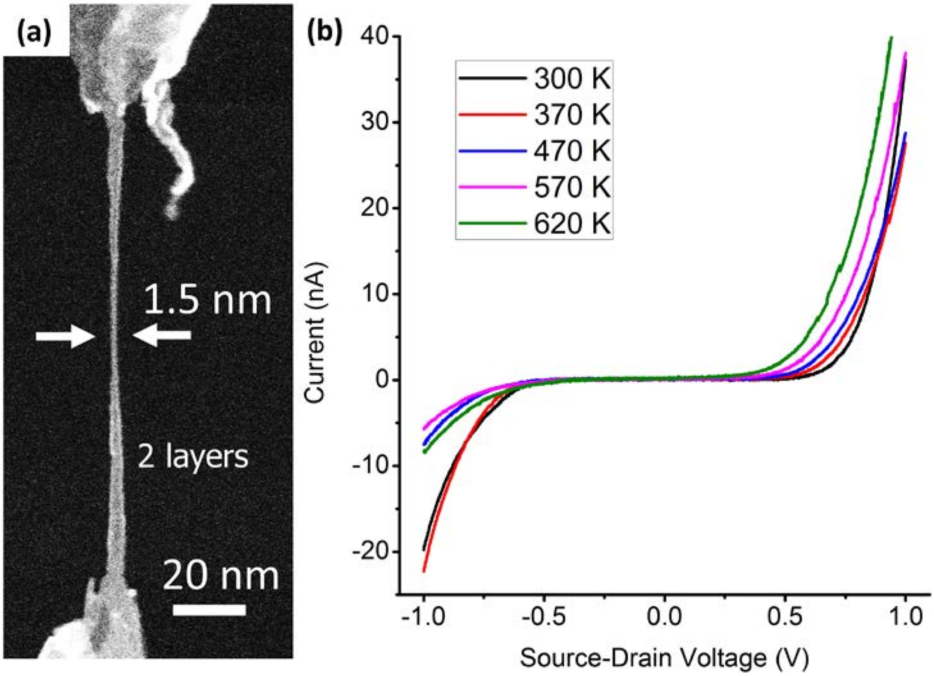

Figure 4.15 (a) STEM image of the bilayer graphene nanoribbon after additional Joule heating at 2.9 Volts. (b) I-V plot of the nanoribbon, recorded at various temperatures, showing strong non-linear behavior, with an insulating state (R >1 GΩ) in the ±700 mV range.

4.3.6 General survey on all the fabricated samples

During the course of this research, more than 40 graphene samples were fabricated. Only 13 of them did not present fabrication issues, and were sculpted and measured in our in-situ experiments. Figure 4.16 summarizes the Resistance vs Width behavior for all these samples. The data has not been filtered at all. It includes samples with any layer number (monolayer, bilayer, multilayer) and any temperature (from T=300 K to T= 873 K).

All this data can be used to validate the model we proposed in Chapter 4.3.1, Equation 4.1 (only the width dependency), fitting them with the equation:

$$R = R_c + \frac{\rho L}{W^{\beta}}. \tag{4.5}$$

We find that R_c=6±12 kΩ, ρL=1.2±0.2×10^6 Ω·nm and β = 0.9±0.1. The proposed model, with β=1, remains within the standard deviation.

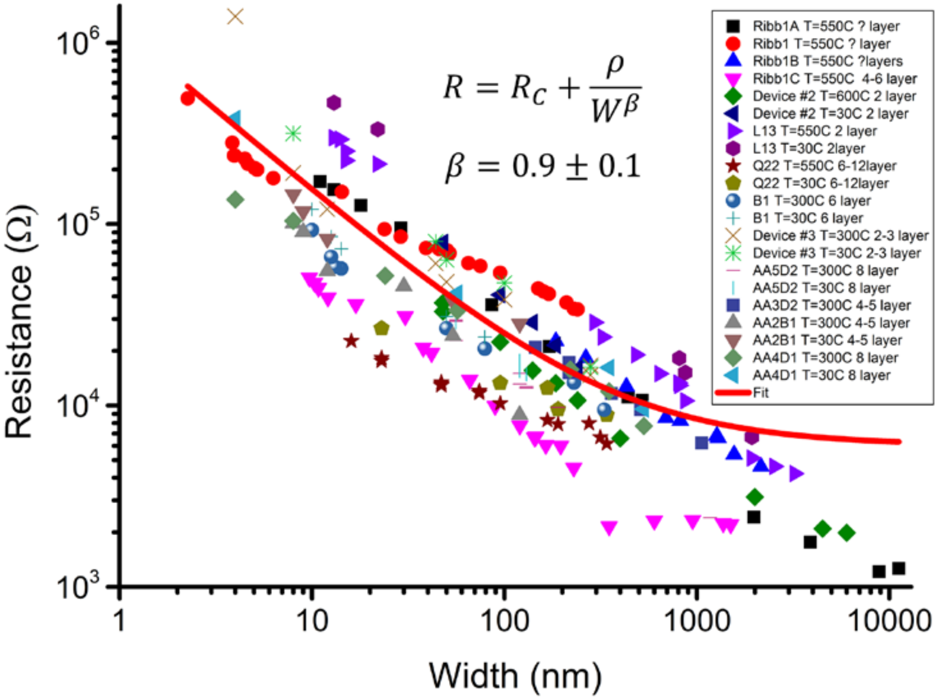

Figure 4.16. Resistance vs Width plot for 13 graphene nanoribbon samples. The red line is a non-linear fit based on the equation written on top of the figure.

4.4 Conclusions

In this chapter we have demonstrated the fabrication of graphene nanoribbons using direct electron beam-sculpting in STEM mode, combined with in-situ heating and electrical biasing. We have seen that the wide nanoribbons (W>5-10 nm) behave similarly to ohmic conductors, whose resistance scales inversely with the ribbon width. Narrower ribbons (W~1.5 nm) exhibit insulating state, with transport gap as large as 700 meV.

Although we cannot control the Fermi level in our ribbons, we show strong evidence that they are mostly near the charge neutrality point during the in-situ measurements in the TEM high-vacuum. This is also compatible with the fact that their electrical conductance always increases as a function of temperature, due to thermal generated carriers. However, the exact temperature-conductance relationship considerably varies from sample to sample, being either sublinear, linear or superlinear. Such variation can be attributed to the different scattering sources (Coulomb, phonon, defects) which contribute to the electrical conduction in the graphene ribbon.

Upon application of a high-voltage bias (2.9 Volts) on the graphene nanoribbon, temperatures exceeding T=2000 K can be reached in its centermost part. The high temperature, in combination with temperature gradient, causes a thermomigration process, during which carbon atoms move from the hottest part of the ribbon (in the middle), to the colder parts (the extremities). This procedure can be used to thin down multilayer graphene nanoribbons, down to bilayer graphene (but not possible with monolayer).

Concerning the dependency of electrical conductivity on the number of graphene layers, we find that is scales linearly between two to five layers (including all the data from the 13 fabricated samples, not shown here). We cannot claim that this linear trend extends to monolayer graphene because we measured only one sample. Moreover, we did not find any dependence of electrical conductance on armchair or zigzag edge in our samples, which could be explained by the residual roughness of the edges we fabricated.

As a general remark about in-situ electrical-heating experiments, we found that in-situ heating above T ~570 K induces (partial) graphitization of amorphous carbon, present on the SiN surface. The graphitized carbon has a non-negligible conductance, and it offers a parallel, parasitic, path for electrical current flow. The experimenter should always be aware of this effect, and try to reduce the amount of undesired carbon on the sample (for example polymer residues from processing, or beam-induced carbon deposition during SEM and TEM imaging).

For future experiments, the inclusion of an electrostatic gating would allow us to change the Fermi level in the nanoribbon, thus exploring an additional degree of freedom. The recent experiment from Rodríguez-Manzo *et al.*[28] shows promising steps in this direction.

References

[1] Q. Xu, M. Y. Wu, G. F. Schneider, L. Houben, S. K. Malladi, C. Dekker, E. Yucelen, R. E. Dunin-Borkowski, and H. W. Zandbergen, “Controllable atomic scale patterning of freestanding monolayer graphene at elevated temperature,” *ACS Nano*, vol. 7, no. 2, pp. 1566–1572, Feb. 2013.

[2] J. C. Meyer, F. Eder, S. Kurasch, V. Skakalova, J. Kotakoski, H. J. Park, S. Roth, A. Chuvilin, S. Eyhusen, G. Benner, A. V. Krasheninnikov, and U. Kaiser, “Accurate measurement of electron beam induced displacement cross sections for single-layer graphene,” *Phys. Rev. Lett.*, vol. 108, no. 19, p. 196102, May 2012.

[3] M. Müller, M. Bräuninger, and B. Trauzettel, “Temperature dependence of the conductivity of ballistic graphene,” *Phys. Rev. Lett.*, vol. 103, no. 19, pp. 2–5, 2009.

[4] M. I. Katsnelson, “Minimal conductivity in bilayer graphene,” *Eur. Phys. J. B*, vol. 52, no. 2, pp. 151–153, Jul. 2006.

[5] M. Y. Han and P. Kim, “Graphene nanoribbon devices at high bias,” *Nano Converg.*, vol. 1, no. 1, p. 1, Dec. 2014.

[6] A. Celis, M. N. Nair, A. Taleb-Ibrahimi, E. H. Conrad, C. Berger, W. A. de Heer, and A. Tejeda, “Graphene nanoribbons: fabrication, properties and devices,” *J. Phys. D. Appl. Phys.*, vol. 49, no. 14, p. 143001, Apr. 2016.

[7] F. Miao, S. Wijeratne, Y. Zhang, U. C. Coskun, W. Bao, and C. N. Lau, “Phase-Coherent Transport in Graphene Quantum Billiards,” *Science (80-.).*, vol. 317, no. 5844, pp. 1530–1533, Sep. 2007.

[8] Y. Sui, T. Low, M. Lundstrom, and J. Appenzeller, “Signatures of Disorder in the Minimum Conductivity of Graphene,” *Nano Lett.*, vol. 11, no. 3, pp. 1319–1322, Mar. 2011.

[9] R. Botello-me, S. J. Hong, E. a. Stach, Y. W. Park, J. C. Charlier, M. Drndic, a. T. C. Johnson, Z. J. Qi, J. a. Rodríguez-Manzo, A. R. Botello-Méndez, S. J. Hong, E. a. Stach, Y. W. Park, J. C. Charlier, M. Drndić, and a. T. C. Johnson, “Correlating Atomic Structure and Transport in Suspended Graphene Nanoribbons,” *Nano Lett.*, vol. 14, no. 8, pp. 4238–4244, 2014.

[10] Q. Wang, R. Kitaura, S. Suzuki, Y. Miyauchi, K. Matsuda, Y. Yamamoto, S. Arai, and H. Shinohara, “Fabrication and In Situ Transmission Electron Microscope Characterization of Free-Standing Graphene Nanoribbon Devices,”

ACS Nano, vol. 10, no. 1, pp. 1475–1480, Jan. 2016.

[11] K. I. Bolotin, K. J. Sikes, J. Hone, H. L. Stormer, and P. Kim, “Temperature-Dependent Transport in Suspended Graphene,” *Phys. Rev. Lett.*, vol. 101, no. 9, p. 96802, Aug. 2008.

[12] W. Zhu, V. Perebeinos, M. Freitag, and P. Avouris, “Carrier scattering, mobilities, and electrostatic potential in monolayer, bilayer, and trilayer graphene,” *Phys. Rev. B - Condens. Matter Mater. Phys.*, vol. 80, no. 23, pp. 1–8, 2009.

[13] S. Das Sarma, E. H. Hwang, and E. Rossi, “Theory of carrier transport in bilayer graphene,” *Phys. Rev. B - Condens. Matter Mater. Phys.*, vol. 81, no. 16, pp. 3–6, 2010.

[14] Y. Huang, J. Wu, and K. C. Hwang, “Thickness of graphene and single-wall carbon nanotubes,” *Phys. Rev. B*, vol. 74, no. 24, p. 245413, Dec. 2006.

[15] X. Zhang, H. Xie, M. Fujii, H. Ago, K. Takahashi, T. Ikuta, H. Abe, and T. Shimizu, “Thermal and electrical conductivity of a suspended platinum nanofilm,” *Appl. Phys. Lett.*, vol. 86, no. 17, pp. 1–3, 2005.

[16] M.-H. Bae, Z. Li, Z. Aksamija, P. N. Martin, F. Xiong, Z.-Y. Ong, I. Knezevic, and E. Pop, “Ballistic to diffusive crossover of heat flow in graphene ribbons,” 2013.

[17] X. Xu, L. F. C. Pereira, Y. Wang, J. Wu, K. Zhang, X. Zhao, S. Bae, C. Tinh Bui, R. Xie, J. T. L. Thong, B. H. Hong, K. P. Loh, D. Donadio, B. Li, and B. Özyilmaz, “Length-dependent thermal conductivity in suspended single-layer graphene,” *Nat. Commun.*, vol. 5, Apr. 2014.

[18] H. Ochoa, E. V. Castro, M. I. Katsnelson, and F. Guinea, “Scattering by flexural phonons in suspended graphene under back gate induced strain,” *Phys. E Low-dimensional Syst. Nanostructures*, vol. 44, no. 6, pp. 963–966, Mar. 2012.

[19] S. Berciaud, M. Y. Han, K. F. Mak, L. E. Brus, P. Kim, and T. F. Heinz, “Electron and Optical Phonon Temperatures in Electrically Biased Graphene,” *Phys. Rev. Lett.*, vol. 104, no. 22, p. 227401, Jun. 2010.

[20] S. Das Sarma and E. H. Hwang, “Density-dependent electrical conductivity in suspended graphene: Approaching the Dirac point in transport,” *Phys. Rev. B - Condens. Matter Mater. Phys.*, vol. 87, no. 3, pp. 1–13, 2013.

[21] J. K. Viljas, A. Fay, M. Wiesner, and P. J. Hakonen, “Self-heating and nonlinear current-voltage characteristics in bilayer graphene,” *Phys. Rev. B - Condens. Matter Mater. Phys.*, vol. 83, no. 20, pp. 1–8, 2011.

[22] J. Y. Huang, L. Qi, and J. Li, “In situ imaging of layer-by-layer sublimation of suspended graphene,” *Nano Res.*, vol. 3, no. 1, pp. 43–50, Jan. 2010.

[23] A. Barreiro, F. Börrnert, M. H. Rümmeli, B. Büchner, and L. M. K. Vandersypen, “Graphene at high bias: Cracking, layer by layer sublimation, and fusing,” *Nano Lett.*, vol. 12, no. 4, pp. 1873–1878, 2012.

[24] J. Y. Y. Huang, F. Ding, B. I. Yakobson, P. Lu, L. Qi, and J. J. Li, “In situ observation of graphene sublimation and multi-layer edge reconstructions.,” *Proc. Natl. Acad. Sci. U. S. A.*, vol. 106, no. 25, pp. 10103–10108, Jun. 2009.

[25] J. R. Haines and C. C. Tsai, “Graphite Sublimation Tests for the Muon Collider / Neutrino Factory Target Development Program,” *Energy*, vol. 27, no. February, p. 26, 2002.

[26] Z. J. Qi, C. Daniels, S. J. Hong, Y. W. Park, V. Meunier, M. Drndic, and A. T. C. Johnson, “Electronic transport of recrystallized freestanding graphene nanoribbons,” *ACS Nano*, vol. 9, no. 4, pp. 3510–3520, Apr. 2015.

[27] C. Stampfer, J. Güttinger, S. Hellmüller, F. Molitor, K. Ensslin, and T. Ihn, “Energy Gaps in Etched Graphene Nanoribbons,” *Phys. Rev. Lett.*, vol. 102, no. 5, p. 56403, Feb. 2009.

[28] J. A. Rodríguez-Manzo, Z. J. Qi, A. Crook, J.-H. Ahn, A. T. C. Johnson, and M. Drndić, “In Situ Transmission Electron Microscopy Modulation of Transport in Graphene Nanoribbons,” *ACS Nano*, vol. 10, no. 4, pp. 4004–4010, Apr. 2016.

[29] T. Kozlova, M. Rudneva, and H. W. Zandbergen, “In situ TEM and STEM studies of reversible electromigration in thin palladium–platinum bridges,” *Nanotechnology*, vol. 24, no. 50, p. 505708, Dec. 2013.

CHAPTER 5

In-situ electron holography on graphene nanotips

This chapter is the result of collaboration with Dr. Vadim Migunov and Prof. Rafal E. Dunin-Borkowski, from the Ernst Ruska-Centre (ER-C) for Microscopy and Spectroscopy with Electrons in Julich. The collaboration aims at understanding the electric field distribution in graphene nanoribbons, sculpted with our technique, and the electrostatic charging in graphene tips.

In Chapter 5.1, we first introduce the theory of off-axis (electron) holography. Then, in Chapter 5.2, we give a brief overview on graphene nanogaps, and some techniques to map electric charge distribution on graphene. Finally, the results of in-situ electrical measurements combined with holography on graphene nanogaps are given in Chapter 5.3. Conclusions and additional experimental details are provided in Chapters 5.4 and 5.5.

5.1 Theory of off-axis holography

In general, off-axis holography is an imaging technique which uses two coherent wave sources, spatially separated but with the same frequency and fixed phase shift, to generate an interference pattern where both amplitude and phase information of the two incident waves are recorded. The phase and amplitude of these waves can be modified by the space which they traverse, changing the shape of the interference pattern. Therefore, we can say that the interference pattern is an image, or “hologram”, of the space which the waves crossed.

In the following text, when speaking about holography we may occasionally omit the term “off-axis”. However, the reader should be aware that also “in-line” holography exists (same technique with only one wave source), but we are not going to treat it in this chapter.

5.1.1 Off-axis optical holography

Optical holography was the first type of holography to be practically realized [1]: the waves are generated by a laser, a monochromatic, very coherent light source, and the interference pattern is recorded on a photographic emulsion, or, more recently, on a CCD camera. The laser beam is split into two separate beams: the first one is called “reference beam”, and it directly travels to the interference plane; the second, called the “object beam”, travels to an object of which one wants to record the “hologram”, and later it is reflected to the interference plane. When these two beams meet at the interference plane they form an interference pattern, which visually resembles a grating, with parallel dark and bright lines (called interference fringes). The spacing of the fringes, which is the distance between two consecutive dark lines, is roughly equal to the wavelength of the laser, and it slightly varies depending on the angle comprised between the reference and object beam. These tiny changes in fringe spacing and intensity (bending of the fringes), contain all the amplitude and phase information of the object one wants to record. The most interesting data is stored in the phase, as it depends on the distance that the object wave travelled, plus on the refractive index of the medium (air, water, glass…) which the wave travelled through. For example, a burning candle heats the air surrounding it, changing its refractive index: holography can record these changes, giving a map of the temperature distribution around the flame [2].

After the hologram has been recorded, the amplitude and phase information can be recovered with a “reconstruction” process: the reference beam illuminates the interference pattern, which acts as a diffraction grating; the zero-order beam goes through the grating unaffected, without producing any image; two first-order beams are diffracted at the same angle that the object beam had respect to the reference beam during recording, symmetrically respect to the zero-order beam. One of these first-order beams creates a “real image”, while the other a “virtual image”. Mathematically speaking, the virtual and real images are complex conjugate of each other, thus they contain the same amplitude and phase information (but the phase with opposite sign).

5.1.2 Off-axis electron holography

In perfect analogy with optical holography, electron holography uses electrons, instead of photons, to record holograms. Compared to photons, electrons are charged particles which can "feel" the influence of electric and magnetic fields. Therefore electron holography can be used to investigate magnetic materials, electric charge accumulation, and strain in crystals [3].

From the historical point of view, "in-line" electron holography was actually conceived even before off-axis optical holography, when Gabor proposed it as a "new microscopic principle" in 1948 [4]. The first practical realisation of off-axis electron holography came only a few years later, with the invention of the Mollenstedt biprism in 1956 [5], which is just a positively charged Au or Pt wire, functioning as a beam-splitter for electrons. Early holographic experiments faced problems with the spatial coherency of the electron source, which were solved with the introduction of the FEG (Field Emission Gun) in the 1970s [6]. Nowadays electron holography is an established technique, routinely used to map magnetic and electric fields in materials with sub-nanometer spatial resolution [7].

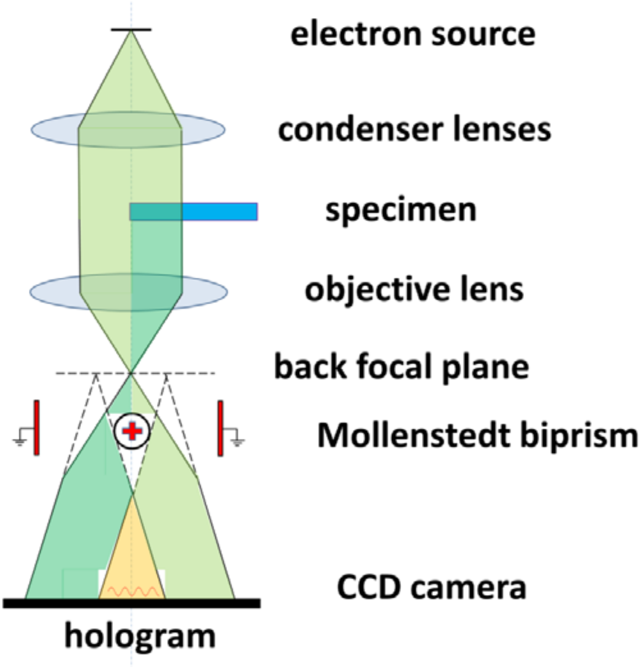

Figure 5.1 Schematic illustration of off-axis electron holography in TEM.

Moving to the practical design of an electron holography experiment, Figure 5.1 illustrates the basic modification of TEM to run in holography mode. Starting from the electron source, the first group of condenser lenses creates a parallel beam. Part of the beam goes through the sample (object beam, dark green) and part of the beam goes through a hole next to the sample (reference beam, bright green). After the beam crossing in the back focal plane, the Mollenstedt biprism bends the path of electrons, creating a zone (yellow in the figure) where the object and reference beam interfere. The interference pattern can be recorded using any position resolved electron detector (such as a CCD camera). The reconstruction of electron holograms is performed digitally, as it is described in the following section.

5.1.3 Digital acquisition and reconstruction of holograms

As already mentioned in the previous section, holograms are digitally recorded on a CCD camera (or more recently on CMOS, direct electron detectors). The hologram reconstruction is performed digitally, and it can be carried out also off-site, days after data acquisition. Figure 5.2 (a) shows the interference fringes, as recorded by the CCD camera. The fringes are parallel to the biprism direction, which is usually oriented along the diagonal of the camera to maximize fringe resolution. The inset shows a detail of the fringes, which in this case have 0.44 nm spacing. The fringe spacing is very important because it sets the spatial resolution limit of the hologram: denser fringes means higher resolution. This fact can be intuitively understood looking at the Fourier transform of the fringes, shown in Figure 5.2 (b).

We see that there are three bright “stars”, the center band and two side-bands, which correspond to the zero- and first-order beam in analogy to optical holography. The center band does not contain useful information, just as the zero-order beam, while two side-bands carry amplitude and phase information of the object under investigation. The distance of the side-bands from the center is equal to the reciprocal of the fringe spacing.

To avoid mixing of intensity between the center and the side-bands, they should be as distant as possible from the center. It is possible to demonstrate that the radius of un-perturbed intensity around one side-band is equal to 1/3rd of the center-to-side-band distance [8] (see the circle drawn around the +1 side-band in Figure 5.2(b)). Translated into direct space, this means that the best hologram spatial resolution is equal to 3 times the fringe spacing. To increase the resolution we can reduce the fringe spacing (changing the biprism voltage) at the expense of fringe contrast, which means we increase the noise in the phase image. Additionally, fringe spacing is inversely proportional to the interference distance, which, for a given position of the biprism, sets the size of the field of view. In practice, a compromise between resolution, noise and field of view should be made.

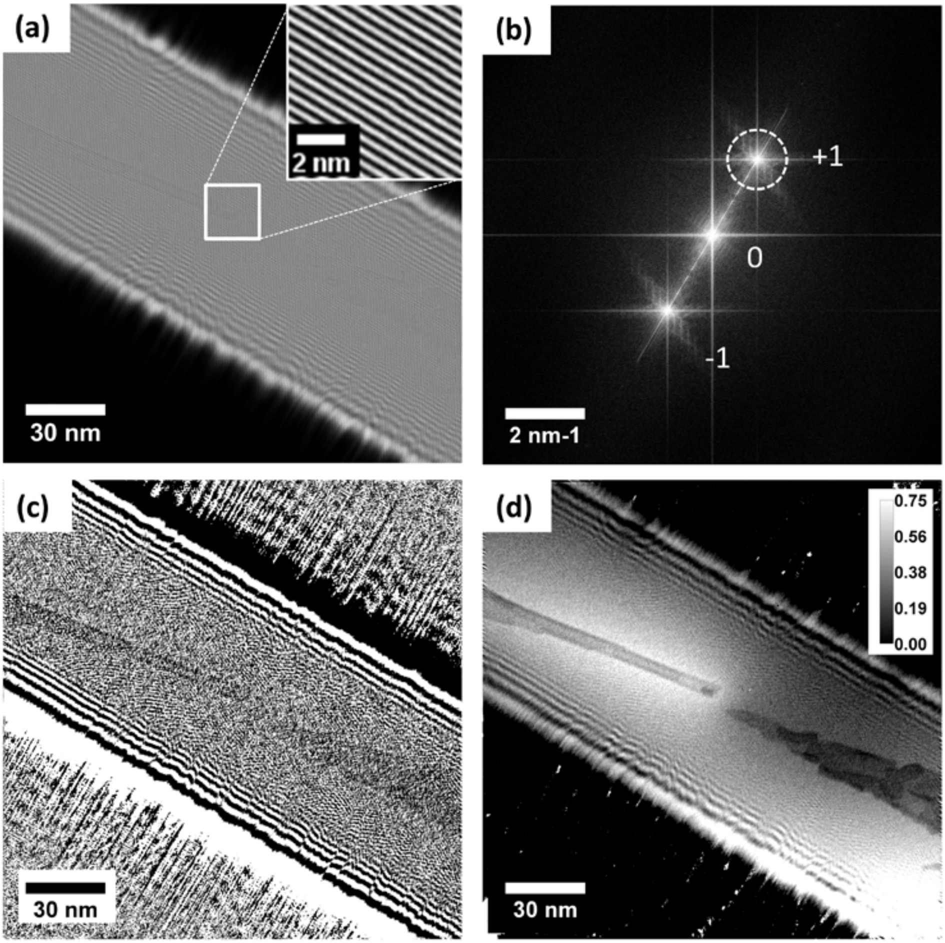

Figure 5.2 (a) Hologram as recorded on the CCD camera. The inset shows a detail of the interference fringes, with spacing 0.44 nm. (b) FFT of the image in (a), with the "zero order" in the center and the two sidebands, +1 and -1. The dotted circle around the sideband +1 indicates the low-pass filter area used to reconstruct the hologram. (c)-(d) Amplitude and phase images, respectively, after the reconstruction. The phase is shown in radians.

Finally, the reconstruction of the hologram is performed by shifting one of the sidebands to the origin, filter-out everything which is outside the 1/3rd radius, and perform the inverse Fourier transform. The result is a complex image, from which we extract amplitude, shown in Figure 5.2(c), and phase in Figure 5.2(d). In this example we have a two isolated graphene tips, electrostatically charged (see the next section for the description of the experiment): the tips are barely visible in the amplitude image, because graphene is so thin that it has little contrast in bright-field imaging; instead, they are clearly visible in the phase image. The tip on the left is brighter (higher phase) than the tip on the right because we have applied a potential difference of 4 Volts across them (if we selected the -1 sideband for the reconstruction, the phase would be inverted).

To improve the quality of holographic reconstruction, it has become common practice to acquire an additional “vacuum reference” hologram, with exactly the same settings of the “specimen” hologram. The reference hologram is taken in a totally empty area, and it is subtracted from the specimen hologram to eliminate the perturbations in the electric field given, for example, by the inhomogeneity of the Mollenstedt biprism [8].

The phase sensitivity of electron holography is limited by the phase noise, which arises due to Poisson noise in the original holograms and due to limited source spatial coherency. A good strategy to reduce the phase noise is the acquisition of a series of holograms, with short exposure time: this helps to improve Poisson statistics and to simultaneously compensate for fringe and sample drift [9].

The interested reader can find more details on holography and reconstruction in the references [3], [6]–[8], [10], [11].

After this general introduction to holography, the following sections are taken from the draft paper about the experimental work, which will be submitted soon.

5.2 Introduction to graphene nanogaps

Graphene nanogaps[*], which we define as two opposite graphene electrodes separated by a few nm gap, is a particular device geometry which has several applications in the research community. The first and most straightforward application is the nanocapacitor: two electrodes separated by a gap simply form a capacitor, whose capacitance can be tuned with the gap size and the dielectric material inserted between the electrodes. The recent fabrication of graphene supercapacitors [12], shows how promising this route can be for both the electronic industry and energy storage applications. Another potential application of graphene nanogaps lies in the fabrication of a DNA sequencing device[13], [14]: DNA is forced to move through two graphene electrodes, with maximum 2 nm gap, modulating the tunneling current that flows between them. In this case graphene is, so far, the best candidate material for this purpose because of its single atomic thickness, which allows for single nucleotide detection. In the field of molecular electronics, graphene nanogaps have been successfully used to contact single molecules [15], replacing the traditional gold electrodes. The main advantages of graphene respect to gold are the higher melting point, which allows flowing more current through the molecule without experiencing electromigration, and the reduced screening of electric fields, which allows applying

---

[*] We equivalently use the term “nanogaps” or “nanotips” in this chapter, to indicate two graphene tips separated by a nm-sized gap.

external gating to such devices. Similarly, it has been proposed to replace gold with graphene to fabricate a plasmonic dipole antenna, to be used as a plasmonic (optical) tweezer [16]. For this application, the advantages of graphene over gold are the ability to sustain surface plasmons with very low losses in the infrared and terahertz regime, and to enhance the electric field in a much more confined space, therefore reducing the laser power needed to trap sub-wavelength particles. Finally, if a very high electric field is applied across larger graphene nanogaps in a high-vacuum environment, cold field-emission might be observed, which, together with carbon nanotubes and carbon cones, has been proposed for future high-brightness, highly stable, electron sources in electron microscopes [17].

In all the applications that we considered, both the electric field inside the gap and the charge distribution on the graphene electrodes play a fundamental role in the basic design of the devices. However, traditional models, based on bulk, thick materials, may actually fail to predict these properties in a truly two-dimensional material such as graphene. Up to this moment, charge distribution in graphene flakes has been investigated with scanning tunnel microscopy (STM) [18]–[21], scanning single-electron transistor microscopy (SETSE) [22] and scanning gate microscopy (SGM) [23], to visualize the formation of elecron-hole puddles near the charge neutrality point and the electrostatic confinement of charge carriers in graphene. The STM approach delivers sub-nm spatial resolution and can detect charge density variation as small as 5×10^{-4} e/nm^2, but it requires ultra-high vacuum environment and cryogenic temperatures; moreover it is hardly scalable to large areas (more than 100x100 nm), as the scanning time increases quadratically with the imaged area. On the other hand, SETSE and SGM can be operated at ambient pressure and room temperature, and they can image larger areas, in order of several μm^2, but their resolution is limited by the size of the tip used to scan the surface, typically in the order of tens of nanometers. Neither of these techniques can, however, directly measure electric field distribution in the surroundings of a suspended, charged graphene sheet.

Off-axis electron holography in Transmission Electron Microscopy (TEM) is a consolidated technique to measure electrostatic and magnetic fields, and also charge distribution in nanoscale materials. The operation principle is similar to the classic split-beam transmission holography, but using a coherent electron source instead of a laser. While traversing the material under investigation, electrons experience a phase shift which depends on the local electric and magnetic field. The interference with a second, unperturbed, electron beam generates a set of closely spaced interference fringes, where all the phase information is stored. The hologram is then reconstructed through software processing, and the original phase information can be retrieved.

The combination of electron holography with in-situ electrical measurement considerably broadens the experimental possibilities, of which we find several examples in recent publications. The electric field has been mapped around electrically biased tungsten microtips [24], field emitting carbon nanotubes [25] and carbon cone nanotips [26], and inside directly and reverse biased p-n junctions in silicon [27]. If the sample is thin enough to be electron transparent, and if the thickness and material composition are known a-priori, it is also possibile to substract the phase contribution due to electron scattering with the material, called mean inner potential (MIP), and retrieve both the electric field and charge distribution inside the object. Some examples are the mapping of charges in biased Fe atom probe needles [28], carbon nanotubes [29], Ge nanowires undergoing lithiation [30] and charge trapping memories [31].

In the following section, we investigate the electrostatic charging and electric field distribution in a graphene nanogap, consisting of two graphene sharp, freestanding electrodes, 6-60 nm wide and separated by 8-58 nm gap, using off-axis electron holography combined with in-situ electrical measurements. We demonstrate that electron holography can map charges in graphene with nanometer resolution and single electron charge detection limit.

5.3 Experimental results of in-situ electron holography

We started from a pre-patterned graphene bridge, which was decomposed in two tips inside the TEM by applying high voltage which resulted in electrical break down (see Chapter 5.5 for details).

Figure 5.3(a) shows the phase shift measured by electron holography at zero bias voltage. In this case, the phase is simply proportional to projected electrostatic potential because the sample is not magnetic. The two graphene tips are approximately 60 nm wide in the largest part, and they are separated by a 58 nm gap. We have counted number of graphene layers for each tip by normalizing the electron phase shift at zero bias voltage with a mean phase shift produced by single graphene layer (see Figure 5.3(b)), which is about 50 mrad at 80 kV and 30 mrad at 300 kV (used here) [32]. The thickness is non-uniform, comprised mostly between 6 and 8 layers. The applied bias voltage to the tips (9.8 Volts) results in the electrostatic field, which causes additional phase shift as shown in Figure 5.3 (c). The contribution from the mean inner potential (MIP) has been subtracted in this image, to isolate the contribution of the induced charges on the tips. It is worth mentioning that such phase maps (either with or without MIP contribution) suffer from the artefacts due to perturbation of the vacuum reference wave (PRW) by the field from the specimen itself [24], which can be seen in Figure 5.3 (c) as asymmetry of the phase contours with respect to tip axis (since the biprism was placed parallel to the tips).

The electrostatic field results in induced charges in the tips, which can be estimated with the modified Poisson's equation [29], [33]:

$$\sigma_p(x,y) = -\frac{\varepsilon_0}{C_E}\nabla^2\varphi(x,y) \ , \qquad (5.1)$$

where σ_p is the projected charge density, ε_0 is the vacuum permittivity, C_E is a constant that depends on the accelerating voltage of the microscope (C_E =6.526 rad V^{-1} $\mu\mathrm{m}^{-1}$ at 300 kV), and φ is the electron phase shift. Given the fact that calculating the charge density practically requires to calculate a discrete Laplacian on a noisy image, we convolute the Laplace operator with a Gaussian blurring filter, as suggested in [33], to calculate the experimental charge distribution.

Figure 5.3 (e) shows the projected charge density distribution, calculated from Figure 5.3 (c) using Equation 5.1 and a Gaussian blur filter with 3 nm sigma. First of all, the artefacts due to PRW effect are avoided in the charge density map, because the reference wave does not contain any charges [28], though some artefacts due to numerical calculations are present at the image borders. Secondly, the charge distribution is not even, most of the charge is concentrated at the apexes of the tips where the electrostatic field is the highest. Lastly, we can calculate the total charge accumulate on the tips integrating the areas marked with dashed lines in Figure 5.3 (e). We see approximately the same number of electrons and holes at both electrodes i.e. 56±1 electrons in the top left tip and 63±1 holes in the bottom right one. The difference of about 7 unit charges can be attributed to difference in the integration areas, which is 4140 nm^2 and 4690 nm^2 in the tips with less and more charges, respectively. The error on the measurement has been estimated from the standard deviation of the charge on 10 different integration areas, taken from the same dataset. The single electron charge detection limit that we obtain here is comparable to what has been already observed in charge measurements by electron holography with similar noise levels, using cumulative acquisition techniques [9] for acquiring holograms and loop integral method for extracting total charge [28], [34].

The measurements of charge accumulated in the tips allow estimation of the capacitance of the ribbons by simply dividing the charge with the voltage applied, giving an extremely small value of approximately 1 aF. In such geometry as demonstrated here, the distance between the ribbons could be increased dramatically, therefore the voltage applied between the ribbons before onset of electron field emission can be increased as well. We have seen in our experiments that the potential of 15 V can be safely applied to the ribbons at distances of few tens of nanometers. So taking voltage of 15 V as maximum voltage that can be applied and charge of 1 electron as minimum detectable charge, the minimal detectable capacitance with electron holography at similar geometries can be estimated to 10 zF.

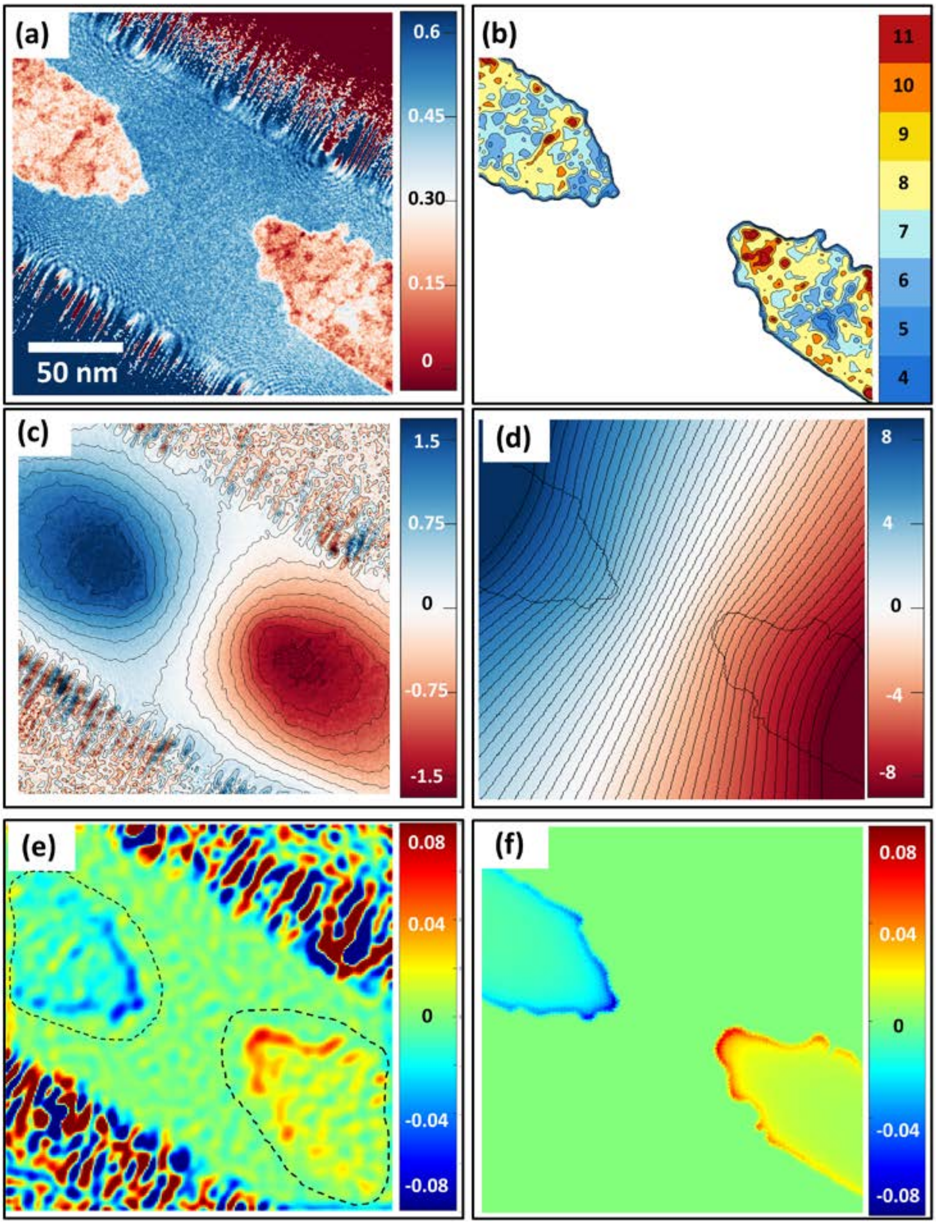

Figure 5.3 (a) Experimental phase image at zero bias voltage. (b) Graphene thickness extracted from (a), using 30 mrad for each layer. (c)-(d) Experimental and simulated phase images at 9.8 Volts, with equipotential lines spaced by 0.2 rad and by 0.4 rad, respectively. (e)-(f) Experimental and simulated projected charge density extracted from (c)-(d), after applying Gaussian blur with sigma=3 nm. The colorbars for the phase images are in radian, while the colorbar for the projected charge density is expressed in -e$^-$/nm^2. The scale bar shown in (a) is valid for all the other panels.

To give a better interpretation to our results, we have implemented FEM (Finite Element Method) simulations to see what would be the behavior of the system in a "classical" way, without any quantum effect due to the two-dimensional nature of graphene. We have faithfully reproduced the geometry of the device, including the SiN supporting membrane, and considered the graphene tip as a two-dimensional charge plane (zero thickness).

Figure 5.3 (d) shows the simulated phase shift, while Figure 5.3 (f) shows the projected charge density. The considerable difference between the experimental and simulated phase images can be almost completely attributed to the PRW effect. This difference disappears in the charge density maps, where the PRW has no effect. According to the simulation we have 56 electrons in the top left tip and 60 holes in the bottom right one, which is in remarkable good agreement with the experimental results. It seems therefore that quantum effects, if present at all, play a negligible role in the charge distribution of 60 nm wide, multi-layer graphene tips. From the simulation we can also extrapolate that the total capacitance of the device, including the parts which have not been imaged with holography (not shown here), is 30 aF.

We have repeated measurements of charge distribution in another graphene sample with fewer layers, shown in Figure 5.4. The top left tip is approximately 6 nm wide, with a thickness comprised between 3 and 6 layers; the bottom right tip has a triangular shape, and it is only 1-2 layers thick in the narrowest part; the tips are separated by an 8 nm gap. Given the very small distance between the tips, we only applied 4 V bias to avoid the release of electric sparks between them. In fact, the TEM column is in high vacuum ($\sim 10^{-7}$ mbar) , but not ultra-high vacuum ($<10^{-9}$ mbar), which is desirable for stable field emission without discharges.

The experimental charge distribution, shown in Figure 5.4(e), seems to indicate that the charge is uniformly distributed across the tip width, contrary to the previous, larger device which had the charge mostly concentrated on the edges. We attribute this effect to the limited spatial resolution of the hologram, which is 1.3 nm based on the fringe spacing and on the Gaussian blurring required to perform the numerical Laplacian. Integrating the charge density, we find that the top left tip has 19±1 electrons, while the other, thinner tip has 16±1 holes, corresponding to an average capacitance of 0.7 aF. Here the unbalance in the charge distribution cannot be related to the integration area, because the tip with fewer charges has a bigger surface (612 nm^2 and 1000 nm^2, for the tip with more and fewer charges, respectively). To find an answer to the problem we have to look at the whole device geometry, on the µm scale.

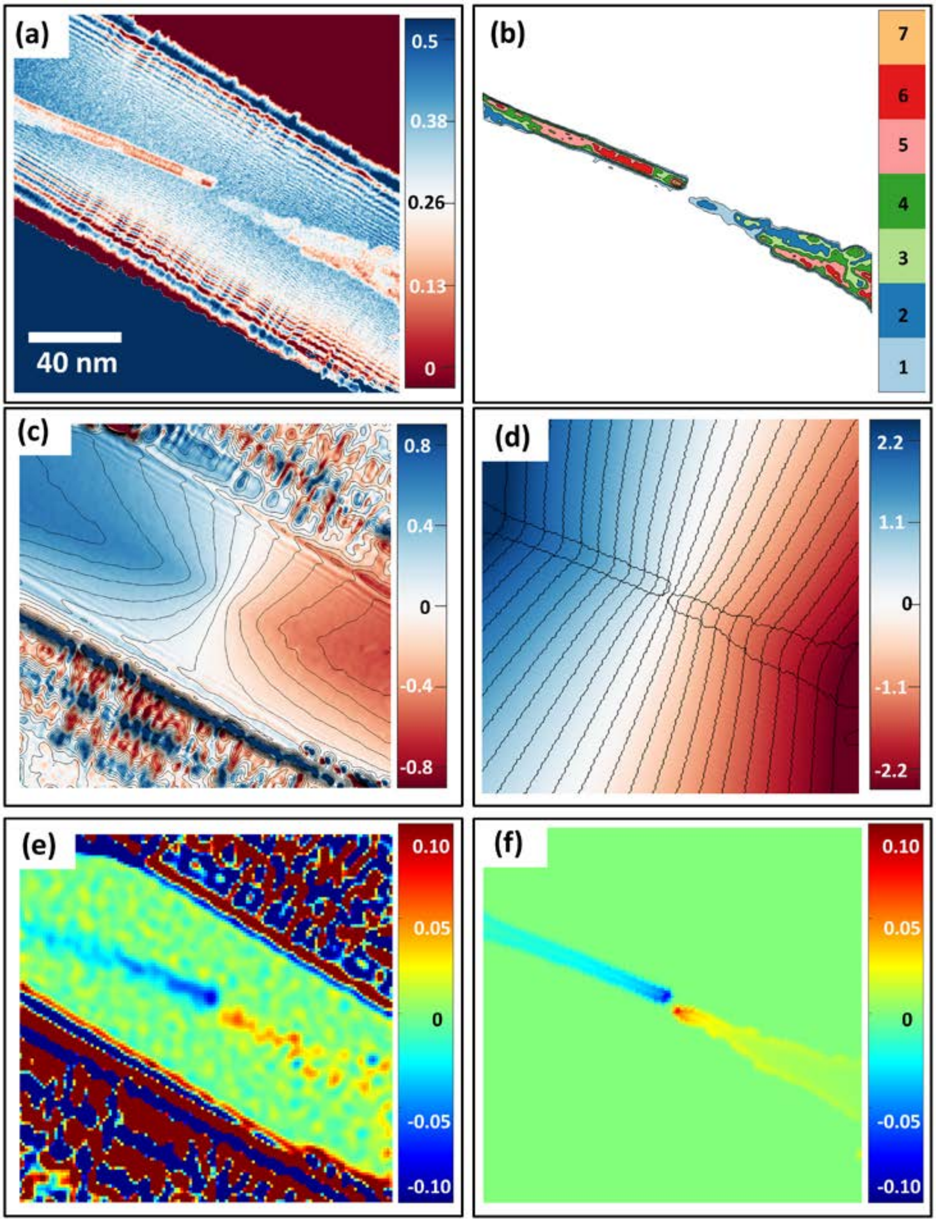

Figure 5.4 (a) Experimental phase image at zero bias voltage. (b) Graphene thickness extracted from (a), using 30 mrad for each layer. (c)-(d) Experimental and simulated phase images at 4 Volts, with equipotential lines spaced by 0.1 rad and by 0.2 rad, respectively. (e)-(f) Experimental and simulated projected charge density extracted from (c)-(d), after applying Gaussian blur with sigma=2.6 nm. The colorbars for the phase images are in radian, while the colorbar for the projected charge density is expressed in -e-/nm^2. The scale bar shown in (a) is valid for all the other panels.

Looking at Figure 5.5(a), we can see a low-magnification STEM image of the suspended graphene tips, and we notice that the top left part is considerably shorter than the other one (this choice was obliged by a pre-existing constriction of the original ribbon in that point, therefore not intentional). This fact implies that the shorter tip has a higher charge density respect to the long tip, because the total charge must be equal on both of them. The simulation, shown in Figure 5.4(f) and Figure 5.5(b), confirms this charge unbalance due to the asymmetric geometry of the device: 16 electrons and 13 holes, in the top left and bottom right tips, respectively. At the moment of this writing, it remains unclear why the simulated charge is, on average, 20% lower than the experimental one. From the simulation we can also extrapolate the total device capacitance, estimated around 12.5 aF.

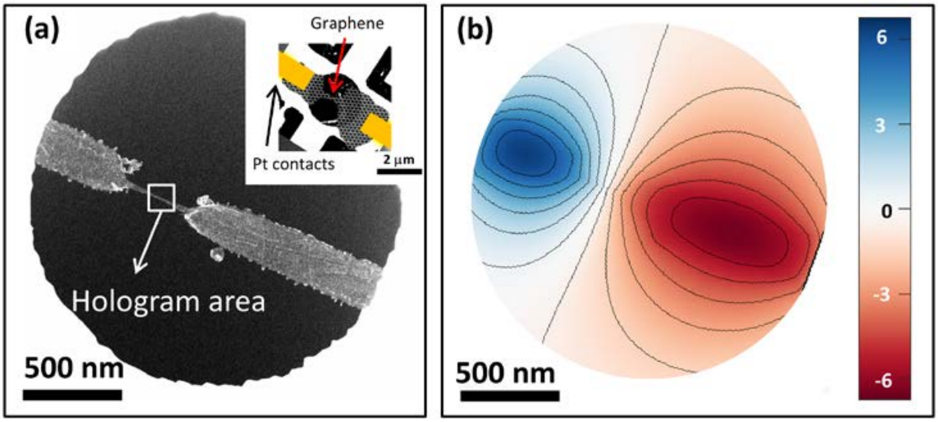

Figure 5.5 (a) Low-magnification HAADF-STEM image of the whole suspended graphene structure, corresponding to the device shown in Figure 5.4. The large black disk corresponds to a hole in the SiN supporting membrane, which is 2 µm in diameter. The area where the hologram was acquired is indicated by the small white square. The inset in the top left corner is a lower magnification image, showing the Pt contacts (schematically painted in yellow) (b) FEM simulation of the phase shift of the same area shown in (a), with equipotential lines spaced by 1 rad. The colorbar is in radian.

As this sample is only 1-2 layers thick on one tip, we would expect also some contribution from graphene QC (Quantum Capacitance). How could we estimate it? Most experiments and theoretical predictions found in literature [35]–[39] deal with a parallel plate capacitor configuration, where the QC is expressed in µF/cm^2. Despite the fact that our geometry is very different from the parallel plate configuration, we can still make a rough estimate of the lowest limit for the QC. Suppose the extreme ends of the device tips were actually parallel to each other, instead of being opposed: given the QC per unit area in monolayer graphene equal to 0.8 µF/cm^2 [37], the QC is 1.3 aF for a surface of 160 nm^2. The geometrical capacitance on the same area is 0.12 aF, approximately 10 times smaller than the QC. Therefore we can conclude that QC could reduce the capacitance of the monolayer tip by ~10%. In multilayer graphene the effect would be even smaller, less than 2% difference, as typical values for QC are in the 4-10 μF/cm^2 range [38], [39].

A 10% difference in charge is, in principle, within the sensitivity range of our holographic measurements. However, the charge unbalance given by the QC effect on the monolayer tip matches, for a pure coincidence, the unbalance given by the asymmetric shape of the device. Being experimentally impossible to distinguish between these two contributions, we cannot quantify the QC effect in this particular device.

5.4 Conclusions

We mapped the charge distribution inside a biased graphene nanotip using in-situ electron holography. The precision of the charge counting is close to a single electron, with a spatial resolution limit of 1 nm. We estimate the contribution of quantum capacitance in multilayer graphene to be completely negligible. Due to coincidental asymmetric device geometry, it remains unclear whether quantum capacitance plays a role in the asymmetric charge distribution of the monolayer graphene tip.

Future experiments will further investigate field-emission and possibly add a tomography study. The fabrication of fully symmetric devices with monolayer graphene tips could also reveal the contribution of quantum capacitance.

5.5 Experimental: sample preparation details

Devices are fabricated similarly to what has been described in Chapter 3 of this thesis. *In-situ* off-axis electron holography experiments combined with simultaneous electrical biasing were performed in FEI Titan G2 60-300 HOLO TEM [40] operated at 300 kV. The microscope was equipped with Möllenstedt type [5] electrostatic biprism situated above first image plane. The biprism potential was set to approximately 75 V, resulting in fringe spacing of 0.43 nm with 24.5% contrast (pixel size 0.084 nm) for the device shown in Figure 5.3 and 0.33 nm spacing with 14.5% contrast (pixel size 0.106 nm) for the device in Figure 5.4 and Figure 5.5.

Prior irradiating the specimen with electron beam, the specimen temperature was set to 523 K with an integrated Joule heating coil. At this temperature, most of the water moisture and hydrocarbon residues are removed from the graphene surface, so that the beam-induced carbon deposition is extremely reduced. To form the gap in the nanoribbon, ~2.5 V bias was applied across it, which induced the breakdown due to electro/thermo-migration. After the junction formation, the temperature was set back to ambient and a series of 10 holograms was acquired at each bias voltage. Averaging the 10 holograms, with drift correction, reduces the phase noise approximately by a factor 2, from ~150 mrad to ~80 mrad, measured as standard deviation of phase in vacuum. In terms of charge noise, this is equivalent to 0.16 e/nm^2 and 0.08 e/nm^2, respectively, after applying Gauss filter with 1 nm sigma. To correct for phase distortions of imaging system of the TEM, a vacuum reference hologram was acquired in field free vacuum region. The holograms were reconstructed using standard Fourier method involving recentring and filtering of a side band with consequent inverse fast Fourier transformation [41]. All further image processing including image alignment, numerical calculations of phase differences and Laplacian were done using self-made scripts in MathWorks Matlab software package.

Finite Element Method simulations were performed in Comsol Multiphysics ® v5.2. The total volume of the simulation was set to a cylinder with 5 μm height and 5 μm diameter, which was enough to contain most of the generated electric field. The simulation data was exported from Comsol to Matlab for post-processing: the phase shift was obtained integrating the electrostatic potential along the z direction (perpendicular to the tips plane); the electrostatic charge was blurred with a Gaussian filter, similarly to those applied on the experimental data.

References

[1] E. N. Leith and J. Upatnieks, “Wavefront Reconstruction with Continuous-Tone Objects,” *J. Opt. Soc. Am.*, vol. 53, no. 12, pp. 1377–1381, Dec. 1963.

[2] D. W. Sweeney and C. M. Vest, “Temperature fields above heated surfaces,” *Int. J. Heat Mass Transf.*, vol. 17, pp. 1443–1454, 1974.

[3] E. Snoeck, “Special issue on developments of electron holography for material science,” *J. Phys. D. Appl. Phys.*, vol. 49, no. 38, p. 380201, Sep. 2016.

[4] D. Gabor, “A new microscopic principle.,” *Nature*, vol. 161, no. 4098. pp. 777–778, 1948.

[5] G. Möllenstedt and H. Düker, “Beobachtungen und Messungen an Biprisma-Interferenzen mit Elektronenwellen,” *Zeitschrift für Phys.*, vol. 145, no. 3, pp. 377–397, Jun. 1956.

[6] G. F. Missiroli, G. Pozzi, and U. Valdre, “Electron interferometry and interference electron microscopy,” *J. Phys. E.*, vol. 14, no. 6, pp. 649–671, Jun. 1981.

[7] T. Tanigaki, K. Harada, Y. Murakami, K. Niitsu, T. Akashi, Y. Takahashi, A. Sugawara, and D. Shindo, “New trend in electron holography,” *J. Phys. D. Appl. Phys.*, vol. 49, no. 24, p. 244001, Jun. 2016.

[8] T. Kasama, R. E. Dunin-Borkowski, and M. Beleggia, *Holography - Different Fields of Application*. InTech, 2011.

[9] E. Voelkl and D. Tang, “Approaching routine 2π/1000 phase resolution for off-

axis type holography," *Ultramicroscopy*, vol. 110, no. 5, pp. 447–459, 2010.

[10] F. Börrnert, A. Lenk, A. Lubk, F. Röder, J. Sickmann, S. Sturm, K. Vogel, and D. Wolf, "Electron holography for fields in solids: Problems and progress," *Ultramicroscopy*, vol. 134, pp. 126–134, 2013.

[11] G. Pozzi, "Chapter Ten – Off-Axis Electron Holography: A Short Introduction," in *Advances in Imaging and Electron Physics*, vol. 194, 2016, pp. 245–269.

[12] M. D. Stoller, S. Park, Z. Yanwu, J. An, and R. S. Ruoff, "Graphene-Based ultracapacitors," *Nano Lett.*, vol. 8, no. 10, pp. 3498–3502, 2008.

[13] H. W. Ch Postma, "Rapid sequencing of individual DNA molecules in graphene nanogaps," *Nano Lett.*, vol. 10, no. 2, pp. 420–425, 2010.

[14] S. J. Heerema and C. Dekker, "Graphene nanodevices for DNA sequencing," *Nat. Nanotechnol.*, vol. 11, no. 2, pp. 127–136, Feb. 2016.

[15] F. Prins, A. Barreiro, J. W. Ruitenberg, J. S. Seldenthuis, N. Aliaga-Alcalde, L. M. K. Vandersypen, and H. S. J. Van Der Zant, "Room-temperature gating of molecular junctions using few-layer graphene nanogap electrodes," *Nano Lett.*, vol. 11, no. 11, pp. 4607–4611, 2011.

[16] J.-D. Kim and Y.-G. Lee, "Graphene based plasmonic tweezers," *Carbon N. Y.*, vol. 103, pp. 281–290, 2016.

[17] F. Houdellier, L. de Knoop, C. Gatel, A. Masseboeuf, S. Mamishin, Y. Taniguchi, M. Delmas, M. Monthioux, M. J. Hÿtch, and E. Snoeck, "Development of TEM and SEM high brightness electron guns using cold-field emission from a carbon nanotip," *Ultramicroscopy*, vol. 151, pp. 107–115, Apr. 2015.

[18] Y. Zhang, V. W. Brar, C. Girit, A. Zettl, and M. F. Crommie, "Origin of spatial charge inhomogeneity in graphene," *Nat. Phys.*, vol. 5, pp. 722–726, 2009.

[19] S. Samaddar, I. Yudhistira, S. Adam, H. Courtois, and C. B. Winkelmann, "Charge Puddles in Graphene near the Dirac Point," *Phys. Rev. Lett.*, vol. 116, no. 12, p. 126804, 2016.

[20] J. Lee, D. Wong, J. Velasco, J. F. Rodriguez-Nieva, S. Kahn, H. Tsai, T. Taniguchi, K. Watanabe, A. Zettl, F. Wang, L. S. Levitov, and M. F. Crommie, "Imaging electrostatically confined Dirac fermions in graphene quantum dots," *Nat. Phys.*, no. June, pp. 1–6, 2016.

[21] R. Decker, Y. Wang, V. W. Brar, W. Regan, H.-Z. Tsai, Q. Wu, W. Gannett, A. Zettl, and M. F. Crommie, "Local Electronic Properties of Graphene on a BN Substrate via Scanning Tunneling Microscopy," *Nano Lett.*, vol. 11, no. 6, pp. 2291–2295, 2011.

[22] J. Martin, N. Akerman, G. Ulbricht, T. Lohmann, J. H. Smet, K. von Klitzing, and A. Yacoby, "Observation of Electron-Hole Puddles in Graphene Using a Scanning Single Electron Transistor," *Nat. Phys.*, vol. 4, no. February, pp. 144–148, 2008.

[23] R. Jalilian, L. a Jauregui, G. Lopez, J. Tian, C. Roecker, M. M. Yazdanpanah, R. W. Cohn, I. Jovanovic, and Y. P. Chen, "Scanning gate microscopy on graphene: charge inhomogeneity and extrinsic doping.," *Nanotechnology*, vol. 22, no. 29, p. 295705, 2011.

[24] G. Matteucci, G. F. Missiroli, M. Muccini, and G. Pozzi, "Electron holography in the study of the electrostatic fields: the case of charged microtips," *Ultramicroscopy*, vol. 45, no. 1, pp. 77–83, Aug. 1992.

[25] J. Cumings, A. Zettl, M. R. McCartney, and J. C. H. Spence, "Electron Holography of Field-Emitting Carbon Nanotubes," *Phys. Rev. Lett.*, vol. 88, no. 5, p. 56804, Jan. 2002.

[26] L. de Knoop, C. Gatel, F. Houdellier, M. Monthioux, A. Masseboeuf, E. Snoeck, and M. J. Hÿtch, "Low-noise cold-field emission current obtained between two opposed carbon cone nanotips during in situ transmission electron microscope biasing," *Appl. Phys. Lett.*, vol. 106, no. 26, p. 263101, 2015.

[27] A. C. Twitchett, R. E. Dunin-Borkowski, R. J. Hallifax, R. F. Broom, and P. A. Midgley, "Off-axis electron holography of electrostatic potentials in unbiased and reverse biased focused ion beam milled semiconductor devices," *J. Microsc.*, vol. 214, no. 3, pp. 287–296, 2004.

[28] V. Migunov, A. London, M. Farle, and R. E. Dunin-Borkowski, "Model-independent measurement of the charge density distribution along an Fe atom probe needle using off-axis electron holography without mean inner potential effects," *J. Appl. Phys.*, vol. 117, no. 13, p. 134301, Apr. 2015.

[29] M. Beleggia, T. Kasama, R. E. Dunin-Borkowski, S. Hofmann, and G. Pozzi, "Direct measurement of the charge distribution along a biased carbon nanotube bundle using electron holography," *Appl. Phys. Lett.*, vol. 98, no. 24, p. 243101, 2011.

[30] Z. Gan, M. Gu, J. Tang, C.-Y. Wang, Y. He, K. L. Wang, C. Wang, D. J. Smith, and M. R. McCartney, "Direct Mapping of Charge Distribution during Lithiation of Ge Nanowires Using Off-Axis Electron Holography," *Nano Lett.*, vol. 16, no. 6, pp. 3748–3753, 2016.

[31] Y. Yao, C. Li, Z. L. Huo, M. Liu, C. X. Zhu, C. Z. Gu, X. F. Duan, Y. G. Wang, L. Gu, and R. C. Yu, "In situ electron holography study of charge distribution in high-κ charge-trapping memory.," *Nat. Commun.*, vol. 4, p. 2764, 2013.

[32] L. Ortolani, F. Houdellier, M. Monthioux, E. Snoeck, and V. Morandi, "Surface electrostatic potentials in carbon nanotubes and graphene membranes

investigated with electron holography," *Carbon N. Y.*, vol. 49, no. 4, pp. 1423–1429, 2011.

[33] M. Beleggia, L. C. Gontard, and R. E. Dunin-Borkowski, "Local charge measurement using off-axis electron holography," *J. Phys. D. Appl. Phys.*, vol. 49, no. 29, p. 294003, Jul. 2016.

[34] C. Gatel, A. Lubk, G. Pozzi, E. Snoeck, and M. Hÿtch, "Counting elementary charges on nanoparticles by electron holography," *Phys. Rev. Lett.*, vol. 111, no. 2, 2013.

[35] S. Dröscher, P. Roulleau, F. Molitor, P. Studerus, C. Stampfer, K. Ensslin, T. Ihn, S. Dröscher, P. Roulleau, F. Molitor, P. Studerus, C. Stampfer, K. Ensslin, and T. Ihn, "Quantum capacitance and density of states of graphene," *Appl. Phys. Lett.*, vol. 96, no. 15, p. 152104, 2010.

[36] T. Fang, A. Konar, H. Xing, and D. Jena, "Carrier statistics and quantum capacitance of graphene sheets and ribbons," *Appl. Phys. Lett.*, vol. 91, no. 9, 2007.

[37] J. Xia, F. Chen, J. Li, and N. Tao, "Measurement of the quantum capacitance of graphene," *Nat Nanotechnol*, vol. 4, no. 8, pp. 505–509, 2009.

[38] C. Zhan, J. Neal, J. Wu, and D. E. Jiang, "Quantum Effects on the Capacitance of Graphene-Based Electrodes," *J. Phys. Chem. C*, vol. 119, no. 39, pp. 22297–22303, 2015.

[39] H. Ji, X. Zhao, Z. Qiao, J. Jung, Y. Zhu, Y. Lu, L. L. Zhang, A. H. MacDonald, and R. S. Ruoff, "Capacitance of carbon-based electrical double-layer capacitors," *Nat. Commun.*, vol. 5, no. Cmcm, p. 3317, Feb. 2014.

[40] S. L. Y. Chang, C. Dwyer, J. Barthel, C. B. Boothroyd, and R. E. Dunin-Borkowski, "Performance of a direct detection camera for off-axis electron holography," *Ultramicroscopy*, vol. 161, pp. 90–97, 2016.

[41] A. Tonomura, "Applications of electron holography," *Rev. Mod. Phys.*, vol. 59, no. 3, pp. 639–669, Jul. 1987.

CHAPTER 6

Experimental methods

This last chapter contains all the experimental details which were not included in the main part of this thesis. Despite being the last chapter, its relevance should not be underestimated, as most of a research is hidden in the small details.

It mostly contains information on the MEMS heating devices, including their cleanroom fabrication (Chapter 6.1), temperature calibration (Chapter 6.2), properties of the SiN membrane (Chapter 6.3) and Finite Element Method simulation (Chapter 6.4). Chapter 6.5 contains an estimate on the strain applied to the suspended graphene ribbons. Chapter 6.6 is dedicated to the very delicate problem of amorphous carbon graphitization on the Silicon Nitride membrane, which brought us to substantially change the initial design of the Graphene nanoribbon experiment. The graphene wedging transfer technique is explained in Chapter 6.7. In Chapter 6.8 and 6.9 we analyze the graphene-metal contact resistance, using four-probe measurements. Ex-situ liquid gating of graphene is explained in Chapter 6.10. Analysis of metal impurities on graphene with EDX is reported in Chapter 6.11. The design of the ten-pin TEM holder is presented in Chapter 6.12. Finally, Chapter 6.13 contains information about the electrical measurement setup, including considerations on electrical noise and some possible solutions to minimize it.

6.1 MEMS in-situ heaters fabrication in cleanroom

In this section we describe all the steps that are needed to fabricate our MEMS heating chips, starting from a bare silicon wafer. We briefly give an overview of the whole process, and later provide the detailed procedure.

The manufacturing of the chips is divided in two main parts: in the first part we produce the MEMS heater without electrodes and without holes or slits in the silicon nitride; this step is performed on 4-inch Silicon wafers and the layers are exposed with optical lithography only. It takes approximately 4 weeks to complete this first part. At this point we start the second part of the fabrication, where we fabricate the platinum electrodes and the SiN slit/holes through electron beam lithography. Since a full 4-inch wafer contains approximately 100 MEMS heaters, in this second part we prefer to cut it, or “dice”, in smaller blocks, each containing 12-25 chips, depending on the size. We process each block separately, so that we can adjust the electrodes design to accommodate our needs. Finally, we cut the blocks in single chips, ready to use. This second part takes an additional 1-2 weeks, and the yield of the whole process is around 70%.

The following part describes the fabrication in detail.

Start from a 4-inch Silicon wafer, p-doped, single side polished, <100> orientation, 525 μm thick. The wafer already has the “zero” layer, containing the markers to align optical lithography layers, engraved on the polished side. Then follow all the steps listed in Table 6.1 to obtain the MEMS heater (1st part only, without electrodes and graphene). Read Tables 6.2, 6.3 and 6.4 for the details of various cleanroom “cooking” recipes. Continue with the final steps, described in Table 6.5 to obtain a ready-to-measure graphene sample. Table 6.6 contains a small glossary.

Table 6.1 List of steps for the 1st part of MEMS heaters fabrication.

1st PART – MEMS heater fabrication on 4-inch wafers			
Step#	**Step description**	**Step #**	**Step description**
(1)	Remove native oxide from wafer with HF cleaning	(2)	Remove organic and metallic contamination with RCA 1+2 cleaning
(3)	Deposit 200 nm LPCVD Silicon Nitride (both sides of the wafer)	(4)	Deposit 20 nm Tantalum and 180 nm Platinum on the top side of wafer (polished side)
(5)	Optical lithography to pattern the heating coil shape. Use bright field mask and positive resist AZ5214.	(6)	Etch the Ta/Pt film with Ion Beam Milling.
(7)	Remove photoresist with Oxygen plasma	(8)	Remove organic and metallic contamination with RCA 1+2 cleaning
(9)	Deposit 200 nm LPCVD Silicon Nitride (both sides of the wafer)	(10)	Optical lithography to pattern the contact pads shape. Use dark field mask and positive resist AZ5214.
(11)	Etch 200 nm SiN with RIE from top of the exposed contact pads. Etching time 15 minutes.	(12)	Strip photoresist with oxygen plasma
(13)	Optical lithography to pattern the KOH etching windows (on the back side of the wafer). Use dark field mask and positive resist AZ5214.	(14)	Etch 400 nm SiN from the back side of the wafer, on top of the KOH windows areas. Etching time 30 minutes.
(15)	Strip photoresist with oxygen plasma	(16)	Perform KOH etching of Silicon to obtain the SiN membrane. Etch 5 hours @85°C for a 525 μm thick wafer.
(17)	Spincoat the wafer with thick resist (S1818) on both sides, as a protective coating during the dicing.	(18)	Dice the wafer in blocks 2x2 cm each.
(19)	Use acetone cleaning to remove photoresist residues and silicon particles after dicing.	(20)	Use nitric acid cleaning to remove all the possibly remaining photoresist residues.

Table 6.2 General description of the cleanroom procedures to clean Silicon wafers and MEMS heaters from resist residues, organic and metal contaminants.

Standard cleaning procedures	
Procedure	**Description**
HF cleaning	Use hydrofluoric acid, 2% concentration, for 30 seconds to remove the native Silicon Oxide from the wafer.
RCA 1+2 cleaning	Standard cleaning for silicon wafers. RCA-1 removes organic contaminants, while RCA-2 removes metal contaminants. For RCA-1, mix $NH_4OH : H_2O_2 : H_2O$ with ratio 1 : 1 : 5. Heat up @ 70°C and insert the wafer for 10 minutes. Rinse with water before continuing with RCA-2. For RCA-2, mix $HCl : H_2O_2 : H_2O$ with ratio 1: 1: 5. Heat up @ 70°C and insert the wafer for 10 minutes. Rinse with water and dry with N_2 gun.
Nitric Acid cleaning	To strip resist and organic contaminants from wafer and chips. Use fuming Nitric acid (HNO3), 90% concentration, for 10 minutes at room temperature. Rinse in abundant water.
Strong Oxygen plasma cleaning	To strip resist and organic contaminants from wafers. Use PVA TePla 300, microwave plasma system. Oxygen flow 200 sccm, power 500 Watt, chamber pressure 0.8 mbar. Remove the Faraday cage. Process time depends on resist thickness (typically 5-10 minutes). Use only on wafers, before the KOH etching. If used on chips with SiN window, the microwave source of the plasma inductively couples with the heating coil in the chip, which will overheat and melt, because of limited heat dissipation.
Mild oxygen plasma cleaning	To remove carbon contaminants from chips and to make the surface hydrophilic before the graphene wedging transfer. Identical to the strong oxygen plasma, but 200 Watt power and use the Faraday cage. Process for at least 10 minutes. Safe to use both on wafers and chips with SiN windows.
Acetone cleaning	To gently remove resist residues from wafer and chips. Not as effective as oxygen plasma or nitric acid. Use acetone heated @50°C. Depending on resist type and thickness, processing time can vary considerably (from 10 minutes to several hours). When the cleaning is finished, directly transfer the wafer/chip from acetone to isopropanol (IPA), without drying. Finally. dry with N_2 gun.

Table 6.3 General description of other cleanroom procedures for device fabrication.

Other procedures	
Procedure	**Description**
Silicon Nitride etching with RIE	Reactive Ion Etching (RIE) is used to etch Silicon Nitride. Use Leybold F-system, Argon 25 sccm, CHF_3 25 sccm, chamber pressure 8 µbar, power 50 Watt. Silicon Nitride etching rate varies considerably depending on the feature size to be etched. For small features (~1-2 µm), slow etching rate= 17±2 nm/min. For large features (>10 µm), fast etching rate 23±2 nm/min. The process is very anisotropic, leading to vertical, straight etch profiles. ZEP520A etching rate is 11±1 nm/min.
KOH etching of Silicon	Potassium hydroxide (KOH) etching is used to etch Silicon. Mix KOH salt in water to obtain ~33% concentration (1 kg KOH salt in 2.5 liters of water). Heat up @85°C and insert the wafer. Etching rate is 100 µm/hour. At the end, rinse the wafer in abundant water for several hours to remove the KOH residues.
Silicon Nitride deposition	Silicon nitride (SiN) is deposited with Low Pressure Chemical Vapor Deposition (LPCVD) on the Silicon wafer. The resulting Silicon Nitride is low-stress (100 MPa tensile stress) and Silicon rich (Si:N ratio 1:1).
Dicing	To cut, or “dice”, the wafer in blocks and single chips. We use a DISCO - DAD3240 automatic dicing saw, with 50 µm thick diamond coated blade.
Graphene etching with RIE	RIE is used to etch graphene after PMMA mask is applied. Use Leybold F-system, oxygen 20 sccm, chamber pressure 8 µbar, power 20 Watt. Etch for 1 minute. PMMA etching rate is ~150 nm/min.
Optical lithography	Optical lithography is used to pattern various layers on the 4-inch wafer, with minimum feature size of ~1 µm. We use 5-inch square soda-lime glass photomasks on an EVG 620 mask aligner (365 nm Near UV light). The lamp irradiance is 10 mW/cm^2. With 15 seconds exposure we obtain the required clearing dose for the photoresist AZ5214E (150 mJ/cm^2)
Electron beam lithography (EBL)	EBL is used to pattern various layers on the blocks of chips (2x2 cm size). The electron-beam resist is exposed with an electron beam, accelerated at 100 keV, generated by a Leica EBPG 5000+.
Electrode deposition	E-beam evaporator (Temescal FC-2000) is used to deposit Ti/Pt electrodes, which will be used to measure the graphene electrical properties. First deposit adhesion layer of Ti, 5 nm with 0.5 A/sec deposition rate, then Pt layer, 70 nm at 1.5 A/sec.

Table 6.4 List of all the e-beam and photo- resist used in the process.

Photo/E-beam resist recipes		
Resist name/type	**Used for these steps:**	**Processing details**
AZ5214E Positive photoresist	Optical lithography	Spincoat 5000 rpm, bake 1 min on hotplate @90°C. Exposure dose 150 mJ/cm^2 with Near UV light (365 nm). Develop in MF321 for 1 min, rinse 30sec in DI water.
S1818 positive photoresist	Protection coating during dicing	Spincoat top side of the wafer at 1000 rpm. Bake 5 min in oven @90°C. Flip the wafer and spincoat the back side. Bake again for 30 min. Thickness ~5 µm. Exposure not needed.
ZEP520A Positive e-beam resist	EBL of SiN slits	Use stock solution, do not dilute. Spincoat 3000 rpm, bake 15 min on hotplate @175°C. 420 nm thickness. Exposure dose 240-320 µC/cm^2 with 100 kV e-beam. Develop in o-Xylene for 90 sec, rinse 1 min in IPA.
PMMA/MMA Double layer Positive e-beam resist	EBL of Ti/Pt electrodes	1st layer: MMA copolymer, 17.5 %wt, 8% in Ethyl Lactate. Spincoat 3000 rpm, bake 10 min on hotplate @175°C. 300 nm thickness 2nd layer: PMMA 950k, 3% in anisole. Spincoat 3000 rpm, bake 20 min on hotplate @175°C. 130 nm thick. Exposure dose: 1000 µC/cm^2 with 100 kV e-beam. Develop in MIBK:IPA, 1:3 ratio, for 70 sec, rinse 30 sec in IPA.
PMMA Single layer Positive e-beam resist	EBL of graphene etching mask.	PMMA 950k, 3% in anisole. Spincoat 2000 rpm, bake 10 min on hotplate @175°C. 200 nm thick. Expose and develop as PMMA/MMA recipe.

Table 6.5 List of steps for the 2nd part of MEMS heater fabrication, including graphene transfer and pre-patterning.

2nd PART – Platinum electrodes, SiN slits and graphene pre-patterning			
Step #	**Step description**	**Step #**	**Step description**
(1)	EBL to expose the electrical contacts. Use e-beam resist PMMA/MMA double layer.	(2)	Deposit 5 nm titanium and 60 nm platinum with e-beam evaporator. Lift-off in warm acetone. Don't use ultrasound sonication.
(3)	EBL to expose the SiN slits. Use e-beam resist ZEP520A	(4)	Etch the SiN slits with RIE. Etching time is 35 minutes, for 400 nm thick SiN.
(5)	Spincoat the block with thick resist (S1818) on both sides, as a protective coating during the dicing.	(6)	Dice the block in single chips.
(7)	Use nitric acid cleaning to remove e-beam resist residues.	(8)	Use mild oxygen plasma to remove carbon residues and make the surface hydrophilic
(9)	Transfer graphene on top of platinum electrodes with wedging technique (see Chapter 6.7). This step must be done within a few hours from the oxygen plasma, otherwise hydrophilicity is lost.	(10)	EBL to expose the graphene wide ribbons mask (300 nm - 1μm width). Use e-beam resist PMMA single layer.
(11)	Etch the graphene wide ribbon with oxygen plasma.	(12)	Insert the sample in TEM and connect the heating box. Heat up at the coil at 400°C to burn the PMMA which was used as an etching mask on graphene.

Table 6.6 Glossary, containing the most frequently used acronyms for fabrication

Glossary	
ACE	Acetone
EBL	Electron Beam Lithography
EBPG	Electron Beam Pattern Generator
IPA	Isopropyl alcohol
LPCVD	Low Pressure Chemical Vapor Deposition
MIBK	Methyl-iso-butylketon
MMA	Methyl methacrylate
PMMA	Polymethyl methacrylate
RIE	Reactive Ion Etching

6.2 Temperature calibration of the MEMs heater

The temperature reached by the heaters is measured with two independent methods. The first method consists in dropping Silicon powder on the surface of the SiN and measuring the Raman shift of the 521 cm^{-1} Stokes line, whose position and linewidth are temperature dependent [1]–[4]. The laser spot size of 1 micron allows a precise mapping of the temperature on the surface. The second method consists in measuring the temperature with a pyrometer, calibrated by the manufacturer. The smallest detail that the pyrometer can resolve is 350 μm in diameter, therefore the measured temperature is an average over the whole heater. The specifications of our pyrometer also limit the measureable temperature in the range 600 K – 1600 K.

The results from the two calibration methods are listed in Table 6.7. As we can see, the readings from the pyrometer are consistently equal or lower than those from the Raman calibration, compatible with the fact that the pyrometer measures an average temperature and not the local maximum.

From both the Raman and the Pyrometer calibration when can extract the relationship between the heating coil resistance and temperature, and find the parameters to use in the Callendar-Van Dusen equation.

6.2.1 Raman calibration of MEMS heater:

A small portion of un-doped silicon wafer is crushed with a mortar and dispersed in an ethanol solution, which is casted on top of the heating coil of the MEMS heating chip. The MEMS chip is then loaded on the TEM heating holder and inserted in a vacuum casing attached to a turbo-molecular pump. The pressure in the casing after 15 minutes pumping time is approximately 5×10^{-6} mbar, low enough to neglect convective heat dissipation trough air. The vacuum casing has a transparent glass window, through which the heating coil can be optically accessed.

The silicon particles, typically 10 μm in size, can be identified with the optical microscope, after which the Sapphire laser (488 nm wavelength) is focused on the sample through a 50x/0.5NA objective, and the Raman spectra acquired. The silicon Stokes line, located approximately at 520 cm^{-1} at room temperature, is fitted with a Lorentzian curve, from which the center of the peak and its Full Width Half Maximum (FWHM) can be extracted. We proceed increasing the current flowing in the heating coil, and thus its temperature, and simultaneously acquire the Raman spectra.

The temperature dependence of the Raman spectra of Crystalline Silicon is quite well established, both in bulk material [4],[3] and in nanoscale devices [2][1], in a broad range of temperature (20 K – 1200 K). Increasing temperature will induce a redshift of the 521 cm^{-1} Stokes line of Silicon, accompanied by a broadening of the peak. In the temperature range 20 K – 1200 K , Raman peak position and can be accurately described by the following equation [1], [5]:

$$\omega(T) = \omega_0 + A\left(1 + \frac{2}{e^x - 1}\right) + B\left(1 + \frac{3}{e^y - 1} + \frac{3}{\left(e^y - 1\right)^2}\right) \tag{6.1}$$

$$x = \frac{hc\omega_{(T=0K)}}{2kT} \qquad y = \frac{hc\omega_{(T=0K)}}{3kT}$$

Where h is the Planck constant, c the velocity of light, k the Boltzmann constant, and $\omega_{(T=0K)} = 525\ \mathrm{cm}^{-1}$ the frequency of the Raman peak at $T = 0\ K$ [4]. The constants , A and B were taken from reference [5], where they were experimentally extrapolated from the Raman spectra of a single crystal Silicon sample: $A = -2.96\ \mathrm{cm}^{-1}$ and $B = -0.174\ \mathrm{cm}^{-1}$. The offset constant $\omega_0 = 526\ \mathrm{cm}^{-1}$, was chosen to match with the peak position of our Raman spectra at room temperature (T= 296 K).

6.2.2 Pyrometer calibration of MEMS heater:

A pyrometer is a remote-sensing thermometer that measures the surface temperature of an object by looking at its (near-) infrared emission, which is temperature dependent according to Planck's law for Black Body radiation. We used a commercially available pyrometer (Sensor Therm, MI16 300C-1300C), which measures the infrared radiation emitted at a wavelength of 1.6 μm. The only parameter that needs to be adjusted in the pyrometer software is the emissivity of the target surface. This parameter is a real number comprised between 0 and 1, where 1 is used for a perfect black body, emitting thermal radiation according to Planck's law, and 0 is used for a perfectly reflecting body, emitting zero thermal radiation. The main two components of our MEMS heater are a 200 nm thick Platinum heating coil, and a 400 nm thick Silicon Nitride supporting membrane. In case of Platinum, emissivity at 1.6 μm wavelength can vary considerably between 0.05 and 0.5, depending on the surface roughness, layer thickness, and on temperature[6]. From literature [7], we find an example of a 500 nm thick, sputtered Platinum film, annealed at 900 K similarly to our platinum coils, that shows an emissivity of 0.1. For Silicon Nitride we also find a wide range of values for emissivity, from 0.05 to almost 1 [6]. Again we find in literature [8] an example of an 800 nm thick SiN/SiO_2 membrane, with an emissivity of 0.125.

As we don't have any direct method to measure the emissivity of our sample, we choose to take the emissivity equal to 0.05, because this is the value that gives the closest temperature reading to the Raman calibration, which we consider to be the most reliable and accurate method. The uncertainty of the sample emissivity can be viewed as a flaw of the Pyrometer calibration, but it does not completely invalidate its reliability.

In fact, if we use a higher emissivity of 0.08 instead of 0.05, the temperature readout decreases approximately 5-7%. This corresponds to an “error” of 50 K when the heater temperature is around 1000 K. Moreover, the pyrometer calibration is experimentally faster, cheaper and easier to perform, as it does not require Raman data analysis, bulky Raman setups, laser safety training and equipment.

Table 6.7 Calibration data for the MEMS heater. Using 5% emissivity for the pyrometer sensor, the match the Raman temperature calibration is within 10 K, except for the highest temperature where the mismatch is considerable. From the Raman calibration we extract the coefficients for the Callendar-Van Dusen equation $a=1\times10^{-6}\pm5\times10^{-6}$, $b=0.423\pm0.008$, $c=161.8\pm2.4$.

Heating coil resistance (Ω)	Dissipated power (mW)	Raman shift (cm^{-1})	Temperature Raman method (K)	Temperature pyrometer with 5% emissivity (K)
289.44	0.002	519.82	296.6	
290.58	0.046	519.73	301.5	
300	0.254	519.25	327	
314	0.572	518.52	364	
325	0.843	517.97	390	
337	1.124	n/a	n/a	
349	1.413	516.81	443	
361.3	1.710	516.22	470	
373.1	2.012	n/a	n/a	n/a below 573 K
384.9	2.323	514.95	523	
408.5	2.966	513.53	582	573
432.1	3.647	n/a	n/a	630
455.66	4.363	510.62	694	684
479.29	5.122	509.11	748	743
550	7.698	504.22	913.6	914
644	12.284	496.93	1137	1248

From the experimental point of view, we use the same vacuum casing used in the Raman calibration, in similar vacuum conditions (5×10^{-6} mbar). We first set the current in the heating coil in order to reach at least 600 K, which is the minimum temperature that our pyrometer can sense. Then we proceed with the alignment of the pyrometer respect to the center of the heating coil: we change x,y,z coordinates of the pyrometer with micrometer screws in order to find the position where the temperature readout is maximum. Finally we perform the actual calibration, setting different currents in the heating coil and reading the corresponding value in the pyrometer.

Table 6.7 summarizes the calibrations obtained with the two different methods, for the Pt heater shown in Chapter 4, Figure 4.3(c).

6.3 Considerations on Silicon Nitride membranes for Heating MEMS:

We collect in this section all the information about Silicon Nitride membranes that might be useful for both experimental considerations and Comsol simulations of our heating MEMS.

In particular we focus on low-stress, amorphous Silicon Nitride, deposited with LPCVD (low pressure chemical vapor deposition), because it is the type we use in our heating MEMS. All the electrical, thermal and mechanical properties of these membranes vary considerably depending on the deposition conditions, such as temperature, pressure and gas composition [9]. Moreover, membrane thickness and temperature are also relevant variables. For this reason, values reported in literature can differ considerably between each other.

6.3.1 Thermal conductivity of SiN

As we already discussed in the section “calibration of MEMS heaters”, most of the generated heat is dissipated through the Silicon Nitride towards the Silicon chip, which acts as a heatsink. Therefore, the in-plane thermal conductivity is the main parameter that will rule temperature distribution across the heater and the amount of power dissipated to the rest of the chip. Less power dissipated means less thermal drift for the TEM holder, and thus better imaging conditions. Thin Silicon Nitride membranes, 50-100 nm thick, display low thermal conductivity, 2.5–3.0 W m^{-1} K^{-1} at room temperature [10][11]. Thicker membranes, 500-1500 nm thick, have a slightly higher thermal conductivity, 4–15 W m^{-1} K^{-1} at room temperature [12]–[14]. Such low values of thermal conductivity make possible to heat the central part of the membrane at over 1100 K, dissipating only a power of 10–15 mW (see the calibration table and the Comsol simulation data).

6.3.2 Mechanical properties of SiN

When fabricating large Silicon Nitride membranes up to several mm in size, it is important to reduce the intrinsic stress in order to avoid cracking and collapse of the membrane itself. For the specific design of out heating MEMS, a small intrinsic tensile stress is preferable because the Silicon Nitride will expand during heating, thus compressing the membrane. The lateral size of the membrane is, in fact, constrained by the silicon frame, which does not expand. Above a certain temperature, approximately 600 K in our heaters, the thermal expansion completely compensates the intrinsic tensile stress of the membrane, which then starts to compress. However, given the elevated stiffness of Silicon Nitride (Young's modulus ~270 GPa [9]), it is energetically convenient for the membrane to bulge out of plane, rather than getting compressed. In fact, we observe an out-of-plane bulging of approximately 10 μm when increasing the temperature from 600 K to 900 K, while no bulging is visible below 600 K.

From a fabrication point of view, low-stress Silicon Nitride is achieved increasing the Silicon to Nitride composition ratio. For Si:N ratio equal to 1, the stress is tensile (~200 MPa), while increasing the ratio to 1.3 gives compressive stress (~ -100MPa)[9]. For comparison, stoichiometric Silicon Nitride has a Si:N ratio of 0.75 and tensile stress of ~1 GPa [9]. EDX compositional analysis on our SiN membranes reveals that they are indeed silicon rich. The average on 10 different 400 nm thick membranes, gives an average Si:N ratio of 1.8±0.4, which is considerably high. This very high ratio could actually be an artifact due to the screening of the N peak in the EDX signal in thick membranes. We thinned one membrane down to 20 nm thickness, and obtained a much more lower Si:N ratio of 1.1 (being only one sample, there is no statistical error).

In accordance to the values reported in literature, we find a low tensile stress of ~120 MPa, measured by laser interferometric technique (Flexus stress meter) on two separate 4-inch Silicon wafers with 100 nm thick SiN film.

The thermal expansion coefficient for Silicon Nitride is $+2.3\times10^{-6}\ K^{-1}$ at room temperature, it increases linearly up to $+3.5\times10^{-6}\ K^{-1}$ at 700 K, and it does not relevantly change as a function to the Si:N ratio [9], [15], [16].

6.3.3 SiN dielectric strength and current transport

As we have seen in the previous section, low-stress, silicon-rich SiN is essential to obtain large, freestanding membranes which can withstand considerable mechanical strain and temperature variations. However, silicon-rich SiN has two major drawbacks on the dielectric properties of the membrane: an increased electrical conductivity and a decreased breakdown field. This variation is understood through a combination of the Poole–Frenkel effect, hopping conduction, which dominate at high electric field, and ohmic conduction at low electric field [17].

According to literature reports, stoichiometric SiN is a good dielectric insulator at room temperature, with a breakdown field of ~10 MV/cm [18]. Instead, Si-rich SiN film can break with a field 5 times smaller, just ~2 MV/cm at T=300 K [19], [20]. As the temperature of SiN membrane increases, this value is further reduced to 1 MV/cm at T= 770 K. Regarding the low electric field regime, below 1 MV/cm, the conduction in SiN is usually ohmic: at room temperature, stoichiometric SiN has a resistivity exceeding 10^{14} Ω·cm [18], while Si-rich SiN ranges from 10^{6} to 10^{11} Ω·cm [21], depending on the amount of Si content.

In order to quantify the dielectric strength and electrical conductivity of our SiN membrane, we run a simple experiment. We evaporate a thin gold film (10 nm thick) on the back side of the SiN window and we deposit a normal Ti/Pt electrode on the top side (for details on fabrication, see Chapter 6.1). Then we apply a linear voltage sweep between the gold in the backside and the electrode on the top side and we measure the current leaking though the SiN membrane (200 nm thick in this case). We highlight that this method completely excludes the contribution of graphitized carbon to the conduction (see Chapter 6.6), and therefore any measured current can only be attributed to the SiN electrical properties.

Figure 6.1 shows the current density leaking through the SiN, as a function of the applied electric field. The current grows linearly up to ~2 MV/cm, indicating ohmic conduction as main electrical transport mechanism. In this low-field regime we can extract the SiN resistivity, equal to 1.6×10^{11} Ω·cm. Beyond E=2 MV/cm, the current grows exponentially following the relationship $J\sim E\cdot\exp[E^{1/2}]$, which is the equation for Poole-Frenkel emission in bulk electrical insulators [17]–[20].

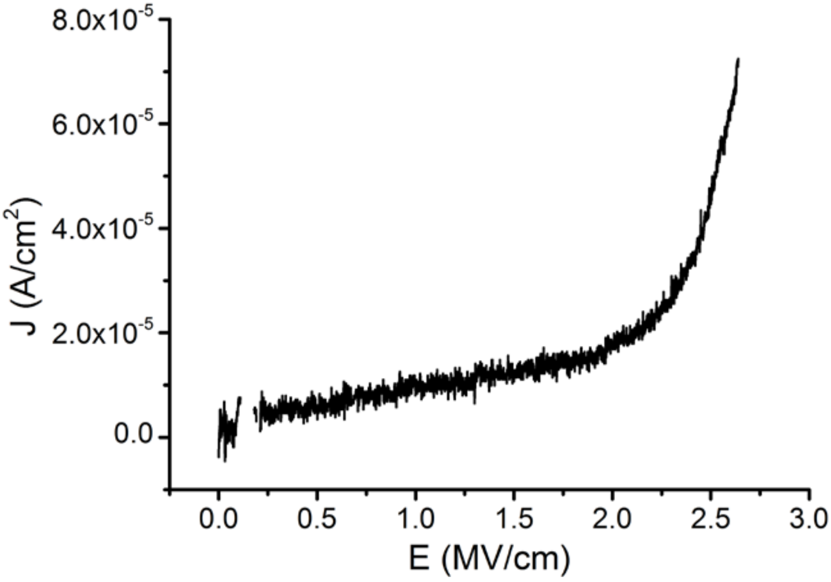

Figure 6.1 Current density through 200 nm SiN membrane, as a function of the applied electric field. Contact area is 100 μm^2. Measured at room temperature.

We did not increase the electrical field beyond 2.6 MV/cm to avoid irreversible breakdown of the sample, which gives us only a lower estimate for the breakdown field of our SiN film.

During our in-situ measurements, the highest electric field we applied is E=0.2 MV/cm (see, for example, Chapter 5 about electron holography), well below the breakdown field. However, we have to consider that future in-situ experiments might need higher electric fields: for example, in order to modulate the carrier density in graphene, an electrostatic gating is required with fields in the order of ±3MV/cm [22].

In addition, we can give a rough estimate of the ohmic contribution of SiN to electrical conduction in our graphene ribbon measurements. Suppose we have two parallel Pt contacts, 30 μm long, separated by a 500 nm SiN gap, which is the worst case scenario we can encounter in our measurements. Based on the extrapolated SiN resistivity $\rho=1.6\times10^{11}\ \Omega\cdot\text{cm}$, the total SiN contribution to resistance would be $R=6.7\times10^{13}\ \Omega$, which is at least 3 orders of magnitude beyond the limits of our electrical setup.

Therefore, we can conclude that the contribution of SiN to electrical conductivity in our in-situ electrical measurement is negligible up to an electric field of 2 MV/cm.

6.4 Finite Element method simulation of MEMS heating devices with Comsol Multiphysics:

Cleanroom fabrication of MEMS heating devices is a very time consuming process. Due to the high number of fabrication steps and the chance of failing some of them, the time needed to obtain the final MEMS chip starting from a bare Silicon wafer is approximately 4-5 weeks (see Chapter 6.1 for the details). During this Phd research, the design of the MEMS heating chip has been changed several times, in order to accommodate different experimental requirements and to correct some flaws discovered during experiments. We soon realized that the adjustments we made to the design were not always correct, which lead to fabrication of faulty heaters and wasted time.

For this reason, we implemented FEM (Finite Element Method) simulations of our MEMS heating devices. With these simulations we can roughly predict the behavior of the heater in terms of maximum achievable temperature, temperature distribution on the surface, power dissipation, SiN membrane stress due to the thermal expansion. Every new MEMS design can be virtually tested within a few minutes, and the major flaws can be corrected. It should remain clear to the reader that these simulations are not intended to calculate exact temperatures and deformations, but to give the experimenter a rough indication on the best way to design a new heating MEMS device.

6.4.1 Description of the FEM model, with simulation settings and parameters:

FEM simulations are performed with commercial software, COMSOL Multiphysics®, version 4.3a. The simulation is performed in three dimensions, to allow mechanical deformation (bulging) of the Silicon Nitride due to thermal and intrinsic stress. The simulation is limited to the Silicon Nitride membrane and the platinum heating coil. The surrounding bulk Silicon frame is not directly included in the simulation and it is considered as special boundary condition. We suppose, in fact, that the Silicon chips acts as large heat sink for the power generated by heating coil, and therefore its temperature raise is negligible. We set two boundary conditions at the edges of the SiN membrane, where they connect with the Silicon frame: fixed temperature (300 K) and fixed spatial constraint. We neglect the convective heat dissipation to the surrounding gas atmosphere, as the heaters are typically used in high-vacuum condition. We include black-body radiation, which we expect to give a considerable contribution to heat dissipation at high temperatures. The size of the SiN membrane can vary depending on the design, while the thickness is fixed at 400 nm. To simplify the geometry of the simulation, the platinum heating coil is defined as a “highly conductive layer” with 180 nm thickness, and positioned on top of the SiN membrane (in the real device the platinum is embedded between two 200 nm thick SiN films).

Regarding the material characteristics, we take the thermal, mechanical and electrical properties of Silicon Nitride from the literature values which are listed in Chapter 6.3. For the Platinum properties, we take the default values which are listed in the material library of Comsol Multiphysics®. Finally we can run the simulation: we fix the voltage at the opposite ends of the heating coil and we look for the stationary solution of the system, which means after the coil and the membrane have reached thermal equilibrium.

6.4.2 Simulation results: temperature distribution

As an example of this simulation method, we report here the results obtained from two different MEMS heater designs. The first design, shown in Figure 6.2(a), corresponds to the one used in the 6 PIN in-situ holder: the heating coil has a “square” shape and there is a flat, empty part at the center of it. The second design, shown in Figure 6.2(c), corresponds to the chip used in the 10 pin in-situ holder and in the 10 pin gas-in-situ holder: the heating coil has a circular shape, with one open side and a flat part in the center. In both cases, the SiN window is 650x650 µm in size and 400 nm thick.

As it can be seen from Figure 6.2(a) and (c), the hottest part is confined within the centermost area of the heater, which is where the graphene is transferred for the in-situ experiments. In Figure 6.2(b) and (d) we can see the temperature profile across the central part of the heater: we notice in particular in Figure 6.2(d) that the temperature “dips” approximately 50°C in the most central part. This “dip” is due to the thermal radiation emitted from the Silicon Nitride, which is related to the emissivity and the temperature of the material (see Chapter 6.2.2).

From the simulations shown in Figure 6.2, we extrapolate that at 800°C approximately 10% of the total dissipated power is due to thermal radiation, while the remaining 90% is dissipated through convective heating to the Silicon frame. In an another simulation run at a maximum temperature of 300°C (not shown here), thermal radiation accounts for only ~2% of the total dissipated power.

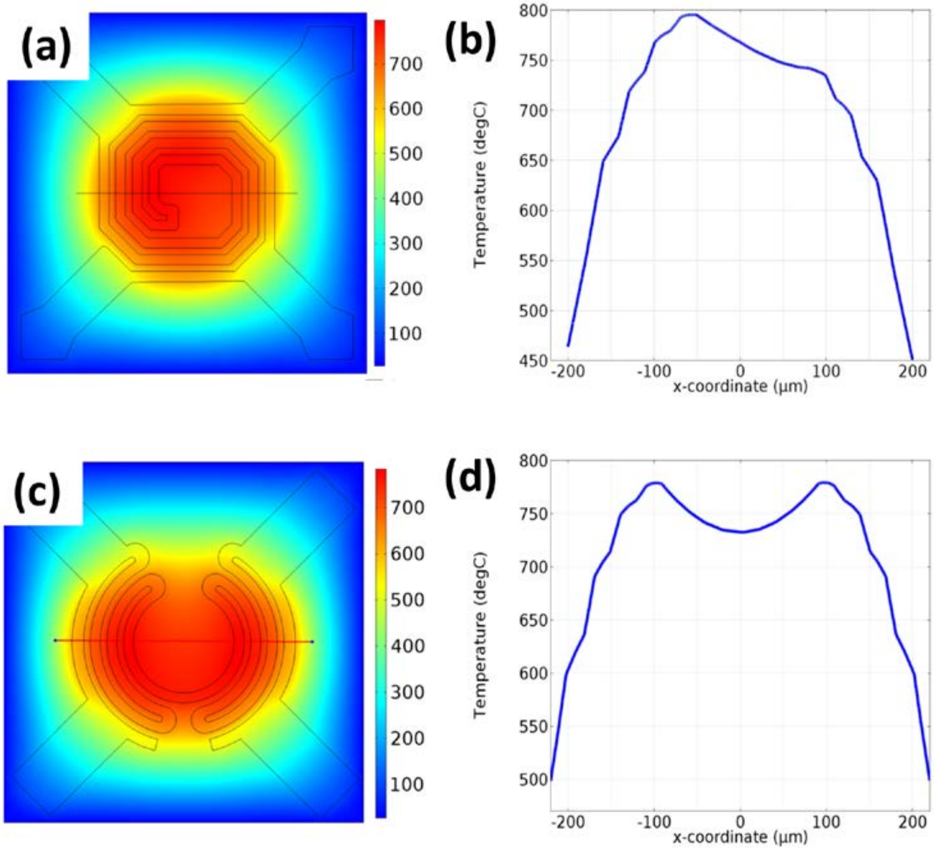

Figure 6.2. FEM simulation of the temperature distribution on the Silicon Nitride membrane. The emissivity of SiN is set at 0.12 and the thermal conductivity at 5 W/m/K. (a)-(b) "square" type of heating coil. The voltage applied is 2.2 V, with a total dissipated power of 14 mW. (c)-(d) "circular" type of heating coil. The voltage applied is 2.3 V, with a total dissipated power of 16 mW. In (a) and (c) we see the top view of the SiN membrane, with the heating coil and a color-map of the temperature distribution. The scale bar is in degrees Celsius. In (b) and (d) the temperature profile across the horizontal line drawn in (a) and (c). Notice that the in the central part, from -100 μm to +100 μm, the temperature is uniform within ± 25°C.

6.4.3 Simulation results: deformation and strain in Silicon Nitride

One of the first obstacles that we encountered during the sculpting of the suspended graphene nanoribbons is the strain generated during the heating of the SiN membrane. In fact, the thermal expansion coefficient of Silicon Nitride is positive (+2.3×10^{-6} K^{-1}, see Chapter 6.3.2), which means that if we cut a long and narrow slit in the membrane, the gap between the long edges is going to be compressed when the temperature increases. Since graphene is suspended between the edges of the slit, such induced strain can interfere with the electrical measurements and, in extreme cases, rupture the graphene itself. This actually limits the maximum slit size that we can cut in the Silicon Nitride membrane.

First we show the experimental results and simulations of a rectangular slit, 30 μm long and 0.3 μm wide, which corresponds to the initial chip design that we manufactured. As a function of temperature, we measure both the gap between the long edges of the slit and the bulging of the membrane. The bulging is measured adjusting the z-position in the microscope stage, to keep the sample always in focus. We remind the reader that the Silicon frame does not expand during the heating, thus the SiN membrane needs to bulge out of plane to compensate for the thermal expansion (see Chapter 6.4.3 for additional considerations on membrane bulging).

Figure 6.3(a) and (b) show the experimental and the simulation results, respectively. In the experimental data we notice a strong non-linearity: from room temperature to 300°C the membrane does not bulge, but there is a strong compression of the SiN slit; above 300°C the behavior is inverted. We observe that the slit compresses by almost 40 nm over the full temperature range.

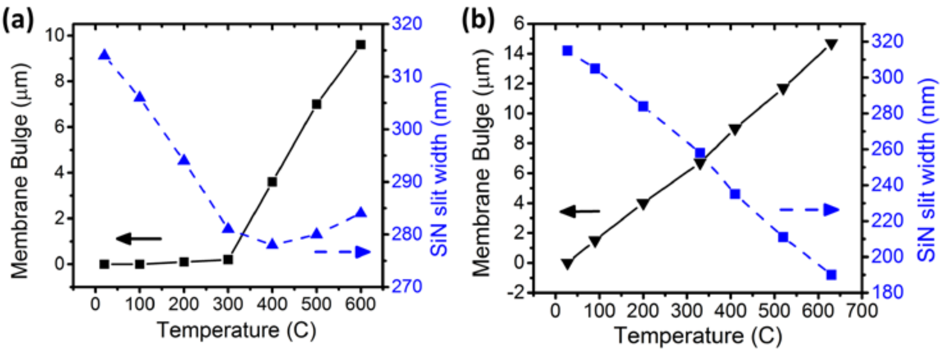

Figure 6.3. SiN membrane out-of-plane bulging (black squares) and compression of a 30 μm long and 314 nm wide slit (blue triangles), cut in the membrane, due to thermal expansion. (a) Experimental results show a strong non-linear behavior. (b) Simulation results predict bulging and slit compression, but fail to mimic the non-linearity. We use a constant thermal expansion coefficient, 2.3×10^{-6} 1/K , Young's modulus 270 GPa, Poisson's ratio 0.27.

The simulation also predicts the bulging of the membrane and the compression of the slit with a comparable magnitude to the experiment, but it completely fails to predict its non-linear behavior. The simulation, in-fact, supposes that SiN is a "linear elastic material" and neglects the intrinsic tensile stress of the membrane. For the reader who may not have access or familiarity with FEM simulations, we can also give a simple rule of thumb to calculate the compression of the slit. It is sufficient to multiply the length of the slit (30 μm) by the thermal expansion coefficient (2.3×10^{-6} K^{-1}) and the temperature change (600°C) to get a 40 nm compression, very close to the actual value.

As a second simulation, we check the design which we used in the final version of the MEMS heating chip. This design has a circular hole with 2 μm diameter, and several other rectangular openings next to it. The diameter of the hole shrinks 4 nm during the heating from room temperature to 873 K. For this simulation we don't report any graph, as the compression is linear with temperature, like the one seen for the rectangular slit. We conclude that the round hole design is preferable over the long, thin slit.

6.5 Considerations about graphene strain

After establishing the dynamics of the SiN thermal expansion, what can we say about graphene strain? The initial graphene strain, immediately after wedging transfer, remains unknown and it is hardly measurable. The smallest strain that can be measured by HRTEM imaging is in the order of 2-3% [23]. The best estimation that we can find in literature is that the initial strain is less than 1% on a local scale, measured from the broadening of the diffraction spots during tilting in CBED* mode [24].

The contribution of SiN thermal expansion to graphene strain can be estimated in the order of -0.2% (compressive) for a hole with 2 μm diameter, when heating from room temperature to 873 K. However, graphene itself has a negative expansion coefficient [25] which is twice as large as the SiN one coefficient (-8×10^{-6} K^{-1}), which compensates for the effect of the SiN expansion, so that the effective strain +0.2% (tensile) at 873 K. A 0.2% tensile strain will induce a maximum 0.6% increase in graphene electrical resistance, according to the Gauge factor reported in literature [26]–[28]. Such change is very small compared to the variation that we actually observe in our samples during heating, which is more likely to be interpreted in terms of thermal generated carriers and phonon scattering (see Chapter 4.3).

6.6 Considerations on electrical resistivity of amorphous carbon

As we already emphasized in Chapter 4, one of the key components of our graphene sculpting experiments is the use of MEMS heaters. Heating up the device at temperatures T>570 K prevents beam-induced carbon deposition, while for T>800 K graphene undergoes a recrystallization process, which heals the lattice defects and

---

* Convergent Beam Electron Diffraction

improves the electrical conductivity. Moreover, we can perform temperature dependent electrical measurements, exploiting the precise temperature calibration of the heater (see Chapter 4.3).

However, as graphene recrystallizes and improves its conductivity at high temperatures, so does amorphous carbon. The heating coil is, in fact, heating up the whole SiN membrane, where there can be a non-negligible amount of organic residues (polymer) from the device fabrication. Upon high-temperature heating, these residues will first undergo a “carbonization” process (loss of H, N, O atoms) and later a “graphitization” process (transformation in graphite). This newly graphitized carbon provides a parallel path for electrical conduction, acting as a parasitic resistance. In the worst cases, the magnitude of this parasitic resistance can be equal or even smaller than the resistance of the graphene nanoribbon we are trying to characterize (mostly in the range from 100 kΩ to 1 MΩ). Therefore it is important to consider this effect when designing graphene nanoribbon experiments, in order to minimize its magnitude.

In the following two sub-chapters we are going to give a brief literature overview on the topic, followed by an experimental characterization of the amorphous carbon conductivity in our MEMS heaters.

6.6.1 Amorphous carbon electrical conductivity, carbonization and graphitization: brief literature overview.

Pyrolytic graphitization is the process during which amorphous carbon transforms into one of its crystalline allotropes, graphite, through high temperature annealing in vacuum or inert atmosphere [30]. This topic has been thoroughly investigated in the last 60 years [29], even long before the first single-layer graphene was isolated [31], as it was of great interest for the manufacturing of carbon steels.

As we can see in Figure 6.4, the ordering, or crystallinity, of carbon structure improves as annealing temperature increases. Although the complete graphite transformation is achieved in the 2000 – 3000 K temperature range, the formation of small graphitic islands already starts at 900 K – 1100 K [29]. This high-temperature transformation is also compatible with the recrystallization of graphene that we observe during our Joule heating experiments on graphene nanoribbons (Chapter 4.3).

Here we would actually like to consider the transformation that organic residues (mostly PMMA polymer) undergo in a lower temperature range, between 600 K and 900 K. Starting from 600 K, the volatile atoms, such as hydrogen, nitrogen and oxygen, evaporate, leaving only an amorphous carbon matrix behind; this process is called “carbonization” [32]. As the hydrogen atoms are removed, the carbon bonds become more and more unsaturated, increasing the amount of sp^2 bonding sites. When the temperature has reached 900 K, approximately 70% of the total amount of C-C bonds are sp^2 [32].

In general, the temperature dependence of the electrical conductivity in amorphous carbon follows the equation [32]:

$$\sigma = \sigma_0 \exp\{-(T_n/T)^n\} \tag{6.2}$$

The coefficient n in the exponent changes depending on the main conduction mechanism: $n = 1$ indicates thermal activation of the states with energy $E = k_B T_n$, away from the Fermi energy; $n < 1$ indicates variable range hopping in localized states around the Fermi energy. In particular, $n = 1/4$ and $n = 1/3$ are the classic values for three-dimensional and two-dimensional systems, respectively [33]. The value of σ_0 strongly depends on the maximum annealing temperature that the amorphous carbon has reached.

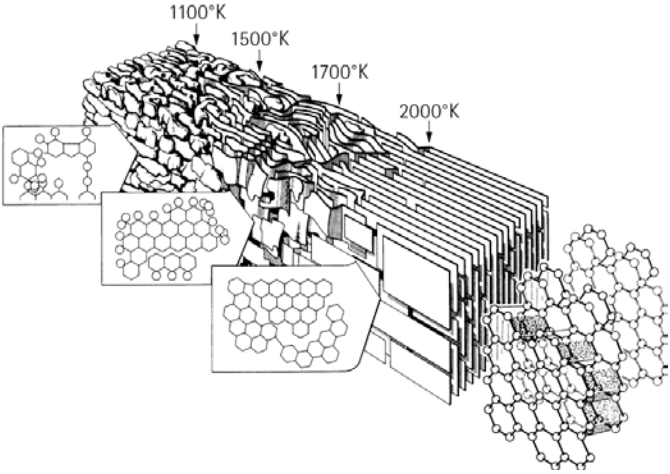

Figure 6.4 Schematic illustration of carbon graphitization, as a function of temperature. Small graphitic platelets form already at 1100 K. Adapted from [29].

6.6.2 Experimental characterization of a-C graphitization

We perform a series of tests, in order to isolate the sources of carbon contamination on the SiN membrane, and to characterize the temperature dependence of this “graphitization” process.

We start with a MEMS heater with two platinum electrodes, 1 μm apart and 1 μm wide, without any graphene on them. We thoroughly clean the sample from carbon contaminants with oxygen plasma. In this case, the low-bias, room temperature resistance between the electrodes is greater than 200 GΩ (upper limit of our electrical setup). When the SiN is heated at 920 K in high-vacuum, the resistance slightly drops to

10 GΩ, due to SiN increased electrical conductivity (see Chapter 6.3.3), but it promptly recovers the original value when cooled again to room temperature. The blue triangles in Figure 6.5(a) summarize the temperature dependence of the electrical conductance, which does not show hysteresis if the heating cycle is repeated. With this first test we establish that the sample is mostly carbon-free, and we quantify the contribution from SiN electrical conductivity at very high temperatures.

For the second test, we dip the same MEMS heater in Ethyl Acetate for a few seconds, then let the chip dry in air for a couple of minutes. We repeat the heating experiment in high-vacuum, and leave the chip at 920 K for 10 minutes. After this time lapse, we find that the resistance between the electrodes at 920 K has dropped to 100 MΩ. Upon cooling to room temperature, the resistance does not completely recover the initial values, stopping just above 100 GΩ. The temperature dependence is indicated by the black squares in Figure 6.5(a). Hysteresis data is not available in this case.

Finally, we clean the sample with oxygen plasma, we check that the initial high resistance has been recovered, and then we repeat the test once again, this time dipping the sample in a Cellulose Acetate Butyrate polymer solution (the same used in the graphene wedging transfer). After the polymer has dried, we wash it away in ethyl acetate for 15 minutes. After heating at 920 K the resistance has considerably dropped to 1 MΩ. The temperature dependence is indicated by the red circles in Figure 6.5(a). We also measure the hysteresis of the process during the first heating cycle, shown in Figure 6.5(b): for each point, we wait 1 minute at the chosen temperature, during which the resistance has time to roughly stabilize.

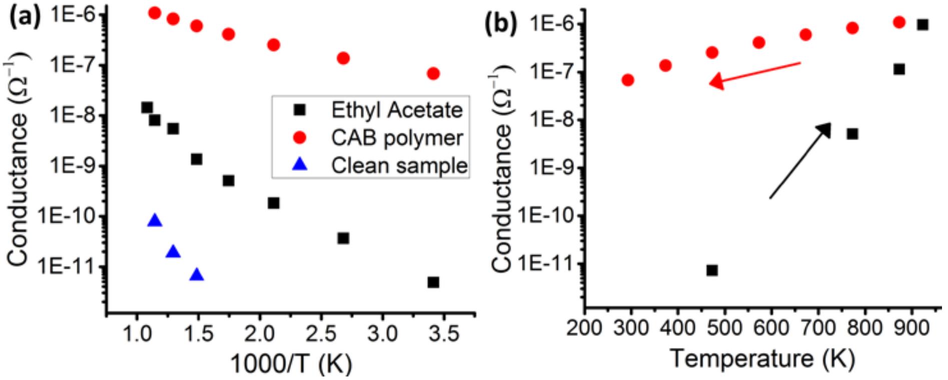

Figure 6.5 (a) Arrhenius plot of the electrical conductance measured between two platinum electrodes on top of the SiN membrane, for three different conditions (see main text). (b) Hysteresis cycle of conductance for a sample treated with CAB polymer.

From this series of experiments we make some brief conclusions:

1) The electrical conductivity of amorphous carbon is greatly enhanced above ~550 K and it rapidly increases with temperature.
2) Even a simple dip in an organic solvent, such as ethyl acetate, leaves a very small amount of hydrocarbons on the SiN surface, which becomes slightly conducting upon heating.
3) Coating the SiN surface with a polymer, such as CAB, leaves a considerable amount of hydrocarbons, even after washing with ethyl acetate.
4) The temperature dependence of the conductive carbon, after the heating, suggests a typical temperature activated behavior, as expected from literature. The dependence follows equation (6.2), with the exponent $n = 0.4 \pm 0.1$ in the case of ethyl acetate (compatible with $n = 1/3$ of variable range hopping in the two-dimensional regime), and $n = 0.24 \pm 0.03$ for the CAB polymer (compatible with $n = 1/4$ of the three-dimensional regime)
5) The hysteresis behavior upon repeated heating cycles reveals that the phenomenon is not related the intrinsic conductivity of SiN, but rather to a gradual physical modification of the amorphous carbon coating.

6.7 Graphene Wedging transfer technique

As we have seen in Chapter 4, our experimental design requires transferring graphene on top of the platinum electrodes. Here we describe the graphene “wedging” transfer technique, which we adapted from the work of G. Schneider et al. [34]. We repeat the description of graphene exfoliation part which we already gave in the main text, for completeness.

We start with a silicon substrate, covered with 285 nm SiO_2 thermally grown oxide. The substrate is cleaned with oxygen plasma to remove organic contaminants and to increase the hydrophilicity, which is required for the best graphene adhesion. We manually exfoliate natural graphite with blue Nitto tape on top of the SiO_2 surface, and then identify the graphene flakes through optical microscopy. After the desired flake has been chosen, the position of the flake is roughly marked on the substrate with a permanent ink marker, visible by naked eye. Now we dip the entire substrate, with the graphene, in a beaker with a Cellulose Acetate Butyrate solution (~30 mg/mL in ethyl acetate) for approximately 5 seconds. The substrate is then removed from the solution and the solvent evaporates in air, leaving a ~1µm thick, transparent polymer coating on top. The relative humidity during this step must be around 50-60%. If the solvent evaporates in a very humid environment, water vapor is trapped in the polymer, which then becomes opaque and foggy. Again, we look for the target graphene flake, with the help of the ink marker that we previously made, and we check in the optical microscope that the polymer coating did not considerably alter the flake. It may occasionally happen that the flake rolls up during the polymer bath, because of poor adhesion with the substrate. To make sure that we don’t lose the position of the flake in the following step, we mark it with four small ink dots, drawn by hand on top of the polymer layer.

At this point we prepare the target substrate: we take a modified Petri dish, the MEMS chip with the electrodes and we clean them in oxygen plasma. We use double sided carbon tape to fix the MEMS chip in the center of the Petri dish, so that it doesn’t move during the transfer. We fill the Petri dish with de-ionized water, enough to cover also the MEMS chip. Next step is the most difficult of the whole process: with the sharp tip of metallic tweezers, we scratch the polymer from the edges of the SiO_2 origin substrate; then we slide the substrate in the Petri dish filled with water, with 30° incidence angle respect to the water surface. Starting from the scratched polymer edge, the capillary force attracts water between the polymer layer, which is hydrophobic, and the SiO_2, which is hydrophilic. The polymer gradually detaches from the substrates and floats on water, while the substrate itself sinks at the bottom of the Petri dish. During this lift-off process, graphene, which is also hydrophobic [35], remains attached to the polymer layer. It may require several attempts to successfully separate the polymer from substrate, especially if the substrate has glue residues from the Nitto tape (which might happen if the tape was pressed too much on the surface during the graphene exfoliation).

The Petri dish with the floating polymer is positioned under the lens of the optical microscope, where the original flake position is recovered thanks to the ink markers; the optical contrast of the flake is, in fact, extremely poor when looked through the floating transparent polymer. A micromanipulator is used to move the polymer on the water surface, to align the graphene flake with the target destination on the MEMS chip. The water is drained with a syringe pump, while monitoring the alignment with the microscope, until the polymer lands on the MEMS chip. Residual water is absorbed with a paper tissue and the chip dries in air for at least 12 hours. Finally, the polymer is carefully dissolved in abundant ethyl acetate and the chip dried with nitrogen gun. The chip is now ready for imaging in TEM or for further cleanroom processing.

As a final remark, we highlight that the whole transfer procedure, from exfoliation until final water drying, needs to be performed within a few hours from the oxygen plasma cleaning, while the surfaces are still hydrophilic.

6.8 Improvement of metal-graphene contact resistance upon thermal annealing

In order to make electrical contact with graphene, one or more metal lines have to come in contact with it. Due to the difference in the work functions and interaction strength between graphene and the metal, contact resistance develops across the junction [36]–[38], which is added in series to the “intrinsic” graphene device resistance. This contact resistance is largely influenced by the type of metal and by the device fabrication sequence.

The contact fabrication procedure which is mostly found in literature is the following: first deposit graphene, then evaporate metal contacts on top of it, and finally anneal the sample. The annealing step is crucial to remove polymer contamination on graphene surface (deposited during electron beam patterning of electrodes) and to reduce the graphene-metal contact resistance. In all our samples, the fabrication sequence is inverted: first we deposit the metal contacts, then graphene is transferred on top of them, and finally annealed. Here we show that this inverted sequence delivers similar results to the conventional sequence; moreover, in the inverted sequence graphene is not exposed to the PMMA/metal evaporation step, which results in a much cleaner surface.

We tested the validity of this assumption with our in-situ electrical setup, performing the annealing with the integrated MEMS heater in the vacuum of the TEM (~10^{-6} mbar). For this purpose it is preferable to use a two-probe configuration, instead of the four-probe. Before the annealing, in fact, the two extra sensing connection of the four-probe configuration would suffer from poor contact with graphene, giving wrong voltage readings. The values obtained with two-probe configuration pose an upper limit for the graphene-metal contact resistance, which is more than sufficient to prove the annealing effect. The measuring protocol is the following: anneal the sample at a given temperature for 1 minute and then measure resistance; if the resistance does not considerably change, increase the temperature and repeat; otherwise keep the same temperature and measure with 1 minute interval.

We report the results from a representative monolayer graphene sample, transferred on top of Pt electrodes with wedging transfer technique (see Chapter 6.7); the same behavior has been observed in all the samples fabricated with this method (more than 40) with small temperature annealing variations. Figure 6.6 shows the dependence of the two-probe device resistance as a function of the annealing temperature: the initial resistance is in the GΩ range, which can be explained by the fact that graphene has a very poor physical adhesion on the metal immediately after the transfer. At T=423 K we stopped increasing the temperature and we monitored the resistance for 25 minutes, as shown in the inset of Figure 6.6. This slow process can be mostly attributed to the improved mechanical contact between the metal and graphene, to the evaporation of residual water molecules and other volatile contaminants. In another sample (not shown here), annealing at T=473 K achieves the same results in only 3 minutes.

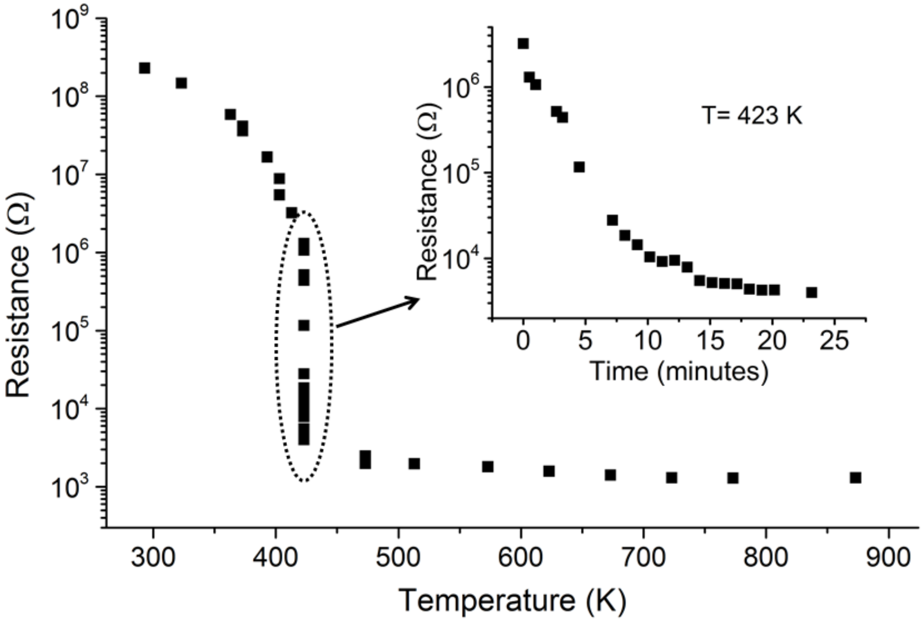

Figure 6.6: In-situ electrical measurements of the graphene-metal contact resistance as a function of the annealing temperature, on a single representative sample. Each data point in the graph corresponds to 1 minute annealing time. At T=423 K there is a large resistance drop, whose variation in time is shown in the inset. The duration of the whole annealing, from T=300 K to T= 870 K is 42 minutes.

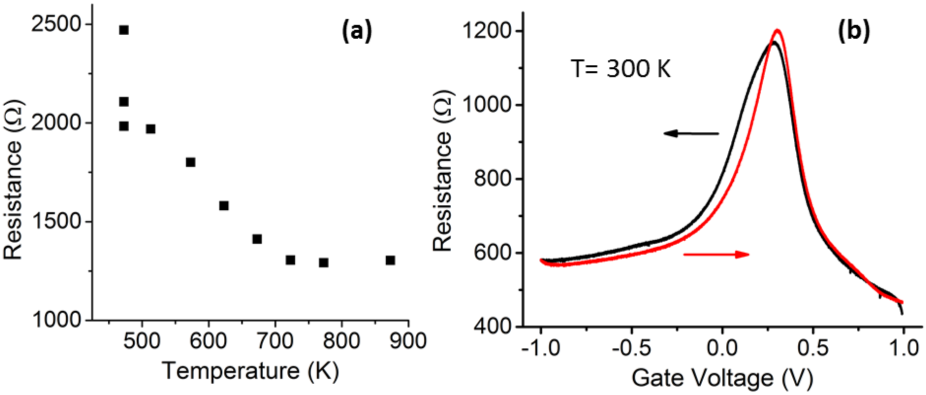

Figure 6.7 (a) Detail of Figure 6.6 for 470 K<T<870 K. Each point corresponds to 1 minute annealing time. (b) Liquid gating of the same sample show in Figure 6.6, after the thermal annealing. The maximum resistance is R=1200 Ω, in correspondence of the charge neutrality point.

Figure 6.7(a) shows a detail of the evolution between T=470 K and T= 870 K, where we expect the formation of chemical bonds between graphene and metal. Annealing beyond T= 670 K brings no additional benefit to the resistance. Considering the 3.5 μm wide platinum electrodes (this graphene flake is actually 10 μm wide, much more than the electrodes), and the minimum achieved resistance R= 1290 Ω, we can extract an upper limit for the contact resistance R_c= 4515 Ω·μm. Please note that the improvement of contact resistance is permanent, so that it will not increase again upon cooling.

This value is considerably higher than what can be achieved with Pd [36] (R_c~600Ω·μm measured at room temperature and charge neutrality point). This is because Pd, together with Co and Ni, have strong interaction with graphene, and can form chemical bonds with it. Instead, metals such as Ag, Au, Cu, Al and Pt, are weakly interacting with graphene [38]. For the particular case of graphene CVD grown on crystalline Pt (111 orientation), it has been shown that the interaction with the metal is so weak that graphene is almost entirely electronically decoupled from it [39]. Therefore, Ni, Co and Pd would be the best materials for fabrication of low-resistance electrical contacts.

However, Ni and Co cannot be used in our experiments because they are ferromagnetic (in a TEM, the magnetic field at the sample can be as high as 2 Tesla [40]). We could have used Pd, but our fabrication process includes one cleaning step in nitric acid (HNO_3), which can dissolve Pd quite rapidly. In practice, we chose Pt because it is resistant to most acids and it has the highest melting temperature of all these metals, so that it does not melt or diffuse during in-situ heating. For future experiments, we suggest finding an alternative to nitric acid cleaning and replace Pt with Pd for the metal contacts.

6.9 Four-probe measurements of contact resistance: temperature dependence

After the graphene-Pt contact resistance has been improved by thermal annealing, we can look at its temperature dependence. For this purpose, the four-probe configuration is essential if we want to eliminate the contribution from the segment of graphene not covered by the metal electrodes.

Figure 6.8 shows the measured values for a bilayer sample. As the temperature increases, we observe a small decrease of contact resistance, quantifiable as -0.1 ± 0.04 Ω/K. The same trend has been observed also in another bilayer sample. However, the large error on the measurement and the limited amount of samples with four-probe contacts make this result not conclusive.

If this trend would be confirmed, it could be explained compatible by the formation of a Schottky barrier between the metal and the graphene, similarly to metal-semiconductor junction. This is actually against what it typically observed in literature, as graphene should be gap-less and form a simple p-n junction with the metal, without any Schottky barrier [36]. At the moment, we do not have any plausible explanation for this behavior. What we can safely assume, is that the graphene-metal contact resistance is constant within ±100 Ω over the whole temperature range, from 300 K to 873K.

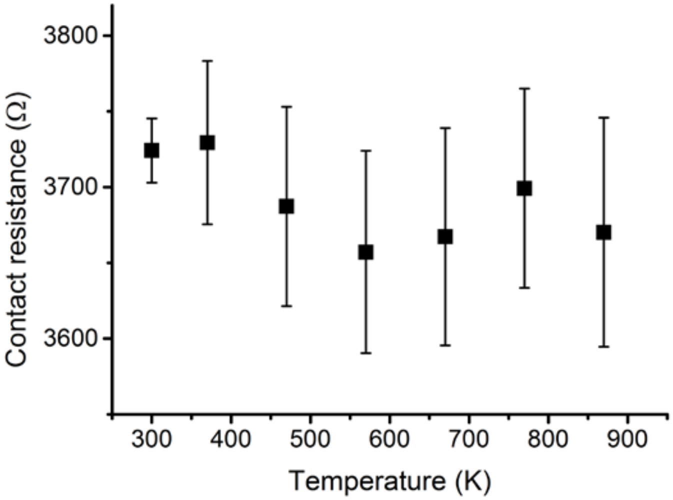

Figure 6.8 Temperature dependence of the contact resistance due to the graphene-Pt interface, measured with the 10-pin holder and 4-probe sensing.

6.10 Graphene liquid gating

One of the main limitations of our in-situ electrical measurements is the lack of an electrostatic gate to shift the Fermi level. We tried to solve this problem using liquid gating, with ex-situ measurements.

Liquid gating consists in using an ionic liquid, such as a KCl solution in water, as dielectric material for field effect electrostatic gating [41]. The electrical double layer (EDL) which is formed at the interface between the liquid and graphene gives the geometrical capacitance of the device, estimated in the order of tens of $\mu F/cm^2$. Its actual value is hard to determine, given the fact that the thickness of the EDL is not known a-priori. Moreover, graphene has a quantum capacitance which is in the same order of magnitude of the EDL one, and thus it has to be considered when calculating the total device capacitance [42]. In addition, the value of quantum capacitance varies strongly as a function of the Fermi energy in graphene, and on the number of graphene layers.

Given the uncertainty on both the quantum and the EDL capacitance, an independent back-gate with very well-known capacitance is usually employed for calibration. However, our devices do not possess any back gate, and we are limited to use the liquid gating as a proof of principle. Without an estimate for its capacitance, we cannot extract the induced charge density in graphene, but we can locate the charge neutrality point and the value of minimum conductivity.

We applied the liquid gating on the same sample used in Chapter 6.8. We used a 20 mM KCl solution in water, with an AgCl reference electrode. The results are visible in Figure 6.7(b): we plot the device resistance as a function of gate voltage, in the ±1 V range, measured at room temperature. First of all, we notice that the charge neutrality point is shifted towards a positive gate voltage, which means that the KCl solution is inducing p-type doping of graphene [43]. Secondly, the curve is asymmetric, with the negative gate voltage resistance higher than the positive side. This is because the portion of graphene on top of the Pt contacts is heavily p-doped [37]: depending on the gate voltage, a p-n or p-p junction is formed at the junction between freestanding and metal supported graphene; the p-p junction is less resistive than the p-n junction, which means that the contact resistance is lower when graphene is p-doped, and higher when n-doped.

Finally, the most important feature we want to highlight is that the maximum resistance, in correspondence of the charge neutrality point, is $R\sim1200\ \Omega$. This is the same value we measure inside the TEM vacuum, after thermal annealing, and it is a strong indication that our devices, during the in-situ experiments in TEM, have very little charged impurities on them.

We tried to implement liquid gating on graphene nanoribbons, instead of using large area flakes, but they cannot withstand the surface tension generated by the liquid, and break as soon as they come in contact with it.

6.11 Impurity analysis on graphene with EDX

In our experiments, as in other literature works [44], one of the most relevant practical problems is the presence of impurities on graphene, both polymeric and metallic. The polymers we typically come across are made of hydrocarbon chains, which, upon annealing in vacuum, undergo a “carbonization” process (see Chapter 6.6). Once this has happened, the polymer forms a thin layer of carbon which strongly adheres to graphene surface, and it becomes very difficult to remove. Therefore it is very important to understand why polymers are attracted to graphene in the first place, and why solvents, such as acetone, cannot completely remove them.

In order to get a bit more insight into the polymer and metal contamination issue, we performed EDX elemental analysis on our graphene samples. Figure 6.9 shows a STEM image of a 300 nm wide graphene ribbon, with several polymer residues after PMMA coating has been dissolved in acetone; the polymer residues appear brighter respect to the graphene, due to increased mass contrast. Metal contamination also appears brighter, because of higher Z-contrast. We acquire EDX spectra (Oxford Instruments X-MaxN 100TLE) in several points of the ribbon, and notice a correlation between the presence of polymer residues and metallic contamination. In this case we find the presence of Ca, Fe, P, Al and Si. Table 6.8 reports the quantitative composition analysis for all the points in Figure 6.9. EDX analysis performed on several other samples, not shown here, confirms the presence of Ca, most likely originating from water, and occasionally shows the presence of Cl and Na, possibly originating from human skin during handling of tweezers without gloves. The origin of Fe, Al, Si and P remains unclear at the moment (we remind the reader that we are always using exfoliated graphene, not CVD graphene).

From these simple observations we cannot conclude whether the metal ions are causing the agglomeration of polymer or, vice versa, if the polymer is trapping metal ions. Nevertheless we think that this correlation is quite peculiar, and it would be interesting to explore it in more depth in future experiments. One possible idea is to sputter a few atoms of metal on graphene, coat with PMMA and check if the metal catalyzes its adhesion on the surface.

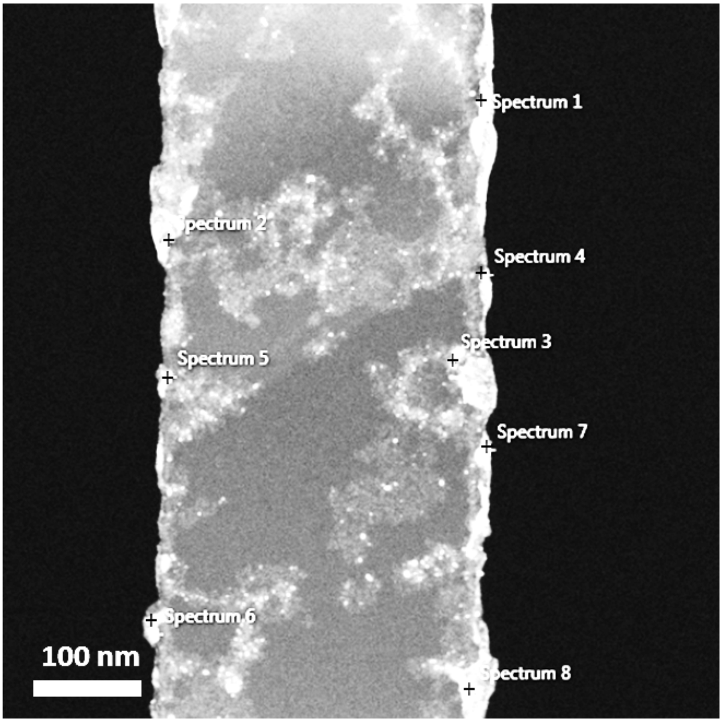

Figure 6.9 STEM image of a graphene ribbon, 300 nm wide, after PMMA coating and acetone cleaning. We acquired EDX spectra in correspondence of the points indicated in the figure, from 1 to 8, whose results are reported in Table 6.8.

Table 6.8 EDX quantitative composition analysis from the positions in Figure 6.9, in weight percentage. The total of all analyzed elements is calculated to be 100%.

Spectrum number	C	O	Al	Si	P	Ca	Fe
1	87.81	3.31	0.23	5.04	1.93	0.34	1.34
2	89	1.25	0.01	6.47	2.51	0.77	0
3	23.33	8.81	0.24	7.91	11.1	2.33	46.27
4	95.59	0.12	0	2.39	1.21	0.12	0.56
5	82.58	6.5	0.35	8.38	0.47	1.64	0.07
6	92.89	0	0	5.92	0	0	1.19
7	19.11	7.01	0.76	28.07	2.66	0.33	42.06
8	21.19	21.79	5.74	7.71	11.07	2.3	30.19

6.12 In-situ TEM 10 pin holder design

Figure 6.10 contains the images of the ten-pin in-situ TEM holder. Compared to the six-pin holder, it has a circular Pt heating coil, designed such that there is no overlap between the coil and the Pt contacts for graphene measurements. It has been used in some of our graphene samples to perform 4-probe measurements.

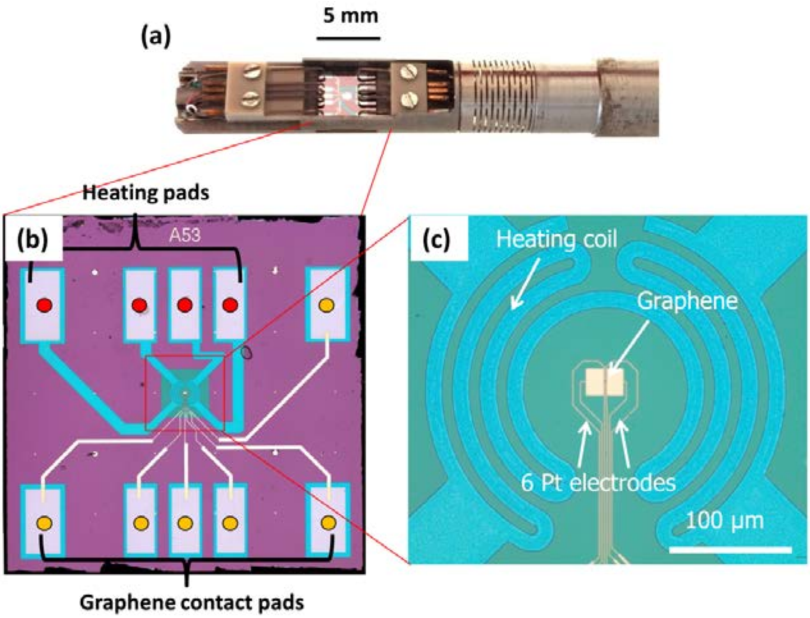

Figure 6.10 (a) Tip of the 10 pin in-situ TEM holder. (b) Design of the MEMS heating chip, 4.8 mm in size. (c) Zoom of the SiN membrane with a circular heating coil.

6.13 Electrical setup

In this last part of the chapter, we describe the details of the electrical setup, which we already roughly explained in Chapter 4, Figure 4.2. We also address the topic of electrical noise, with some solutions that we adopted to reduce it.

6.13.1 Description of electrical setup

Figure 6.11 shows the schematics of our electrical setup. Starting from the bottom of the image, we see the Matrix module, which is used to collect and split the signals coming from the sample. A copper-shielded cable, containing ten wires, is connected on the back side of the Matrix module (not shown here), and it brings the signals from the Matrix module to the TEM holder. On the front side of the Matrix module we can plug up to twenty-four connections, although only ten can be used with the copper-shielded cable. Four of these connections are used for the heating box (indicated with a small flame in the figure). In the two-probe measurement configuration, the voltage source is the Digital Analog Converter (DAC) of the ADwin-Gold, and the current meter is contained in the *current amplifier*. The current amplifier converts the current into a voltage, with four selectable amplifications (from 10^6 to 10^9 V/A), which is sent to the ADC of the ADwin-Gold through a low-pass filter. The input impedance of the current amplifier depends on the amplification factor in a non-trivial way (10^6 V/A =3 kΩ impedance, 10^7 V/A = 10 kΩ, 10^8 V/A=100 kΩ, 10^9 V/A= 1MΩ).

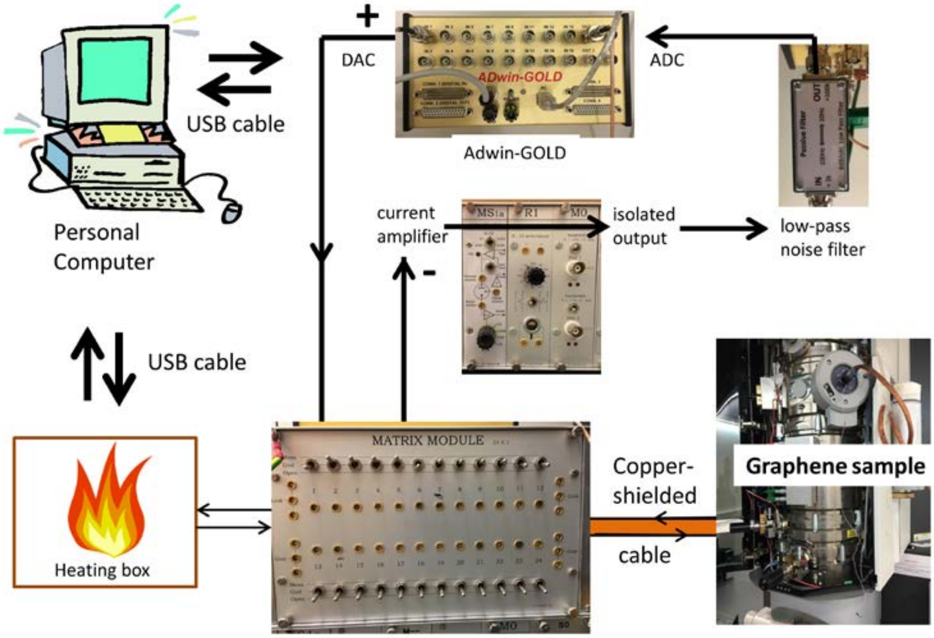

Figure 6.11 Schematic of the electrical setup. See main text for description.

The proper input impedance has been subtracted in all measurements, so that only the real graphene device resistance remains. Regarding the specifications of the ADwin-Gold, it has two 16 bit DAC and two 16 bit ADC, with maximum 200 kHz sampling frequency. The DAC can output in the ±10 V range (±25 mA current), while the ADC has an adjustable gain, which we set to obtain ±5 V measurement range.

Finally, a Personal Computer is connected via two separate USB cables to the Adwin-Gold and the heating box, and it contains two separate software (wrote in Labview), to control them. It is a good habit to synchronize the clock of this PC with the one of the TEM computer, to obtain the same time-stamp on both the images and the electrical measurements. The Adwin-Gold, the Personal Computer and the heating box are powered with AC/DC transformers, which will inject 50 Hz noise into the system (see next section). The current amplifier is powered with lead battery, thus low noise.

Regarding the limitations of the electrical setup in this configuration, the maximum output voltage is given by the DAC (±10 V), and the measurable current is limited by the saturation of the current amplifier, which happens at ±3.2 μA, with the smallest amplification (10^6 V/A). To measure higher currents, which we occasionally used for direct Joule-heating of graphene, we have to modify the setup in the following way (not shown in the figure): we create a voltage divider, where the first resistance is given by the graphene sample, and the second resistance has a fixed, known value (i.e. 10 kΩ); then we use a volt-meter to measure voltage between the two resistances, and extract the value of the first resistance. There were also some occasions in which we were interested in voltages higher than ±10 V, for example while testing the dielectric strength of SiN (see Chapter 6.3.3), or during the in-situ holography experiments (see Chapter 5). In that case we use a different voltage source (not shown here) which has ±90 V output range, but with a maximum 1μA current limit.

Going at the opposite end of the measurement scale, the minimum measurable current is mainly limited by the electrical noise of the setup, which we are going to discuss in the next section.

6.13.2 Considerations about electrical noise

Given the importance of electrical measurements in this work, we dedicate a small section to the analysis of electrical noise, and possible strategies to minimize it.

The first step is the identification of electrical noise sources in our setup. In order to do so, we use a digital oscilloscope (Rigol, model DS1102E, 2 channels, 100 MHz bandwidth) and the signal readout from the ADWin Gold. Using a BNC T-connector, we split the signal going into the input channel of the ADWin Gold (330 kΩ input impedance), and connect the extra path to the high-impedance input of the oscilloscope (1 MΩ input impedance), so that we can monitor the amplitude and frequency of the noise spectrum. As the two input impedances have comparable values, the oscilloscope cannot be considered as an “ideal” monitoring device, and the signal is influenced by its presence in the electrical circuit. Nevertheless, we can get qualitative information about the noise frequency and amplitude.

Before analyzing the possible noise sources and frequencies, we note that each one of the 24 channels in the Matrix box has a 100 pF capacitor connected to ground, which works as a low-pass filter: for a 50 Ω load, the cutoff frequency is around 30 MHz. These capacitors are welded in the circuit, and are present in all measurements.

Without applying any additional filter or software averaging, the noise spectrum is dominated by the 50 Hz and its harmonics, corresponding to the power line frequency. Additional noise is observed in the 10-100 kHz range, present only when the TEM holder is inserted in the microscope, most likely generated by the switches of the magnetic coils.

Considering the 50 Hz noise, we briefly list the sources in our setup:

1) The ADWin Gold power supply (12 Volt transformer)
2) The Personal Computer, used to run measurement software, connected through USB cable to the ADwin and the heating box
3) The heating box power supply (24 Volt transformer)
4) The CompuStage of the microscope, which is the part that is used to move the holder in x,y,z direction, and it is in direct contact with the TEM holder.

The first three elements are the easiest to understand: a power supply converts the 50Hz, 220 Volt AC current into a DC voltage which is used to power those devices; depending on the quality of the transformer, some 50 Hz component can be transferred to the circuit. The fourth and last point needs a longer explanation, which we try to summarize here. In a normal FEI microscope, the CompusStage is connected to a 2 Volt voltage source, so that if the holder touches the objective lens of the microscope (which is grounded), a voltage drop is detected and the “pole-touch” alarm appears. However, our custom-designed TEM holders are always connected to ground through the copper shielded cable, which contains the wires carrying the signal to the matrix box. This implies that, once the TEM holder is inserted in the CompusStage, a fake “pole-touch” alarm is detected, and the system locks the x,y,z stage movements. To solve this issue, we bypass the “pole-touch” protection mechanism, unplugging the 2 Volt source from the CompusStage, which remains floating, not connected to any other metallic part.

We warn the reader who might be interested in replicating this method, that you remove the protection at your own risk, and that tilting the holder is not advisable when the protection is removed. Also, always remember to re-enable the protection when the experiment is finished, as the next user might not be aware of it.

The electrically floating CompuStage now acts as an antenna, capturing all frequencies coming from the nearby electronic devices. This noise is clearly visible from the oscilloscope, and it is well transmitted to the TEM holder. The most effective solution is to ground the whole CompuStage, for example connecting it to the copper shield of the holder cable (also grounded).

Now that we identified the main noise sources, we list the methods we used to minimize their magnitude in our experiments:

1) Application of a low-pass, RC filter, with 100 Hz cutoff frequency, directly at the input channel of the ADWin Gold.
2) Application of two ferrite cores on the BNC cables connecting the ADwin to the matrix box and the current amplifier. They filter very effectively all frequencies above 10 MHz.
3) Connecting to ground all possible components of the setup, including the CompuStage. Avoid creating ground loops with redundant wiring. Check if the ground you are using is “clean” from noise before connecting it. The Faraday cage of our FEI Titan Cubed is not a good grounding option.
4) Signal averaging through software, which is very effective against white noise. The average is performed directly inside the ADWin: 64 samples are acquired with 10 kHz sampling frequency, averaged by the microprocessor of the ADWin, and sent back to the computer. With these settings, the highest data recording rate is approx. 150 Hz.
5) Use only metal shielded cables. In particular, the cable connecting the Matrix module to the TEM holder is shielded with a copper sleeve and an additional plastic sleeve as the outmost layer. This plastic sleeve is very important, because it protects the cable from touching other metallic objects, which might inject noise.

The combination of all the aforementioned solutions delivers a considerable noise reduction. For example, the V_{pp} noise (peak-to-peak) measured at the input channel of the ADwin, without any filter, is typically in the 10-15 mV range, regardless of the amplification factor of the current amplifier (which means that the noise is not originating from the sample, but from the bad grounding and shielding of cables outside the TEM). This value can be reduced to 2 mV just by grounding the CompuStage, which is the most relevant noise source. Adding all the remaining filters, both hardware and software, a minimum V_{pp} noise value of 0.7 mV can be achieved. If the amplification is set to 10^6 V/A, this corresponds to a current noise of 0.7 nA (peak to peak value), regardless of the graphene sample resistance. With the highest amplification, 10^9 V/A, thermal noise (Johnson–Nyquist noise) also contributes: for a 10 MΩ resistor at room temperature and 100 Hz bandwidth, the combined noise is approx. 1.3 pA (peak to peak value).

References

[1] G. Viera, S. Huet, and L. Boufendi, “Crystal size and temperature measurements in nanostructured silicon using Raman spectroscopy,” *J. Appl. Phys.*, vol. 90, no. 8, p. 4175, 2001.

[2] G. S. Doerk, C. Carraro, and R. Maboudian, “Temperature dependence of Raman spectra for individual silicon nanowires,” *Phys. Rev. B*, vol. 80, no. 7, p. 73306, Aug. 2009.

[3] R. Tsu and J. G. Hernandez, “Temperature dependence of silicon Raman lines,” *Appl. Phys. Lett.*, vol. 41, no. 11, p. 1016, 1982.

[4] T. Hart, R. Aggarwal, and B. Lax, “Temperature Dependence of Raman Scattering in Silicon,” *Phys. Rev. B*, vol. 1, no. 2, pp. 638–642, 1970.

[5] M. Balkanski, R. Wallis, and E. Haro, “Anharmonic effects in light scattering due to optical phonons in silicon,” *Phys. Rev. B*, vol. 28, no. 4, pp. 1928–1934, 1983.

[6] P. J. Van Zwol, D. F. Vles, W. P. Voorthuijzen, M. Péter, H. Vermeulen, W. J. Van Der Zande, J. M. Sturm, R. W. E. Van De Kruijs, and F. Bijkerk, “Emissivity of freestanding membranes with thin metal coatings,” *J. Appl. Phys.*, vol. 118, no. 21, 2015.

[7] Z. Huang, W. Zhou, and X. Tang, “Application of low-emissivity Pt layer on Ni alloy to high temperature,” *Acta Met. Sin.(Engl. Lett.)*, vol. 23, no. 1, pp. 1–7, 2010.

[8] A. Jacquot, G. Chen, H. Scherrer, A. Dauscher, and B. Lenoir, “Improvements of on-membrane method for thin film thermal conductivity and emissivity measurements,” *Sensors Actuators A Phys.*, vol. 117, no. 2, pp. 203–210, 2005.

[9] Y. Toivola, J. Thurn, R. F. Cook, G. Cibuzar, and K. Roberts, “Influence of deposition conditions on mechanical properties of low-pressure chemical vapor deposited low-stress silicon nitride films,” *J. Appl. Phys.*, vol. 94, no. 10, p. 6915, 2003.

[10] H. Ftouni, C. Blanc, D. Tainoff, A. D. Fefferman, M. Defoort, K. J. Lulla, J. Richard, E. Collin, and O. Bourgeois, “Thermal conductivity of silicon nitride membranes is not sensitive to stress,” *Phys. Rev. B*, vol. 92, no. 12, p. 125439, Sep. 2015.

[11] B. L. Zink and F. Hellman, “Specific heat and thermal conductivity of low-stress amorphous Si–N membranes,” *Solid State Commun.*, vol. 129, no. 3, pp. 199–204, 2004.

[12] A. Jain and K. E. Goodson, “Measurement of the Thermal Conductivity and Heat Capacity of Freestanding Shape Memory Thin Films Using the 3ω Method,” *J. Heat Transfer*, vol. 130, no. 10, p. 102402, 2008.

[13] R. Sultan, A. D. Avery, G. Stiehl, and B. L. Zink, “Thermal conductivity of micromachined low-stress silicon-nitride beams from 77 to 325 K,” *J. Appl. Phys.*, vol. 105, no. 4, p. 43501, 2009.

[14] X. Zhang and C. P. Grigoropoulos, “Thermal conductivity and diffusivity of free-standing silicon nitride thin films,” *Rev. Sci. Instrum.*, vol. 66, no. 2, p. 1115, 1995.

[15] P. J. Burkhardt and R. F. Marvel, “Thermal Expansion of Sputtered Silicon Nitride Films,” *J. Electrochem. Soc.*, vol. 116, no. 6, p. 864, 1969.

[16] A. K. Sinha, H. J. Levinstein, and T. E. Smith, “Thermal stresses and cracking resistance of dielectric films (SiN, Si3N4, and SiO2) on Si substrates,” *J. Appl. Phys.*, vol. 49, no. 4, p. 2423, 1978.

[17] F. C. Chiu, “A review on conduction mechanisms in dielectric films,” *Advances in Materials Science and Engineering*, vol. 2014. Hindawi Publishing Corporation, pp. 1–18, 2014.

[18] S. M. Sze, “Current Transport and Maximum Dielectric Strength of Silicon Nitride Films,” *J. Appl. Phys. Appl. Phys. Lett. J. Appl. Phys. J. Appl. Phys.*, vol. 38, no. 38, pp. 2951–2250, 1967.

[19] S. Habermehl, R. T. Apodaca, and R. J. Kaplar, “On dielectric breakdown in silicon-rich silicon nitride thin films,” *Appl. Phys. Lett.*, vol. 94, no. 1, p. 12905, 2009.

[20] S. Habermehl and C. Carmignani, “Correlation of charge transport to local atomic strain in Si-rich silicon nitride thin films,” *Appl. Phys. Lett.*, vol. 80, no. 2, pp. 261–263, 2002.

[21] V. Prodanovic, H. W. Chan, J. Smedley, A. Theulings, S. Tao, H. V. D. Graaf, and P. M. Sarro, “Optimization of silicon-rich silicon nitride films for electron multiplication in timed photon counters,” *Procedia Eng.*, vol. 120, pp. 1111–1114, 2015.

[22] M. C. Lemme, T. J. Echtermeyer, M. Baus, and H. Kurz, “A Graphene Field-Effect Device,” *IEEE Electron Device Lett.*, vol. 28, no. 4, pp. 282–284, Apr. 2007.

[23] J. H. Warner, N. P. Young, A. I. Kirkland, and G. A. D. Briggs, “Resolving strain in carbon nanotubes at the atomic level,” *Nat. Mater.*, vol. 10, no. 12, pp. 958–962, 2011.

[24] J. C. Meyer, A. K. Geim, M. I. Katsnelson, K. S. Novoselov, D. Obergfell, S. Roth, C. Girit, and A. Zettl, “On the roughness of single- and bi-layer graphene membranes,” *Solid State Commun.*, vol. 143, no. 1–2, pp. 101–109, 2007.

[25] D. Yoon, Y.-W. Son, and H. Cheong, “Negative Thermal Expansion Coefficient of Graphene Measured by Raman Spectroscopy,” 2011.

[26] A. D. Smith, F. Niklaus, A. Paussa, S. Vaziri, A. C. Fischer, M. Sterner, F. Forsberg, A. Delin, D. Esseni, P. Palestri, M. Östling, and M. C. Lemme, “Electromechanical piezoresistive sensing in suspended graphene membranes,” *Nano Lett.*, vol. 13, no. 7, pp. 3237–3242, 2013.

[27] S.-H. Bae, Y. Lee, B. K. Sharma, H.-J. Lee, J.-H. Kim, and J.-H. Ahn, “Graphene-based transparent strain sensor,” *Carbon N. Y.*, vol. 51, no. 1, pp. 236–242, Jan. 2013.

[28] Q. Cao, H. Kim, N. Pimparkar, J. P. Kulkarni, C. Wang, M. Shim, K. Roy, M. a Alam, and J. a Rogers, “Medium-scale carbon nanotube thin-film integrated circuits on flexible plastic substrates,” *Nature*, vol. 454, no. 7203, pp. 495–500, Jul. 2008.

[29] H. Marsh and R. Menendez, “Chapter 2 – Mechanisms of Formation of Isotropic and Anisotropic Carbons,” in *Introduction to Carbon Science*, 1989, pp. 37–73.

[30] A. Oberlin, “Carbonization and graphitization,” *Carbon N. Y.*, vol. 22, no. 6, pp. 521–541, 1984.

[31] K. S. S. Novoselov, A. K. K. Geim, S. V. V Morozov, D. Jiang, Y. Zhang, S. V. V Dubonos, I. V. V Grigorieva, and A. A. Firsov, “Electric field effect in atomically thin carbon films.,” *Science (80-.).*, vol. 306, no. 5696, pp. 666–669, Oct. 2004.

[32] J. Robertson, “Amorphous carbon,” *Adv. Phys.*, vol. 35, no. 4, pp. 317–374, 1986.

[33] N. F. (Nevill F. Mott and E. A. (Edward A. Davis, *Electronic processes in non-crystalline materials*. Clarendon Press, 1979.

[34] G. F. Schneider, V. E. Calado, H. Zandbergen, L. M. K. Vandersypen, and C. Dekker, “Wedging transfer of nanostructures,” *Nano Lett.*, vol. 10, no. 5, pp. 1912–1916, 2010.

[35] M. Munz, C. E. Giusca, R. L. Myers-Ward, D. K. Gaskill, and O. Kazakova, “Thickness-Dependent Hydrophobicity of Epitaxial Graphene,” *ACS Nano*, vol. 9, no. 8, pp. 8401–8411, Aug. 2015.

[36] F. Xia, V. Perebeinos, Y. Lin, Y. Wu, and P. Avouris, “The origins and limits of metal-graphene junction resistance.,” *Nat. Nanotechnol.*, vol. 6, no. 3, pp. 179–184, 2011.

[37] G. Giovannetti, P. A. Khomyakov, G. Brocks, V. M. Karpan, J. Van Den Brink, and P. J. Kelly, “Doping graphene with metal contacts,” *Phys. Rev. Lett.*, vol. 101, no. 2, pp. 4–7, 2008.

[38] M. Vanin, J. J. Mortensen, A. K. Kelkkanen, J. M. Garcia-Lastra, K. S. Thygesen, and K. W. Jacobsen, “Graphene on metals: A van der Waals density functional study,” *Phys. Rev. B*, vol. 81, no. 8, p. 81408, 2010.

[39] W. Yao, E. Wang, K. Deng, S. Yang, W. Wu, A. V. Fedorov, S. K. Mo, E. F. Schwier, M. Zheng, Y. Kojima, H. Iwasawa, K. Shimada, K. Jiang, P. Yu, J. Li, and S. Zhou, “Monolayer charge-neutral graphene on platinum with extremely weak electron-phonon coupling,” *Phys. Rev. B - Condens. Matter Mater. Phys.*, vol. 92, no. 11, pp. 2–6, 2015.

[40] V. V. Volkov, D. C. Crew, Y. Zhu, and L. H. Lewis, “Magnetic field calibration of a transmission electron microscope using a permanent magnet material,” *Rev. Sci. Instrum.*, vol. 73, no. 6, p. 2298, 2002.

[41] R. Misra, M. McCarthy, and A. F. Hebard, “Electric field gating with ionic liquids,” *Appl. Phys. Lett.*, vol. 90, no. 5, pp. 2006–2008, 2007.

[42] J. Xia, F. Chen, J. Li, and N. Tao, “Measurement of the quantum capacitance of graphene,” *Nat Nanotechnol*, vol. 4, no. 8, pp. 505–509, 2009.

[43] I. Heller, S. Chatoor, J. Männik, M. A. G. Zevenbergen, C. Dekker, and S. G. Lemay, “Influence of electrolyte composition on liquid-gated carbon nanotube and graphene transistors,” *J. Am. Chem. Soc.*, vol. 132, no. 48, pp. 17149–17156, 2010.

[44] Y. C. Lin, C. C. Lu, C. H. Yeh, C. Jin, K. Suenaga, and P. W. Chiu, “Graphene annealing: How clean can it be?,” *Nano Lett.*, vol. 12, no. 1, pp. 414–419, 2012.

Summary

In this thesis, we use *in-situ* Transmission Electron Microscopy (TEM) to characterize novel two-dimensional materials, such as graphene and black phosphorus. Unlike conventional TEM, the *in-situ* method allows us to apply external stimuli, i.e. electrical currents and heating, while imaging the material of interest.

Chapter 1 introduces graphene, the material which is mainly investigated in this thesis, and explains the benefits of using in-situ microscopy to study novel materials.

Chapter 2 explains how a TEM works, and how it can be used to extract meaningful information about two-dimensional materials. In particular, we show how to count the number of layers based on the analysis of the electron diffraction pattern (graphene and black phosphorus) and STEM imaging contrast (graphene only).

In Chapter 3, a brief review illustrates how TEM can be used to study defects in graphene. Special attention is given to the experimental observation of “self-healing” of damaged graphene lattice. We analyse and compare four recent experiments, taken from literature, which encountered the “self-healing” effect.

Chapter 4 shows the results of *in-situ* electrical and heating TEM experiments on graphene nanoribbons. Using the fine probe of the electron microscope, operated in Scanning TEM (STEM) mode, we sculpt suspended graphene nanoribbons, from 1.5 to 350 nm wide and ~200 nm long, with different number of layers. Heating the graphene at ~900 K during the sculpting ensures that the crystalline structure is preserved. Simultaneously, we perform 2-probe and 4-probe in-situ electrical measurements to correlate their electrical conductivity with their width. We find that wide nanoribbons (W > 50 nm) behave as ohmic conductors, whose conductivity scales linearly with the width. Instead, the narrower ribbons (W~2-50 nm) display a transport gap that ranges from ~10 to 700 meV. We also perform temperature dependent measurements on the same nanoribbons: from 4.2 K to 300 K, we find variable range hopping and thermal activated behavior; from 300 K to 873 K, thermal generation of charge carriers causes the electrical conductivity to increase. This last observation is compatible with the fact that the Fermi level of these suspended graphene structure is close to the charge neutrality point.

Chapter 5 reports the combination of *in-situ* electrical measurements with electron holography to study the electrostatic charge accumulation on graphene nanotips. Two graphene tips, 6 (60) nm wide and separated by 8 (58) nm gap, are fabricated using the method described in Chapter 4. A static potential of 4 (10) Volts is applied across them, and the resulting phase shift around the tips is recorded using electron holography. The electrostatic charge distribution is calculated from the phase map using Poisson’s equation: we find an accumulation of 16±1 (60±1) electron/holes on the extremities of

the tips. The spatial resolution of the charge distribution is limited to 1 nm by the fringe spacing of the hologram. Finite Element Method simulations can accurately describe the charge distribution of multilayer and monolayer graphene tips. The contribution of quantum capacitance is found to be negligible in the multilayer graphene sample (< 2% of the measured charge). It remains unclear whether it contributes to the monolayer, where it could reduce the local charge density up to 10%, compared to the non-quantum result.

Chapter 6 contains all the fabrication recipes and the experimental details which were not included in Chapters 4 and 5. Most importantly: the temperature calibration of the in-situ heating device; the variation of electrical conductivity of amorphous carbon during graphitization at high-temperature.

Samenvatting

In dit proefschrift gebruiken we *in-situ* Transmissie-elektronenmicroscopie (TEM) om nieuwe tweedimensionale materialen, zoals grafeen en zwarte fosfor, te karakteriseren. In tegenstelling tot traditionele TEM, staat de *in-situ* methode externe stimuli toe tijdens het afbeelden, zoals elektrische stroom en verhitting.

In hoofdstuk 1 wordt grafeen, het materiaal dat in dit proefschrift het meest wordt onderzocht, geïntroduceerd. De voordelen van het gebruik van in-situ microscopie om nieuwe materialen te bestuderen worden uitgelegd.

In hoofdstuk 2 wordt de werking van de TEM uitgelegd. Voorts wordt beschreven hoe waardevolle informatie over tweedimensionale materialen met de TEM verkregen kan worden. In het bijzonder laten we zien hoe we het aantal lagen kunnen tellen op basis van elektronendiffractie (grafeen en zwarte fosfor) en met het contrast van STEM beelden (alleen grafeen).

In Hoofdstuk 3 wordt een overzicht gegeven van hoe TEM gebruikt kan worden bij het bestuderen van defecten in grafeen. Speciale aandacht wordt besteed aan de experimentele waarneming van “zelf-reparatie” van beschadigde grafeen roosters. We analyseren en vergelijken vier recente experimenten, die we in de literatuur vonden, waarin het “zelf-reparatie” effect optrad.

In hoofdstuk 4 worden de resultaten getoond van de *in-situ* elektrische en verhittings TEM experimenten aan grafeen nanolinten. Door gebruik te maken van de hele kleine bundel van de elektronenmicroscoop in de raster TEM (STEM) modus, kunnen we los liggende nanolinten van grafeen boetseren met een breedte van 1.5 tot 350 nm en een lengte van ongeveer 200 nm, bestaande uit een verschillend aantal lagen. Verhitting van het grafeen tot ongeveer 900 K tijdens het boetseren zorgt ervoor dat de kristalstructuur behouden blijft. Gelijktijdig voeren we twee- en vier-punts in-situ elektrische metingen uit om de elektrische geleiding te correleren met de breedte. We vinden dat brede nanolinten ($W > 50$ nm) zich gedragen als Ohmse geleiders, waarvoor de de geleiding lineair schaalt met de breedte. Daarentegen vertonen de smallere linten ($W \sim 2$-50 nm) een transportgat variërend van ~10 tot 700 meV. We voeren tevens experimenten met een variabele temperatuur uit op dezelfde nanolinten: Tussen 4.2 K en 300 K vinden we *variable range hopping* en thermische geactiveerd gedrag; tussen 300 K en 873 K neemt de elektrische geleiding toe door de thermische generatie van ladingsdragers. Deze laatste observatie is in overeenstemming met het feit dat het Ferminiveau van deze los liggende grafeenstructuren dicht bij het punt van ladingsneutraliteit ligt.

In hoofdstuk 5 wordt verslag gedaan van de combinatie van *in-situ* elektrische metingen en elektronholografie om de elektrostatische ladingsophoping op grafeen-nanopunten te bestuderen. Twee grafeenpunten, 6 (60) nm breed en gescheiden door een 8 (58) nm gat, werden vervaardigd met de methode beschreven in hoofdstuk 4. Een statische potentiaal van 4 (10) Volt werd over hen gezet en de resulterende faseverschuiving rond de punten werd vastgelegd met behulp van elektronholografie. De elektrostatische ladingsverdeling werd berekend uit het fase-plaatje met behulp van de Poisson vergelijking: we vinden een ophoping van 16±1 (60±1) elektronen/gaten op de uiteinde van de punten. De resolutie in positie van de ladingsverdeling is beperkt tot 1 nm vanwege de lijn-afstanden van het hologram. Simulaties met de eindige-element-methode kunnen de ladingsverdeling van multi- en monolagen grafeenpunten nauwkeurig beschrijven. De bijdrage van de kwantumcapaciteit bleek verwaarloosbaar in het multilaag grafeenmonster (< 2% van de gemeten lading). Het blijft onduidelijk of het wel bijdraagt aan de monolaag, waar het de lokale ladingsdichtheid kan reduceren tot wel 10% vergeleken met het niet-kwantummechanische resultaat.

Hoofdstuk 6 bevat alle fabricagerecepten en experimentele details, die niet opgenomen zijn in de hoofdstukken 4 en 5. Met name: de temperatuur kalibratie van de in-situ verhittingschips; de variatie in elektrische geleiding van amorf koolstof tijdens de grafitisering bij een hoge temperatuur.

Curriculum Vitae

Leonardo VICARELLI

05-09-1986	Born in Siena, Italy

Education

2000 – 2005	High School Liceo Scientifico Statale “Galileo Galilei” Siena, Italy
2005 - 2009	Bachelor of Science in Physics Università di Pisa, Italy *Thesis:* “Present state of mid-sized and big RLG (Ring Laser Gyroscope) and first results from the G-Pisa RLG” *Promotor:* Dr. Angela Di Virgilio
2009 - 2012	Master of Science in Physics Università di Pisa, Italy *Thesis:* “Terahertz Photodetection in Graphene Field Effect Transistors” *Promotors:* Dr. Vittorio Pellegrini & Prof. Dr. Alessandro Tredicucci
2012 - 2017	Ph.D. in Applied Physics Delft University of Technology, the Netherlands *Thesis:* “In-situ Transmission Electron Microscopy Studies on Graphene” *Promotor:* Prof. Dr. H.W. Zandbergen

List of Publications

Relevant to this thesis

[1] A. Castellanos-Gomez, L. Vicarelli, E. Prada, J. O. Island, K. L. Narasimha-Acharya, S. I. Blanter, D. J. Groenendijk, M. Buscema, G. A. Steele, J. V. Alvarez, H. W. Zandbergen, J. J. Palacios, and H. S. J. Van Der Zant, “Isolation and characterization of few-layer black phosphorus,” 2D Mater., vol. 1, no. 2, p. 25001, 2014.

[2] L. Vicarelli, S. J. Heerema, C. Dekker, and H. W. Zandbergen, “Controlling Defects in Graphene for Optimizing the Electrical Properties of Graphene Nanodevices,” ACS Nano, vol. 9, no. 4, pp. 3428–3435, Apr. 2015.

[3] L. Vicarelli, S. J. Heerema, C. Dekker and H. W. Zandbergen, “In-situ electrical measurements of Graphene Nanoribbons fabricated through Scanning Transmission Electron Microscopy” (in preparation)

[4] L. Vicarelli, V. Migunov, S. K. Malladi, H. W. Zandbergen, and Rafal E. Dunin-Borkowski, “Graphene based World's smallest 4 atto-Farad capacitor” (to be submitted)

Other publications

[5] L. Vicarelli, M. S. Vitiello,D. Coquillat,A. Lombardo, A. C. Ferrari,W. Knap,M. Polini,V. Pellegrini and A. Tredicucci, “Graphene field-effect transistors as room-temperature terahertz detectors,” Nature Materials 11, pp. 865–871, Sept. 2012

[6] S. J. Heerema, G. F. Schneider, M. Rozemuller, L. Vicarelli, H. W. Zandbergen, and C. Dekker, “1/f noise in graphene nanopores,” Nanotechnology, vol. 26, no. 7, p. 74001, Feb. 2015.

[7] L. Vicarelli and H. W. Zandbergen “Novel TEM holder for in-situ gas, biasing and heating experiments” (in preparation)

[8] A. K. Erdamar, L. Vicarelli, M. Neklyudova, S. J. Heerema, G. Pandraud, C. Dekker and H. W. Zandbergen. “Back side lithography technique for transmission electron microscopy research” (to be submitted)